

ABSTRACT

Title of Dissertation: TRANSIENT SPECTROSCOPY AND
DYNAMICS OF OPTICALLY
CENTRIFUGED MOLECULES

Hannah M. Ogden, Doctor of Philosophy, 2020

Dissertation directed by: Professor Amy S. Mullin, Department of
Chemistry and Biochemistry

This dissertation investigates the behavior of molecules with extreme amounts of rotational energy and oriented angular momentum. The molecules studied in this thesis are prepared in an optical centrifuge and are studied using high-resolution transient IR absorption spectroscopy. The optical centrifuge uses intense, shaped laser pulses to accelerate molecules angularly into extreme rotational states. Through the interaction with the field, anisotropic molecules are trapped and follow the field through its angular acceleration. The final angular frequency of the molecules depends on the spectral profile of the centrifuge. The result is an ensemble of molecules with highly oriented angular momentum and rotational energies far from that of equilibrium. High-resolution transient IR absorption spectroscopy is used to measure nascent distributions of optically centrifuged molecules, as well as the collisional dynamics of the centrifuged molecules as they relax toward equilibrium by means of a collisional cascade.

These studies show that an optical centrifuge can launch N₂O molecules into rotational states with $J \geq 195$, and that the mechanism for collisional energy transfer depends on the rotational energy and angular momentum of the molecules. We show that our optical centrifuge is capable of driving CO₂ into rotational states up to $J = 280$, and we measure spectral perturbations that have not been observed previously. We measure the full rotational distribution of centrifuged CO and show that states up to $J = 80$ are populated using the full centrifuge bandwidth. This study of CO provides a lower limit to the final angular frequencies of N₂O and CO₂ prepared in our optical centrifuge. We have developed a tunable optical centrifuge to measure directly the nascent population distributions of centrifuged molecules, from which the capture and acceleration efficiencies for CO and CO₂ are compared. Lastly, the effect of reactant rotational energy on bimolecular reactions is investigated. We control the rotational energy in CO reactants and measure the yield of C₂ products. We find that CO rotational energy inhibits bimolecular reactions that form C₂. This work provides new information about the properties and behavior of molecules in a previously inaccessible energy regime and lays the groundwork for future investigations.

TRANSIENT SPECTROSCOPY AND DYNAMICS OF OPTICALLY
CENTRIFUGED MOLECULES

by

Hannah M. Ogden

Dissertation submitted to the Faculty of the Graduate School of the
University of Maryland, College Park, in partial fulfillment
of the requirements for the degree of
Doctor of Philosophy
2020

Advisory Committee:
Professor Amy S. Mullin, Chair
Professor John T. Fourkas
Professor Millard H. Alexander
Professor Daniel Falvey
Professor Steven L. Rolston

© Copyright by
Hannah M. Ogden
2020

Dedication

To my family

Acknowledgements

I would like to start by thanking my advisor, Dr. Amy Mullin. Her passion and dedication to this research and my success as a scientist has been invaluable. She has challenged and encouraged me throughout each step of my graduate career. The research we have done on the optical centrifuge has helped prepared me for any challenges ahead.

I would also like to thank Dr. John Fourkas. He has been very helpful in many different aspects of my research including optical centrifuge and 3-color projects. I would also like to thank my committee members Dr. Daniel Falvey, Dr. Millard Alexander, and Dr. Steve Rolston for taking the time to read and provide feedback on this thesis.

My relationships with past and current members of the Mullin group have been such an important aspect of my life. Dr. Matt Murray is a fantastic mentor. His positive spirit is unlike anyone I have ever met. He showed me the best path forward countless times. I would also like to thank Paul Diss who has been by my side since the very first semester of classes. His support during all the many challenges of graduate school has been unwavering. I would like to make a special thanks to Tara Michael. I could not ask for a better labmate. She was a key part of collecting all the data presented in this thesis and I could not have done it without her. Her thoroughness and dedication elevated everything we did to the next level. I would also like to thank Chris Lukowski for his help in the lab as well as during many practice talks. I would like to thank Fourkas group including Sandra Gutierrez, Nikos Liaros, and Amanda Souna. Each of them has helped me in a significant way.

Table of Contents

Dedication.....	ii
Acknowledgements.....	iii
List of Tables.....	vi
List of Figures.....	vii
List of Abbreviations.....	xiv
Chapter 1: Introduction.....	1
1.1 Background.....	1
1.2 Outline.....	4
Chapter 2: Experimental Instrumentation and Methods.....	7
2.1 The Optical Centrifuge Pulse.....	7
2.1.1 Theory of an Optical Centrifuge.....	7
2.1.2 Generating the Optical Centrifuge Pulses.....	12
2.1.3 Building a Tunable Optical Centrifuge.....	15
2.1.4 Making a Dynamic Polarization Grating (DPG).....	17
2.1.5 Measuring the Chirp Rate of the Optical Centrifuge Pulse.....	20
2.2 High-Resolution Transient IR Absorption Spectroscopy.....	23
2.2.1 Theory.....	23
2.2.2 Experimental Setup of the High-Resolution Transient IR Absorption Spectrometer.....	26
2.2.3 Transient IR Absorption Signals.....	30
2.2.4 Doppler-Broadened Line Profiles.....	31
2.2.5 State-Specific Number Densities.....	33
2.2.6 Polarization-Sensitive IR Absorption Measurements.....	34
Chapter 3: Spectroscopy and Dynamics of N ₂ O Super Rotors with $J \leq 205$ Initially Prepared in an Optical Centrifuge.....	38
3.1 Introduction.....	38
3.2 Experimental Details.....	41
3.3 Results and Discussion.....	44
3.3.1 Spectroscopy of N ₂ O High- J States.....	44
3.3.2 Polarization-Sensitive Transient IR Absorption Signals of N ₂ O.....	48
3.3.3 Polarization-Sensitive Translational Temperatures of N ₂ O.....	51
3.3.4 Orientational Anisotropy Measurements.....	54
3.4 Conclusion.....	56
Chapter 4: High-Resolution Transient IR Absorption Spectroscopy of CO ₂ $J = 186$ -280: Observation of Spectral Perturbations.....	57
4.1 Introduction.....	57
4.2 Experimental Details.....	60
4.3 Results and Discussion.....	64
4.3.1 IR Transition Frequencies for CO ₂ States with $J = 186$ -280.....	65
4.3.2 Identifying the Origin of the Perturbations.....	70
4.4 Conclusion.....	72
Chapter 5: Characterization and Collision Dynamics of Optically Centrifuged CO.....	74

5.1 Introduction.....	74
5.2 Experimental Details.....	76
5.3 Results and Discussion	79
5.3.1 CO Excited in an Optical Centrifuge with SI Bandwidth.....	79
5.3.2 CO Excited in an Optical Centrifuge with SII Bandwidth	83
5.3.3 Collision Dynamics of Optically Centrifuged CO.....	86
5.3.4 Estimating Rotational Excitation of Other Molecules in the Optical Centrifuge	90
5.4 Conclusion	90
Chapter 6: Nascent Distributions of CO and CO ₂ made with a Tunable Optical Centrifuge: Measuring Capture and Acceleration Efficiencies	92
6.1 Introduction.....	92
6.2 Experimental Details.....	95
6.2.1 Controlling the Angular Frequency of the Optical Centrifuge	96
6.2.2 High-Resolution Transient IR Spectroscopy of Centrifuged CO and CO ₂	97
6.3 Results and Discussion	99
6.3.1 Transient IR Probe Transitions of CO ($v=0, J = 41-49$) and CO ₂ ($00^0_0, J =$ $200-240$).....	100
6.3.2 Rotational Excitation Using the Full Bandwidth of the Optical Centrifuge	101
6.3.3 Nascent Distributions of CO and CO ₂ from a Tunable Optical Centrifuge	102
6.3.4 Intensity-Dependent Nascent Populations	111
6.4 Conclusion	113
Chapter 7: The Effect of CO Rotation from Shaped Pulse Polarization on Reactions that form C ₂	115
7.1 Introduction.....	115
7.2 Experimental Details.....	116
7.3 Results and Discussion	118
7.3.1 Dispersed Emission Measurements: C ₂ Formation.....	119
7.3.2 Multiphoton Absorption of CO.....	121
7.3.3 Mechanism of C ₂ Formation.....	123
7.3.4 Effect of Rotational Excitation on CO Reactivity	128
7.4 Conclusion	131
Chapter 8: Conclusions and Future Work.....	133
Appendix: Dunham Coefficients for CO	137
Bibliography	139

List of Tables

- Table 2.1 Possible configurations of dipole moment and angular momentum vectors for in- and out-of-plane molecules.
- Table 3.1 Observed and predicted R-branch N₂O (00⁰1←00⁰0) IR transition frequencies.
- Table 4.1 Observed (ν_{obs}) and calculated (ν_{calc}) IR transition frequencies in the R-branch of the antisymmetric stretch (00⁰1← 00⁰0) of CO₂ and their differences
- Table 6.1 Rotational energies and Ω_J values for selected J -states of CO and CO₂.
- Table 6.2 IR probe transition frequencies for CO and CO₂ used in this study.
- Table 7.1 Rate constants for formation of the CO($a^3\Pi$) state.
- Table A.1 Relationships between spectral constants and Dunham coefficients.
- Table A.2 Reported Dunham coefficients (in cm⁻¹) for the main isotope of CO based on absorption and plasma emission spectra. Data up to $J = 93$ was used in the global fit.

List of Figures

- Figure 2.1 An overview of the key components of the spectrometer. An amplified, chirped-pulse laser system generates the optical centrifuge pulse. A frequency-stabilized, high-resolution, CW IR probe is used to detect the centrifuged molecules using transient IR absorption spectroscopy.
- Figure 2.2 The electric field of the optical centrifuge induces a dipole moment in a molecule that interacts with the field, ultimately trapping the molecule.
- Figure 2.3 a) Spectral profile of positively- and negatively-chirped pulses. b) Spectral profile of Ω_{OC} .
- Figure 2.4 Stimulated Raman excitation of a rotational ladder
- Figure 2.5 A schematic of the optical components used to generate the optical centrifuge pulses. The key components of the IR spectrometer are shown as well.
- Figure 2.6 Pulse characteristics for optical components that generate the centrifuge pulse.
- Figure 2.7 Schematic diagram showing how the angular frequency of the optical trap is controlled by reducing the bandwidth of the positively-chirped pulse in the pulse shaper.
- Figure 2.8 a) Spectra of pulses that create the optical centrifuge. Bandwidth reduction of the positively-chirped pulse reduces the rotational excitation by the trap. b) Optical trap intensity as a function of angular frequency. A solid blue line indicates the intensity profile of the angular frequency when the full bandwidth is used, and a black dashed line indicates the intensity profile of the angular frequency when the bandwidth has been reduced.
- Figure 2.9 a) Experimental set up for the optical centrifuge and dynamic polarization grating polarizations. b) The optical centrifuge has linearly polarized light that angularly accelerates over the time of the pulse. c) The dynamic polarization grating polarization changes from 45° linear, to right circular, to -45° linear, to left circular and back to 45° linear.
- Figure 2.10 A schematic of the experimental set up used to collect the SFG signal as a function of delay time.

- Figure 2.11 a) An example of the sum-frequency-generation signal. b) The SFG signal as a function of time between the two chirped pulses. c) The optical frequency of the SFG signal as a function of time between the two chirped pulses.
- Figure 2.12 Example of $P(2)$ and $R(2)$ IR transitions of CO.
- Figure 2.13 A detailed schematic of the high-resolution transient IR absorption spectrometer.
- Figure 2.14 a) Optical centrifuge pulse and IR probe propagation and polarization configuration. b) Top-down view of the beam path of the multi-pass detection. c) Side-view of the multi-pass detection where the IR beam crosses the optical centrifuge beam 11 times.
- Figure 2.15 a) An example of AC- and DC-coupled signals collected simultaneously from InSb IR detectors. b) Corresponding fractional absorption signal.
- Figure 3.1 The Fortrat diagram for predicted N₂O IR transition frequencies for the antisymmetric stretch ($00^0_1 \leftarrow 00^0_0$) band.
- Figure 3.2 a) Spectra of the chirped pulses. b) Optical centrifuge intensity used to rotationally excite N₂O.
- Figure 3.3 a) The optical centrifuge aligns N₂O with the optical field. b) N₂O molecules trapped by the centrifuge rotate in the xy -plane. The IR probe beam propagates along the x -axis and intersects the optical centrifuge beam at 90°. c) Predicted IR transition frequencies for the R-branch absorption of the antisymmetric stretch of N₂O ($00^0_1 \leftarrow 00^0_0$).
- Figure 3.4 Line-center transient absorption measurements with IR probe polarization parallel (\vec{E}_{\parallel}) to the original plane of centrifugation and snapshots of frequency tuned absorption at $t = 50, 100,$ and 200 ns after optical centrifuge excitation for a) $J = 140$ and b) $J = 195$ states.
- Figure 3.5 Deviations (observed-predicted) for R -branch IR transition frequencies of N₂O for $J = 140-205$.
- Figure 3.6 a) Polarization-dependent line-center transient measurements for N₂O states with $J = 92, 160, 180, 195$. b) Transient signals resulting from molecules with a component of their angular momentum along the z -axis are denoted as $S_z(t)$ (red) and those

along x and y are denoted $S_x(t) = S_y(t)$ (blue).

- Figure 3.7 J -dependent fractional absorption intensities for N_2O at three times $t =$ a) 50, b) 150, and c) 250 ns after the optical centrifuge excitation. In-plane signals are shown with red circles and out-of-plane are shown with inverted blue triangles. Lines are a guide for the eye.
- Figure 3.8 Doppler-broadened line profiles for in- and out-of-plane molecules for states with $J = 92, 160, 180, 195$. The $J = 92$ state is shown at $t = 200$ ns after the centrifuge pulse and the $J = 160, 180,$ and 195 are shown at $t = 60$ ns after the centrifuge pulse.
- Figure 3.9 Translational temperatures for in- (red circles) and out-of-plane (inverted blue triangles) N_2O molecules in the $J = 92, 160, 180,$ and 195 states at a) $t = 50$ ns, and b) $t = 100$ ns.
- Figure. 3.10 Time-resolved orientational anisotropy of N_2O states with $J = 92, 160, 180,$ and 195 . Orientational isotropy is denoted with a dotted grey line at $1/3$.
- Figure 4.1 A Fortrat diagram of predicted rovibrational IR transition frequencies for the antisymmetric stretch ($00^01 \leftarrow 00^00$) absorption of CO_2 based on a 3rd-order polynomial expansion in $J(J + 1)$. Previously measured transition frequencies are shown in blue and predicted transition frequencies are shown in red.
- Figure 4.2 a) Spectra of the chirped pulses of the optical centrifuge. b) Optical centrifuge intensity as a function of angular frequency.
- Figure 4.3 Geometry of the optical centrifuge beam and IR probe propagation, IR polarization, and molecular rotation imparted to the CO_2 molecules by the optical centrifuge.
- Figure 4.4 a) Transient signals of the CO_2 R(196) transition collected as a function of IR frequencies. b) The signals at $t = 100$ ns are used to identify the line-center frequency. A Gaussian fit is used as a guide to identify line-center.
- Figure 4.5 a) Spectral fingerprinting of the CO_2 (00^01-00^00) R(212) transition relative to the (01^11-01^10) R(56) transition. b) Line-center transient absorption signals of the (00^00), $J = 212$ state and the (01^10) $J = 56$ state.
- Figure 4.6 Line-center transient absorption signals for a number of CO_2 states with $J = 188-234$ at a pressure of 5 Torr.

- Figure 4.7 Deviations (observed-predicted) in IR transition frequencies for 22 CO₂ states with $186 \leq J \leq 256$.
- Figure 4.8 a) A comparison of calculated (v_{calc}) and predicted transition frequencies (v_{pred}) for CO₂ R-branch transitions. b) A comparison of observed transition frequencies (v_{obs}) with those calculated using rotational energies reported in the CDSD4000.
- Figure 4.9 A Fortrat diagram of calculated IR transition frequencies based on rotational energies of the (00⁰0) and (00⁰1) states reported in the CDSD4000.
- Figure 4.10 Deviations for calculated and predicted rotational energies for the a) (00⁰0) states and b) (00⁰1) state.
- Figure 4.11 Energy-level crossings for the a) (00⁰1) and (03³0) states and b) (00⁰1) and (11¹0(1)) states.
- Figure 5.1 Chirped pulse spectra for a) Spectrum I and b) Spectrum II. Optical damage to a reflector led to a drop in intensity near $\lambda = 788$ nm of SI. Optical centrifuge intensities for c) SI and d) SII as a function of trap angular frequencies.
- Figure 5.2 Predicted IR transition frequencies for CO for rotational states up to $J = 100$ based on Dunham coefficients of the rotational energies of the ground and first excited vibrational states.
- Figure 5.3 In- ($S_z(t)$) and out-of-plane ($S_x(t)$ and $S_y(t)$) transient IR absorption signals for CO states with $J = 29-66$ prepared using the optical centrifuge with SI.
- Figure 5.4 Orientational anisotropy $r(t)$ based on line-center transient absorption signals. $S/N < 1$ are not included. A dashed grey line shows the $r(\infty) \approx 0.33$ for an isotropic distribution.
- Figure 5.5 a) The distribution for in- (red) and out-of-plane (blue) CO signals at 5 Torr. b) Spectral intensity of SI vs the angular frequency of the optical field.
- Figure 5.6 Transient absorption signals using IR probe polarization parallel (red) and perpendicular (blue) to the plane of centrifuge rotation. Shown are CO states with $J = 62, 73,$ and 80 at a CO pressure of 2.5 Torr. These signals were measured for optically centrifuged CO prepared with the SII bandwidth.

- Figure 5.7 a) The distribution for measurements for in- and out-of-plane signals at a pressure of 2.5 Torr. b) Spectral intensity of SII vs angular frequency of the optical field.
- Figure 5.8 Transient Doppler-broadened line profiles for CO rotational states with $J = 62, 70, 72,$ and 75 with a CO pressure of 5 Torr collected at $t = 100$ ns after the optical centrifuge pulse. Residuals for the Gaussian fit are shown below each profile. The IR probe polarization was parallel with the plane of centrifuge rotation.
- Figure 5.9 The average translational temperature over the first 10 collisions are shown. Individual measurements are shown in black circles, and the average translational temperature for each J state is shown with a red triangle. The dotted line indicates 300 K.
- Figure 5.10 Time-evolution of translational temperatures for CO rotational states with $J = 62, 70, 72,$ and 75 at a pressure of 5 Torr and IR probe polarization parallel to the plane of centrifuge rotation. The number of collisions are included in each plot based on the average time between collisions is 20 ns at 300 K.
- Figure 6.1 a) Spectra of optical centrifuge pulses. Bandwidth reduction of the positively-chirped pulse ω_1 reduces the rotational excitation in the trap. b) Optical trap intensity as a function of angular acceleration. c) Angular frequency of the optical trap at full-width half-maximum (FWHM) as a function of clipping the positively-chirped pulse. Clip 0 corresponds to the full bandwidth trap; Clips 1-3 have sequentially smaller ultimate angular frequencies.
- Figure 6.2 Schematic energy levels and R-branch transitions for transient IR probing of optically centrifuged CO and CO₂. The optical centrifuge excites molecules to a set of centrifuged rotational states with J_{OC} . The transient IR probe measures state-specific number densities for the nascent distribution of centrifuged molecules.
- Figure 6.3 a) The full bandwidth optical trap intensity as a function of angular frequency. b) The population distribution of CO with $J = 29 - 68$ made using the full bandwidth trap and a pressure of 2.5 Torr. c) Number densities of CO ($J = 41 - 49$) and CO₂ ($J = 200 - 240$) made with the full bandwidth centrifuge at 500 mTorr.

- Figure 6.4 a) Full bandwidth spectrum (left-most), and three reduced bandwidth decreasing from left to right. Measurement of number densities for b) CO ($J = 62$), c) CO ($J = 49$), d) CO₂ ($J = 240$) at the four bandwidths.
- Figure 6.5 a-c) Nascent distributions of CO and CO₂ rotational states as a function of reducing the optical centrifuge spectral bandwidth. The lines are included as guides to identify the molecule. d-f) The populations measured with Clips 1-3 relative to populations made with the full bandwidth (Clip 0) centrifuge shown in Figure 6.3c.
- Figure 6.6 a) Total number densities of trapped molecules for CO and CO₂ from integrated nascent distribution measurements. b) The ratio of [CO₂] to [CO] shows that CO₂ has a capture and acceleration probability in the optical centrifuge that is nearly three times larger than that for CO.
- Figure 6.7 a) Instantaneous laser power of sequentially clipped pulses as a function of optical centrifuge angular frequency. Nascent J -specific populations at 100 ns of b) CO₂ and c) CO that are released from the optical trap as a function of instantaneous laser power.
- Figure 7.1 Spectral output from the pulse shaper.
- Figure 7.2 Power-dependent Swan-band emission spectra observed with a CO pressure of 100 Torr and optical centrifuge polarization.
- Figure 7.3 Relative integrated emission intensities at CO pressures of a) 100 Torr, b) 75 Torr, c) 50 Torr, and d) 25 Torr with either the optical centrifuge polarization (OCP) or dynamic polarization grating (DPG) configurations.
- Figure 7.4 Comparison of relative integrated C₂ emission intensities for optical centrifuge polarization (OCP) and the dynamic polarization grating (DPG) as a function of cell pressure with $I = 1.8 \times 10^{13} \text{ W cm}^{-2}$ (41 mJ/pulse).
- Figure 7.5 Power-dependent analysis to determine the lower limit for the number of photons absorbed by CO prior to formation of C₂(d³Π_g). Logarithmic plots of integrated spectral intensity vs pulse energy for (a) the optical centrifuge polarization (OCP) and (b) the dynamic polarization grating (DPG).
- Figure 7.6 Electronic energy levels and terms for CO and C₂. The red arrows indicate multiphoton absorption of seven and eight 800 nm

photons. Emission pathways are indicated with blue arrows and collision-induced intersystem crossing (denoted in green) leads to excitation of CO triplet states.

Figure 7.7 Time-dependent fractional populations of CO $B^1\Sigma^+(B)$, $A^1\Pi(A)$, $X^1\Sigma^+(X)$, $b^3\Sigma^+(b)$ and $a^3\Pi(a)$ for the four pressures used in our experiments. Formation of the $a^3\Pi$ state is enhanced at higher pressures shows the fractional populations for the CO states at 100 Torr pressure. The relaxation of the b state occurs readily at pressures of 25-100 Torr and is predominantly collision induced.

Figure 7.8 a) The pressure dependence of the Swan band emission threshold. b) R -branch high-resolution transient IR absorption for the CO $J = 70$ state with OCP and DPG excitation. c) J -dependent transient intensities at 100 ns based on polarization-sensitive IR detection. d) Ratio of $S(J,t)$ values with OCP and DPG.

List of Abbreviations

BBO	Barium borate
CDSD4000	Carbon Dioxide Spectral Database at 4000 K
CW	Continuous wave
DPG	Dynamic polarization grating
FSR	Free spectral Range
FWHM	Full-width half-maximum
InSb	Indium antimonide
IR	Infrared
MPA	Multi-pass amplifier
OC	Optical centrifuge
OCP	Optical centrifuge polarization
QCL	Quantum cascade laser
SI	Spectrum-I
SII	Spectrum-II
SFG	Sum-frequency-generation
SDG	Synchronization and delay generator

Chapter 1: Introduction

1.1 Background

According to the Born-Oppenheimer approximation, the electronic, vibrational, and rotational motion of a molecule can be treated separately from one another. For gas-phase molecules at 300 K, the energy gaps between vibrational states are significantly larger than those between rotational states. In addition, at 300 K the time scales for vibrational motion are on the order of femtoseconds, whereas rotational motion occurs on the order of picoseconds. However, in the case of a molecule with large amounts of rotational energy, the relative energy gaps and time scales for vibrational and rotational motions become more similar. Based on the rigid-rotor and harmonic-oscillator models, the energy gaps between rotational states increase with increasing rotational quantum number, whereas the vibrational energy gaps decrease with increasing vibrational quantum number because of anharmonicity.

Molecules in high energy rotational states are observed in plasmas and as products of photodissociation and collisional energy transfer, yet much remains to be understood about their behavior and properties. Such high energy states cannot be accessed using traditional optical approaches, because selection rules for absorption and Raman processes limit changes in the rotational angular momentum to small ΔJ values. Advances in optical control of molecular rotation have led to new methods for controlling alignment, orientation, energy and directionality of molecular rotors.¹⁻⁶ These techniques include using two orthogonally polarized pulses of light with a time

delay, and a train of pulses with varying pulse lengths. These techniques can control a component of molecular motion, but are limited to relatively low- J states.

In 1999 Karczmarek et al. proposed an optical centrifuge, a laser-based technique that would excite molecules into extreme rotational states with oriented angular momentum.⁷ In their proposal, a non-resonant strong optical field would trap and rotationally excite anisotropic molecules in a controlled manner. The technique was termed an “optical centrifuge” because it would distinguish between molecules based on their moments of inertia. In the laboratory, the optical centrifuge is generated by overlapping a pair of optical pulses with opposite linear chirp and counter-rotating circular polarizations. The overlap of the pair of pulses generates a linear electric field that angularly accelerates over the time of the pulse. Molecules are trapped in the field through an interaction between an induced-dipole moment in the molecule and the electric field of the centrifuge pulse. The trapped molecules follow the linearly polarized field through its angular acceleration, resulting in an ensemble of rotationally excited molecules with highly oriented angular momentum. In 2000, Villeneuve and coworkers first illustrated the optical centrifuge technique by rotationally exciting Cl_2 to angular frequencies capable of breaking the molecular bond and detecting the Cl fragments using mass spectrometry.⁸

A number of theoretical studies on the optical centrifuge have been performed.^{7, 9-11} They include criteria for efficient trapping, and a purely classical and quantum description of the optical centrifuge excitation. These studies are described in more detail in Chapter 6.

The Mullin group has built a high-power optical centrifuge coupled to a high-resolution transient IR absorption spectrometer. We have used the optical centrifuge to observe previously unseen IR transitions of high- J state molecules and to study the collision dynamics of molecules with oriented angular momentum.¹²⁻¹⁸ Studies using this technique have revealed several key aspects of the behavior of molecules prepared in an optical centrifuge. Studies of optically centrifuged CO₂ and CO have shown how the centrifuged ensemble relaxes via a collisional cascade, and that large amounts of translational energy are gained through from impulsive collisions and non-resonant energy transfer.^{15, 16} The development of multi-pass IR detection in the spectrometer led to improved signal-to-noise levels and enabled new capabilities to measure the time-dependent orientational anisotropy of optically centrifuged molecules, and to investigate how atomic buffer gases collisions affect the relaxation dynamics of centrifuged molecules.^{17,18} Studies involving argon and helium illustrate the importance of rotational adiabaticity in collisions of super rotors in which the relative time scale of the collision and the molecular rotational period influence the energy transfer dynamics. We showed that collisions of He-CO₂ ($J = 100$) relax the rotational energy of optically centrifuged CO₂ faster than Ar-CO₂ ($J = 100$) collisions. The time-dependent orientational anisotropies with buffer gases was also investigated. Polarization-sensitive measurements showed that the more massive collision partner argon was more effective at reorienting the centrifuged CO₂. In other work, the Milner group has used coherent Raman spectroscopy to observe excitation and subsequent rotational revivals of N₂O molecules in an optical centrifuge.¹⁹

An optical centrifuge prepares an inverted rotational distribution of high- J states that are set apart from the background of thermally populated rotational states. The extent to which the distributions are separated in energy depends on the spectral bandwidth of the shaped pulses and the molecules moments of inertia. Under low pressure conditions, the excited distribution is amenable to detailed spectroscopic investigation without the spectral congestion and line broadening that accompany traditional heating methods such as plasmas or flames.²⁰ These aspects make coupling of an optical centrifuge to a high-resolution transient IR absorption spectrometer a very powerful approach for investigating the high energy regime of optically centrifuged molecules.

1.2 Outline

The outline of the thesis is as follows:

- Chapter 2: A description of the optical centrifuge coupled to a high-resolution transient IR absorption spectrometer is given. Key aspects of the optical centrifuge pulses and IR detection are described.
- Chapter 3: This chapter presents a study of optically centrifuged N₂O focused on identifying new IR transition frequencies for N₂O rotational states up to $J = 205$ and investigating the collision dynamics of these states. The collision dynamics of N₂O with $J = 92, 160, 180,$ and 195 are studied with polarization-sensitive high-resolution transient IR absorption spectroscopy.

Experimental findings show that low-energy models are adequate at describing N₂O molecules in states up to $J = 205$.

- Chapter 4: This chapter focuses on identifying IR transition frequencies for high- J states of optically centrifuged CO₂. Transition frequencies for $J = 186$ - 280 are measured and evidence of two spectral perturbations are observed. The observed spectral perturbations are compared to predicted spectral perturbations based on published effective Hamiltonian calculations.
- Chapter 5: This chapter describes a study performed to identify the full distribution of optically centrifuged CO. The rotational distribution is characterized as a function of pressure and spectral bandwidth. The study shows that the optical centrifuge is capable of driving CO molecules to rotational states as high as $J = 80$ with angular frequencies of $\Omega_J \approx 5.6 \times 10^{13} \text{ rad s}^{-1}$. An investigation of the translational temperatures of the high- J states show that the high- J states of CO predominantly undergo resonant rotation-to-rotation energy transfer.
- Chapter 6: The chapter describes experiments that use a tunable optical centrifuge to measure the capture and acceleration efficiency of CO and CO₂ in the optical trap. A tunable optical centrifuge controls the rotational frequencies of the molecules released from the optical trap. Transient IR measurements of the nascent CO and CO₂ distributions quantify the capture and acceleration efficiency. It is found that the optical centrifuge is three times more efficient at trapping and accelerating CO₂ than CO.

- Chapter 7: This chapter studies the effect that rotational energy has on bimolecular reactions of CO that ultimately form C₂. Power- and pressure-dependent measurements of C₂ Swan band emission characterize reaction yields. Polarization-sensitive, high-resolution, transient IR absorption measurements of CO are used to characterize the extent of rotation energy imparted to the CO reactants. The reaction yield drops as CO rotation is increased.
- Chapter 8: This chapter presents conclusions of the experiments performed and suggests new ideas for future work.

Chapter 2: Experimental Instrumentation and Methods

This chapter describes the experimental instrumentation and methods used to prepare and study rotationally excited molecules. An amplified, chirped-pulse laser system generates the optical centrifuge pulses that are used to excite molecules rotationally in a low-pressure gas cell. A frequency-stabilized, high-resolution continuous-wave (CW), IR probe laser is propagated through the cell orthogonally to the optical centrifuge beam. Transient IR absorption is used to study the rotationally excited molecules. The overall experimental approach is shown in Figure 2.1.

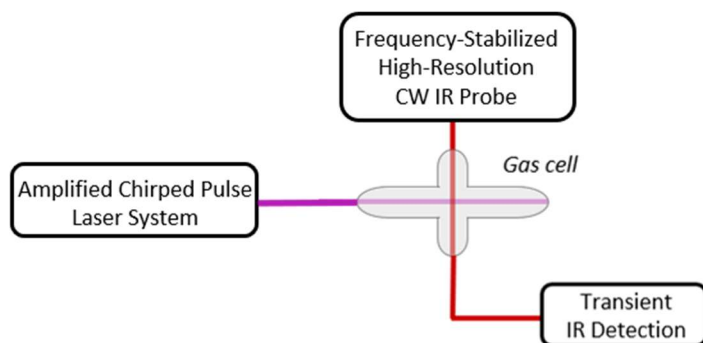


Figure 2.1 An overview of the key components of the spectrometer. An amplified, chirped-pulse laser system generates the optical centrifuge pulse. A frequency-stabilized, high-resolution, CW IR probe is used to detect the centrifuged molecules using transient IR absorption spectroscopy.

2.1 The Optical Centrifuge Pulse

2.1.1 Theory of an Optical Centrifuge

In the research reported here, a laser-based technique known as an optical centrifuge is used to impart extreme amounts of rotational energy to gas-phase molecules. The fundamental operating principles of the optical centrifuge trap are

described in this section, along with classical and quantum mechanical descriptions of the rotational excitation. The classical description is based on an angularly accelerating optical trap. The quantum mechanical description is based on adiabatic excitation of a rotational ladder by sequential Raman transitions.^{7,18}

The optical centrifuge traps molecules with an intense optical field and spins them into extreme rotational states. The optical field induces a dipole moment along the most polarizable axis of a molecule, and the induced dipole $\vec{\mu}_{ind}$ interacts with the electric field of the optical pulse to trap the molecule. For a molecule to be trapped, it must have an anisotropic polarizability. The interaction potential U_0 between the molecule and the optical field is

$$U_0 = -\frac{1}{4}\Delta\alpha|E|^2\cos^2\theta \quad (2.1)$$

where $\Delta\alpha$ is the molecular polarizability, $|E|^2$ is the amplitude of the electric field, and θ is the angle between the most polarizable axis of the molecule and the polarization of the optical field, as shown in Figure 2.2.

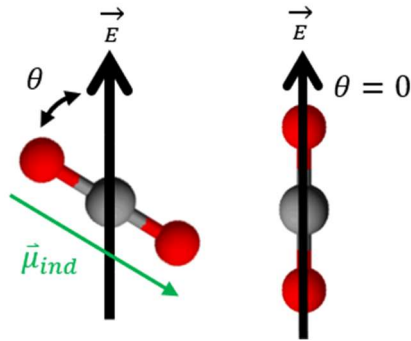


Figure 2.2 The electric field of the optical centrifuge induces a dipole moment in a molecule that interacts with the field, ultimately trapping the molecule.

The optical centrifuge has linear polarization that accelerates angularly over the time of the pulse. A molecule that is trapped in the field follows the field through

the angular acceleration. In this way, the angular momentum of the trapped molecules can be increased to large values that are dependent on the spectral bandwidth of the laser pulse. The angularly accelerating field is formed by combining, in time and space, a pair of pulses with counter-rotating circular polarization and opposite linear chirp. A positively-chirped pulse $\omega_1(t)$ has frequency that increases linearly in time and a negatively-chirped pulse $\omega_2(t)$ has frequency that decreases linearly in time. The time-dependent frequency of positively- and negatively-chirped pulses is given by Equations 2.2 and 2.3, respectively, where ω_0 is the initial frequency and β is the chirp rate.

$$\omega_1(t) = \omega_0 + \beta t \quad (2.2)$$

and

$$\omega_2(t) = \omega_0 - \beta t. \quad (2.3)$$

The angular frequency of the optical field Ω_{OC} is defined by the instantaneous frequency difference of the pair of chirped pulses:

$$\Omega_{OC} = \frac{1}{2}\Delta\omega = \frac{1}{2}(\omega_1(t) - \omega_2(t)). \quad (2.4)$$

Figure 2.3a shows the spectral profile for the pair of oppositely-chirped pulses. Figure 2.3b shows the spectral profile as a function of Ω_{OC} .

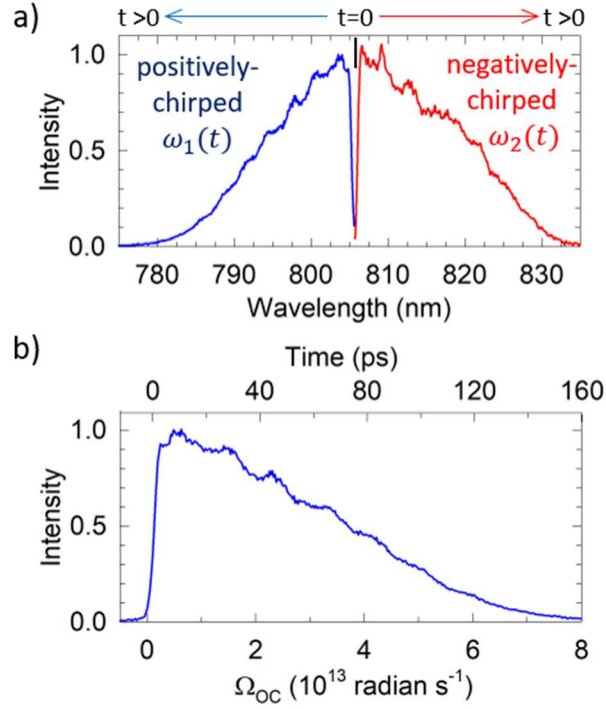


Figure 2.3 a) Spectral profiles of positively- and negatively-chirped pulses. b) Spectral profile of Ω_{OC} .

A molecule trapped and rotationally excited by the optical centrifuge will rotate with the same frequency as the polarization of the optical field. Therefore, the angular frequency of the molecule Ω_J , where J is the rotational quantum number, is equal to the angular frequency of the optical centrifuge Ω_{OC} . The rotational energy of the centrifuged molecules is determined by the angular frequency of the molecule Ω_J and the molecule's moment of inertia I :

$$E_{rot} = \frac{1}{2} I \Omega_J^2. \quad (2.5)$$

The quantum mechanical description of rotational energy is

$$E_{rot} = BJ(J + 1) + \text{higher order terms}, \quad (2.6)$$

where $B = \hbar^2/2I$ is the rotational constant and \hbar is Planck's constant. By equating the classical and quantum rotational energies, one can estimate the rotational quantum number of centrifuged molecules as

$$J \approx \sqrt{J(J+1)} = \left(\frac{I}{2B}\right)^{\frac{1}{2}} \Omega_J = \left(\frac{I}{8B}\right)^{\frac{1}{2}} \Delta\omega. \quad (2.7)$$

In this way, the spectral bandwidth of the pair of pulses leads to rotational energy in the centrifuged molecules. The spectral bandwidth of the pair of pulses used in each study will be shown in each chapter as this is key in determining the amount of rotational energy imparted to the molecules.

Molecules with $J = 0$ are most effectively trapped, based on Equation 2.1. Trapping is possible for molecules with $\theta \neq 0$ if the field polarization sweeps through π radians as it turns on.⁷ This condition provides a lower limit for the trap turn-on time, defined by

$$\frac{\beta t_{on}^2}{2} > \pi. \quad (2.8)$$

An upper limit exists for the turn-on time that is defined by the kinetic energy gain of a molecule in the optical trap. The turn-on time of the trap must be such that the molecules kinetic energy K does not exceed the trap potential energy U_0 . In the limit of a rotationally cold molecule, the kinetic energy gained by a molecule as the trap turns on is

$$K \sim \frac{U_0}{2} + \frac{1}{2}I(\beta t_{on})^2. \quad (2.9)$$

The first term $U_0/2$ is from the virial theorem and the second term describes the rotational energy gain in the trapped molecules during the turn-on time.⁷

The optical centrifuge has also been discussed using a quantum mechanical description based on adiabatic excitation with sequential stimulated Raman transitions.¹⁸ Successive coupling between rotational states of the ground electronic level with virtual states by the laser field results in adiabatic excitation via sequential Raman excitation. Figure 2.4 shows a schematic of this process

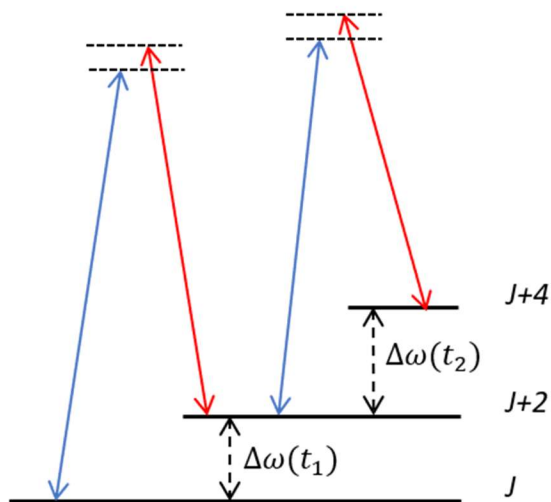


Figure 2.4 Stimulated Raman excitation of a rotational ladder.

2.1.2 Generating the Optical Centrifuge Pulses

The optical centrifuge pulses are generated by overlapping pairs of pulses with opposite linear chirps and counter-rotating circular polarizations in time and space. Figure 2.5 is a schematic diagram of the ultrafast components that generate the optical centrifuge pulses and the key components of the IR absorption spectrometer. The optical centrifuge laser system includes an ultrafast Ti:Sapphire oscillator, a regenerative amplifier, a custom-built chirped pulse shaper, and a multi-pass amplifier.

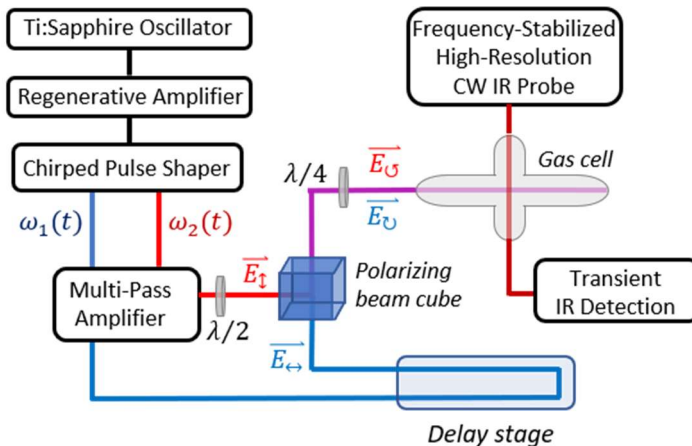


Figure 2.5 A schematic of the optical components used to generate the optical centrifuge pulse. The key components of the IR spectrometer are shown as well.

An ultrafast Ti:Sapphire oscillator generates 40 fs pulses at a repetition rate of 80 MHz. The pulses are centered at $\lambda = 805$ nm and have a full-width at half-maximum (FWHM) of 90 nm. The pulses are directed into a regenerative amplifier where they are stretched in time to 100 ps and amplified at a repetition rate of 10 Hz. Pulse stretching is achieved by dispersing the pulses with a grating that allows the blue wavelengths to travel longer distances than the red wavelengths. This process induces positive linear chirp in the pulses. The positively-chirped pulses have a FWHM of 35 nm.

The output of the regenerative amplifier is directed into a custom-built chirped pulse shaper designed to generate the pair of oppositely chirped pulses needed for the optical centrifuge. Each positively-chirped input pulse is spatially dispersed off a grating and split into a pair of pulses. The positive chirp is maintained for one of the pair of pulses, whereas the chirp is reversed for the other pulse using a pair of gratings. The output of the pulse shaper is a pair of pulses with $\lambda_0 = 805$ nm and

with opposite linear chirp. Figure 2.6 summarizes the pulse characteristics for the optical components discussed so far.

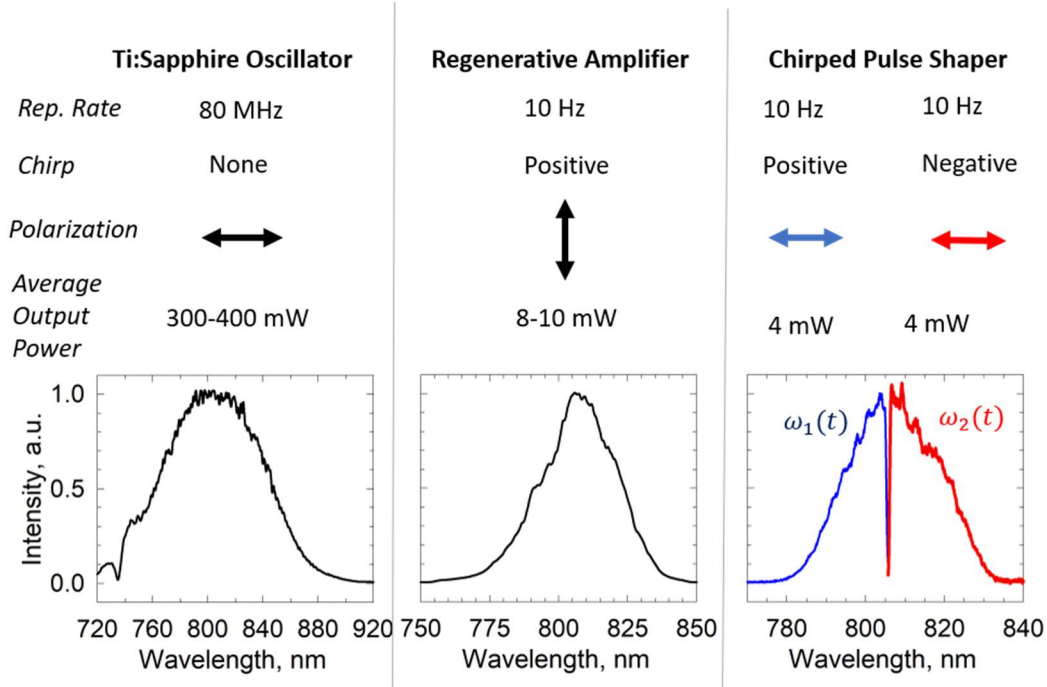


Figure 2.6 Pulse characteristics for optical components that generate the centrifuge pulse.

The pairs of oppositely-chirped pulses are directed into a multi-pass amplifier (MPA) for further amplification. The MPA is comprised of two independent paths $\omega_1(t)$ and $\omega_2(t)$ where each of the pair of pulses passes through a Ti:Sapphire rod four times. Each of the Ti:Sapphire rods is pumped at a repetition rate of 10 Hz with 300 mJ/pulse of 532 nm light from a frequency-doubled Nd:YAG laser. After completion of four passes through the Ti:Sapphire rods, the pair of pulses is amplified by nearly two orders of magnitude to 30 mJ/pulse. For optimal amplification, the 532 nm pulses are set to arrive at the Ti:Sapphire rods 20 ns before the first pass of the pair of chirped pulses. The timing of the 532 nm pump and the pair of pulses is

controlled with a synchronization and delay generator (SDG) that controls 3 Pockels cells in the regenerative amplifier and the Q-switch in the Nd:YAG laser.

The polarization of the amplified pair of pulses is modified to generate the optical centrifuge. The negatively-chirped pulse passes through a half wave-plate ($\lambda/2$) to rotate its polarization by 90° . The pair of chirped pulses is then recombined spatially in a polarizing beam cube and temporally with a delay stage that adjusts the beam path of the positively-chirped pulse. The pair of chirped pulses is then given opposite circular polarization by passing both beams through a quarter wave-plate ($\lambda/4$). The pulses are focused into the center of the gas cell to a beam waist of $w_0 = 53 \mu\text{m}$ using a 50 cm focal length lens.

2.1.3 Building a Tunable Optical Centrifuge

In Chapter 6, a tunable optical centrifuge is used to control the extent of rotational energy in optically centrifuged molecules. Tunability in an optical centrifuge is achieved by reducing the optical bandwidth $\Delta\omega$.^{8,19}

Figure 2.7 illustrates schematically how the tunability is accomplished. In the pulse shaper, the chirped pulses are spatially dispersed off a grating, and an adjustable beam block is used to decrease the bandwidth of the positively-chirped pulse. The angular acceleration of the optical trap depends on the combination of the pair of pulses. By removing the high-frequency components from the positively-chirped pulse, the extent of angular acceleration of the trap is reduced. To avoid optical damage to the Ti:Sapphire crystals in the multi-pass amplifier when the bandwidth is reduced, the pump power is decreased. The reduction in the pump power is

proportional to the intensity of the spectral bandwidth that is removed with the adjustable beam block.

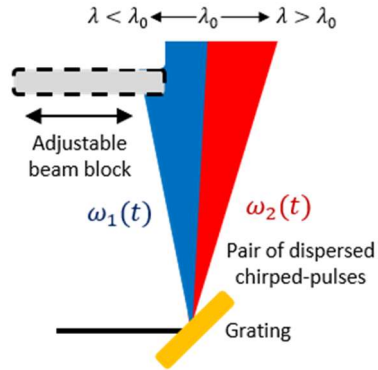


Figure 2.7 Schematic diagram showing how the angular frequency of the optical trap is controlled by reducing the bandwidth of the positively-chirped pulse in the pulse shaper.

Figure 2.8a compares the full-bandwidth spectrum to a reduced-bandwidth spectrum. The resulting angular acceleration of both traps is shown in Figure 2.8b. The ultimate angular frequency of the trap was tuned in these studies from $(4 - 6) \times 10^{13} \text{ rad s}^{-1}$.

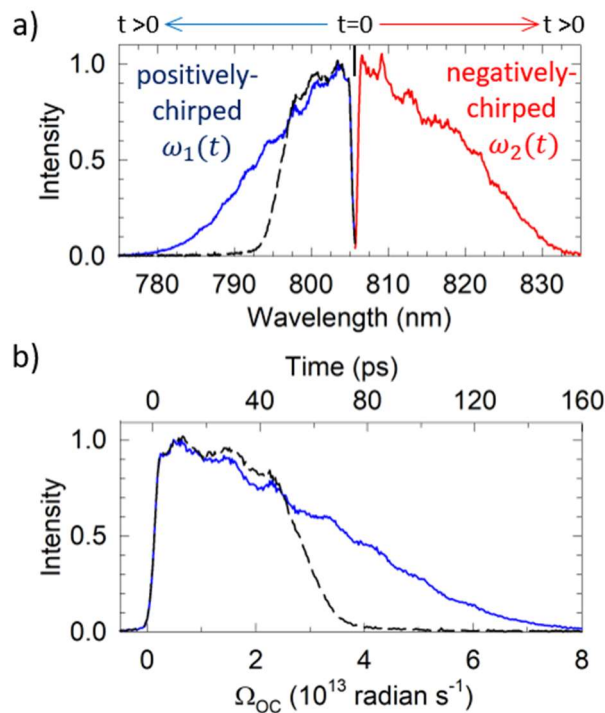


Figure 2.8 a) Spectra of pulses that create the optical centrifuge. Bandwidth reduction of the positively-chirped pulse reduces the rotational excitation by the trap. b) Optical trap intensity as a function of angular frequency. A solid blue line indicates the intensity profile of the angular frequency when the full bandwidth is used, and a black dashed line indicates the intensity profile of the angular frequency when the bandwidth has been reduced.

2.1.4 Making a Dynamic Polarization Grating (DPG)

In Chapter 7, the role of rotational energy in bimolecular reactions is investigated. In this study, the amount of rotational energy imparted to the reactant molecules is controlled by changing the shaped pulse polarization to either an optical centrifuge or a dynamic polarization grating (DPG). In the laboratory, the difference between the optical centrifuge and the DPG is based on the polarization of the pair of pulses. The optical centrifuge is made from pulses with counter-rotating circular polarization and the DPG is made from pulses with orthogonal linear polarization. The DPG is realized by removing the quarter wave-plate following the beam cube in Figure 2.5. A comparison of the OC and DPG experimental setups is shown in Figure

2.9a. In both cases, the pair of shaped pulses have opposite linear chirps. The time-dependent polarizations of the optical centrifuge and dynamic polarization grating are described in detail below.

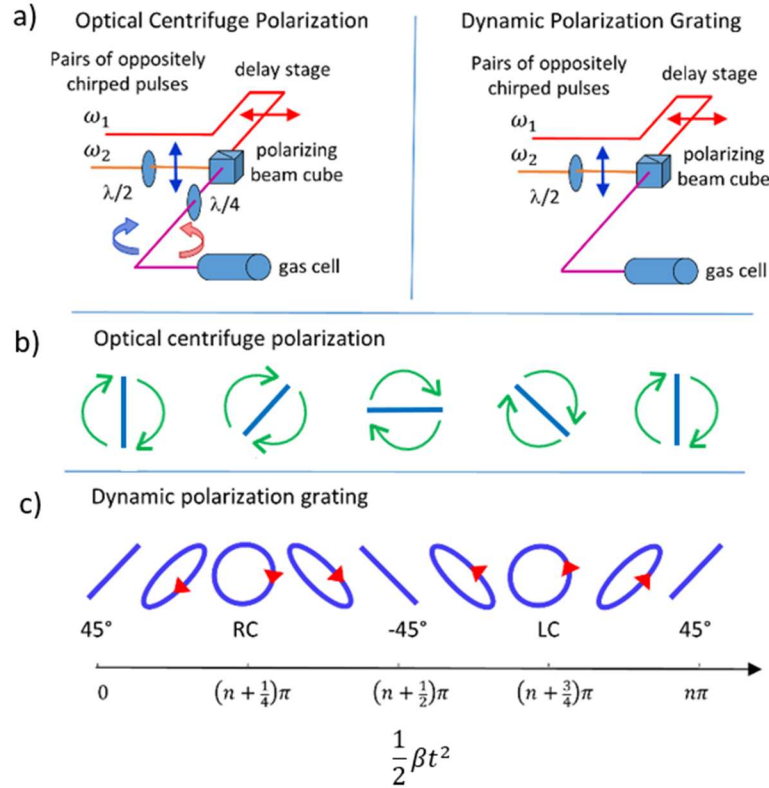


Figure 2.9 a) Experimental set up for the optical centrifuge and dynamic polarization grating polarizations. b) The optical centrifuge has linearly polarized light that angularly accelerates over the time of the pulse. c) The dynamic polarization grating polarization changes from 45° linear, to right circular, to -45° linear, to left circular and back to 45° linear.

The oscillation of an optical field propagating in the z -direction that starts at frequency ω_0 is

$$\cos(\omega_0 t + \varphi(t) - kz) \quad (2.10)$$

where $\varphi(t)$ is a phase shift. The instantaneous frequency is given by

$$\omega(t) = \frac{d}{dt}(\omega_0 t + \varphi(t)) \quad (2.11)$$

For a pulse with a linear chirp β (such as those used in this experiment), the time-dependent phase shift is $\varphi(t) = \frac{1}{2}\beta t^2$.

In the optical centrifuge, the linearly chirped pulses have opposite circular polarizations. Given no initial phase shift, the net optical field oscillation is

$$\left(\mathbf{x} \cos\left(\frac{1}{2}\beta t^2\right) + \mathbf{y} \sin\left(\frac{1}{2}\beta t^2\right)\right) \cos(\omega_0 t - kz). \quad (2.12)$$

The result is an instantaneously linearly polarized field that oscillates at an average frequency ω_0 and a polarization that spins at angular frequency $\beta t/2$, i.e. at an ever-increasing rate during the pulse. The accelerating angular frequency of the polarization is the key to exciting molecules rotationally. Figure 2.9b shows that the electric field rotates a complete cycle for π radians of $\frac{1}{2}\beta t^2$.

For the DPG, a pair of pulses with opposite linear chirp and orthogonal linear polarization are combined spatially and temporally. The resulting field oscillation is

$$\frac{\mathbf{x}+\mathbf{y}}{2} \cos(\omega_0 t - kz) \cos\left(\frac{1}{2}\beta t^2\right) - \frac{\mathbf{x}-\mathbf{y}}{2} \sin(\omega_0 t - kz) \sin\left(\frac{1}{2}\beta t^2\right). \quad (2.13)$$

Equation 2.13 is a combination of two linear fields at 45° and -45° . For any time that $\frac{1}{2}\beta t^2 = n\pi$, the sine of this argument is zero and the overall field is 45° and when $\frac{1}{2}\beta t^2 = \left(n + \frac{1}{2}\right)\pi$, the polarization is -45° . The field is left circularly polarized if $\frac{1}{2}\beta t^2 = \left(n + \frac{1}{4}\right)\pi$, and right circularly polarized if $\frac{1}{2}\beta t^2 = \left(n + \frac{3}{4}\right)\pi$. In the time between the situations where the field is linear and circularly polarized, the field has elliptical polarization. Figure 2.9c shows that the DPG field goes through a complete cycle over π radians of $\frac{1}{2}\beta t^2$. The base oscillation is at ω_0 and the polarization cycling frequency is $\beta t/2$.

The significant difference between the optical centrifuge and the dynamic polarization grating is how the field rotationally excites the trapped molecules. For

the optical centrifuge, the angularly accelerating field traps and spins the molecules into extreme rotational states. In the case of the dynamic polarization grating, the molecules do not have oriented angular momentum. Any rotational excitation in the DPG occurs through Raman transitions.

2.1.5 Measuring the Chirp Rate of the Optical Centrifuge Pulse

This section describes how the chirp rate β of the optical centrifuge is measured using a spectrally-resolved, time-dependent cross-correlation method. For this measurement, the wavelength of the cross-correlated output is collected as a function of delay time between the pair of oppositely chirped pulses. The output is a sum-frequency-generation (SFG) signal with a wavelength that is related to the chirp rate and the delay time, as discussed below.

Figure 2.10 is a schematic of the instrumentation used to collect the SFG signal as a function of Δt . The positively-chirped pulse is directed through a delay stage. The pair of pulses is overlapped spatially using a beam cube and focused onto a barium borate (BBO) crystal to generate the SFG signal. The signal is collected with a fiber optic cable fed into an Ocean Optics Spectrometer for Δt values of -15 ps to +15 ps. The SFG signal is fit to a Gaussian function to determine the center wavelength.

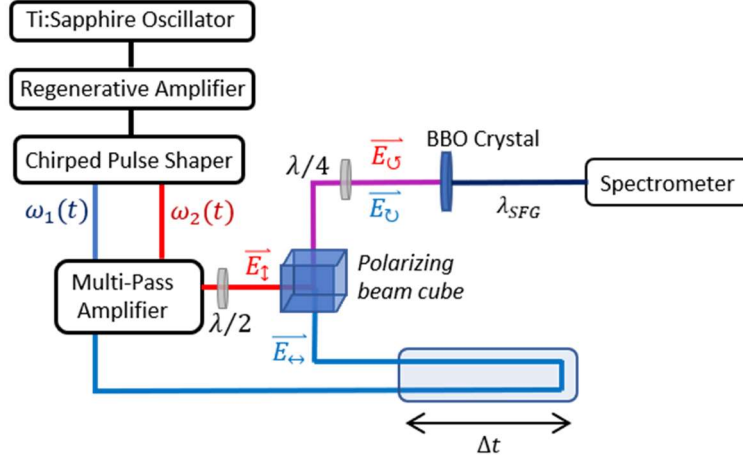


Figure 2.10 A schematic of the experimental set up used to collect the SFG signal as a function of delay time.

The linear chirp is defined as $\omega(t) = \beta t$. In this measurement, a time delay Δt is introduced in the positively-chirped pulse $\omega_1(t)$. With the time delay, the pulse has an instantaneous frequency of

$$\omega_1(t) = \omega_0 + \beta(t - \Delta t), \quad (2.14)$$

where ω_0 is the frequency at the start of the pulse. The negatively-chirped pulse has an instantaneous frequency of

$$\omega_2(t) = \omega_0 - \beta t. \quad (2.15)$$

When $\Delta t = 0$, the sum of the two frequencies is

$$\omega(t) = \omega_1(t) + \omega_2(t) = 2\omega_0. \quad (2.16)$$

The wavelength of the SFG signal when $\Delta t = 0$ is

$$\lambda_0 = \frac{2\pi c}{\omega(t)} = \frac{2\pi c}{2\omega_0}. \quad (2.17)$$

Introducing a time delay such that $\Delta t \neq 0$, the sum of the two pulses frequencies is

$$\omega(t) = \omega_1(t) + \omega_2(t) = 2\omega_0 - \beta\Delta t. \quad (2.18)$$

Equation 2.18 shows that the SFG signal depends linearly on Δt over the entire time of the pulse. For a fixed value of Δt , the SFG signal consists of a single wavelength, given by Equation 2.19.

$$\lambda(\Delta t) = \frac{2\pi c}{\omega(t)} = \frac{2\pi}{(2\omega_0 - \beta\Delta t)} \quad (2.19)$$

A positive Δt value will correspond to a red-shifted SFG signal and a negative Δt value will correspond to a blue-shifted SFG signal. Equation 2.19 is rearranged to determine the chirp rate β

$$\frac{2\pi c}{\lambda(\Delta t)} = 2\omega_0 - \beta\Delta t. \quad (2.20)$$

A plot of $2\pi c/\lambda(\Delta t)$ vs Δt gives a y-intercept of $2\omega_0$ and a linear slope of $m = -\beta$.

We have measured the SFG signal as a function of Δt to determine the chirp rate of the optical centrifuge pulses. An example of the measured signal is shown in Figure 2.11a. The center wavelength of the SFG signals as a function of Δt is shown in Figure 2.11b. The chirp rate β was determined from the slope of Figure 2.11c. The measured chirp rate from this experiment has the value $\beta = 0.5 \times 10^{12}$ rad s⁻¹ per ps.

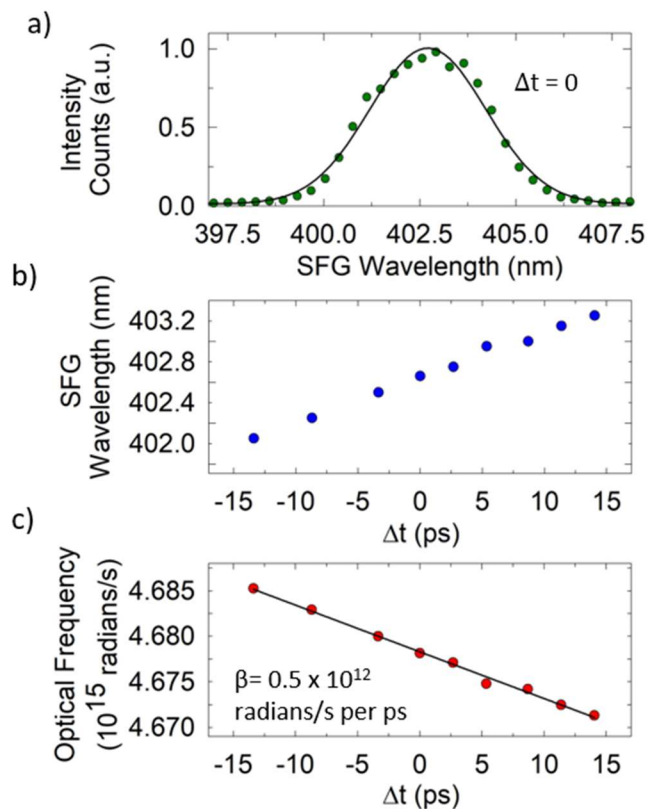


Figure 2.11 a) An example of the sum-frequency-generation signal. b) The SFG signal as a function of time between the two chirped pulses. c) The optical frequency of the SFG signal as a function of time between the two chirped pulses.

2.2 High-Resolution Transient IR Absorption Spectroscopy

2.2.1 Theory

The research reported in this thesis uses high-resolution, transient infrared (IR) absorption spectroscopy to investigate molecules prepared in extreme rotational states with an optical centrifuge. In this technique, a continuous-wave (CW) IR probe laser is used to measure the time-dependence of the population in individual rotational states for CO, CO₂ and N₂O. The IR probe light can be tuned to individual

rovibrational transition frequencies, and measure Doppler-broadened line profiles to yield information about J -dependent translational temperatures.

Transient absorption signals of individual rotational states are measured after the sample has been launched into a non-equilibrium state by the optical centrifuge. IR absorption measurements are made for rotational states that appear through a collisional cascade as the centrifuged molecules relax toward equilibrium and for states that have been directly prepared by the optical centrifuge.

A rovibrational transition occurs when the energy of the IR probe light is resonant with the energy difference between two rovibrational states, as shown in Figure 2.12 for CO. The selection rules for absorption of IR light are $\Delta J = \pm 1$. A $P(2)$ transition corresponds to CO ($v=0, J=2$) + IR \rightarrow CO ($v=1, J=1$). An $R(2)$ transition corresponds to CO ($v=0, J=2$) + IR \rightarrow CO ($v=1, J=3$).

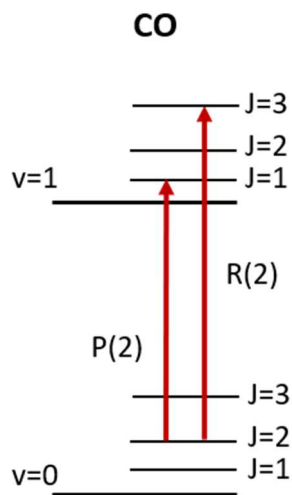


Figure 2.12 Example of $P(2)$ and $R(2)$ IR transitions of CO.

In the gas phase, Beer's Law for absorption is written as

$$I_t = I_0 e^{-\alpha p \ell}, \quad (2.21)$$

where I_t is the intensity of the transmitted light, I_0 is the intensity of incident light, α is the absorption coefficient, p is the pressure, and ℓ is the pathlength. The absorption coefficient α is defined in the gas phase by

$$a = Sf(0)N, \quad (2.22)$$

where S is the absorption strength, $f(0)$ is a line-shape factor and N is the number density of the gas at a reference temperature and pressure. The absorption strength S is an integrated absorption strength for a rotationally-resolved IR transition and is defined by

$$S = \int_0^\infty \sigma(\nu) d\nu, \quad (2.23)$$

where $\sigma(\nu)$ is the cross section for absorption, and ν is the frequency of the light. The line-shape factor $f(0)$ is defined by

$$f(0) = \frac{2}{\Delta\nu_{Doppler}} \sqrt{\frac{\ln 2}{\pi}}, \quad (2.24)$$

where $\Delta\nu_{Doppler}$ is the full-width at half-maximum (FWHM) for a Doppler-broadened absorption line. The FWHM of the Doppler-broadened absorption line is defined by

$$\Delta\nu_{Doppler} = \sqrt{\frac{8k_B T \ln 2}{mc^2}} \nu_0, \quad (2.25)$$

where T is the translational temperature, m is the mass, c is the speed of light, ν_0 is the line-center transition frequency, and k_B is Boltzmann's constant.

2.2.2 Experimental Setup of the High-Resolution Transient IR Absorption Spectrometer

The high-resolution transient IR absorption spectrometer used in this research is described in detail here. The key components of the spectrometer are an IR probe laser, IR detectors, a scanning Fabry-Perot etalon, active feedback control, and a multi-pass IR sample cell. This section also includes a detailed description of the IR beam path for probing the centrifuged molecules.

A quantum cascade laser (QCL) from Daylight Solutions is the high-resolution IR probe source used in this research. The QCL is a single-frequency laser operating between $\lambda = 4.2 - 4.5 \mu\text{m}$. The QCL has a spectral resolution of $\Delta\nu_{IR} < 2 \times 10^{-4} \text{ cm}^{-1}$ and linearly polarized. Doppler-broadened line profiles of CO_2 at 300 K have a FWHM linewidth of $\Delta\nu_{Dopp} = 4 \times 10^{-3} \text{ cm}^{-1}$. The extremely high-resolution of the QCL makes possible transient measurements of Doppler-broadened line profiles of centrifuged molecules. Translational temperatures of individual rotational states are determined from Doppler profiles.

A detailed schematic of the IR spectrometer is shown in Figure 2.13. The QCL is directed through 3 components: a multi-pass sample cell containing a low pressure gas sample, a 3-m reference cell containing a reference gas, and a Fabry-Perot etalon. Before entering the multi-pass sample cell, the linearly polarized light from the QCL passes through a tunable half wave-plate ($\lambda/2$) giving the IR light either parallel (\vec{E}_{\parallel}) or perpendicular (\vec{E}_{\perp}) polarization with respect to the plane of molecular rotation. Through each component, the transmitted IR light is collected on an indium antimonide (InSb) detector, shown as D in Figure 2.13. The detector used

for the sample has a response time of ~ 50 ns. Transient signals are collected and averaged on a digital oscilloscope and average for ~ 300 laser shots. The detectors used with the reference cell and etalon have rise times of 300 ns.

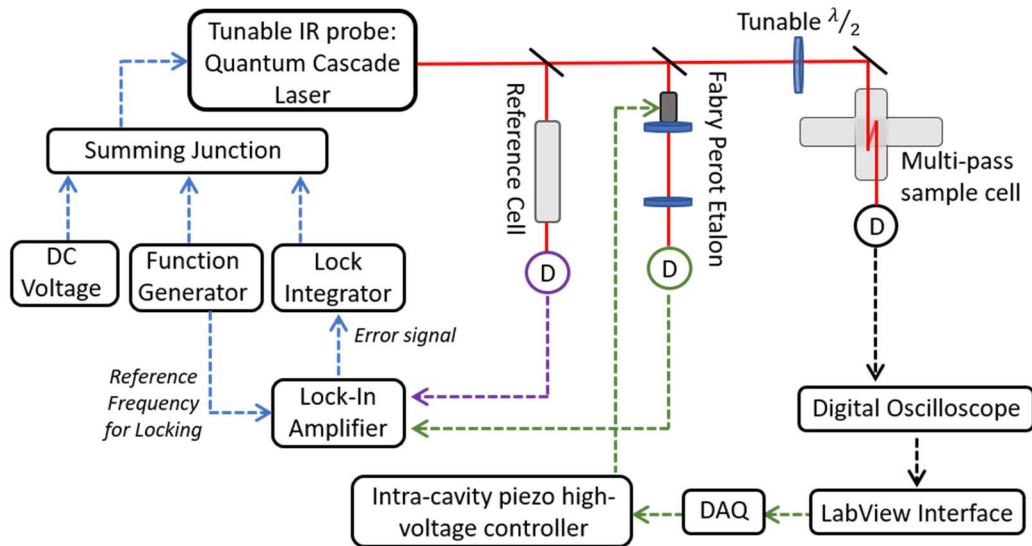


Figure 2.13 A detailed schematic of the high-resolution transient IR absorption spectrometer.

The output of the QCL is wavelength-stabilized using active feedback control. The IR laser frequency is modulated at 100 Hz with a function generator. The modulation frequency is the reference frequency for a lock-in amplifier that maintains the laser output at a fixed optical frequency either of a molecular transition or a fringe of the Fabry-Perot etalon.

A Fabry-Perot etalon is an optical cavity comprised of two parallel flat mirrors separated by a distance L . The etalon is tuned by applying a voltage to a piezoelectric transducer to which one of the cavity mirrors is attached. Constructive interference occurs when the light has an integer number of half-cycles in the length L . This

interference produces peaks (or fringes) that are evenly-spaced in frequency. The frequency spacing is the free spectral range (FSR), which is given by

$$FSR = \frac{c}{2L} \quad (2.26)$$

where c is the speed of light.

To measure Doppler-broadened line profiles, the frequency of the IR light is tuned in frequency steps of $5 \times 10^{-4} \text{ cm}^{-1}$. The frequency of the IR light is stabilized by locking to a fringe from the interference pattern. A voltage is applied to the piezoelectric element, resulting in a small change in the cavity length. The lock-in amplifier applies a voltage to the QCL to change the frequency of the light such that an integer number of cycles fit within the adjusted cavity length. Transient signals are collected at each IR frequency step.

Sample Cell IR Beam Pathlength

The centrifuged molecules are prepared and detected in a custom-built multi-pass sample cell. Figure 2.14a shows the geometry of the interaction region. The optical centrifuge beam propagates along the z -axis and molecules prepared by the optical centrifuge rotate in the xy -plane. In the multi-pass cell, the IR beam crosses the optical centrifuge beam 11 times. The spacing between the IR passes is 1.2 mm along the optical centrifuge axis, as shown in Figure 2.14b. The IR beam is focused to a beam waist $w_0 = 230 \text{ }\mu\text{m}$ using a lens with a 50 cm focal length. Figure 2.14c illustrates the overlap of the multi-pass IR beam with the optical centrifuge beam.

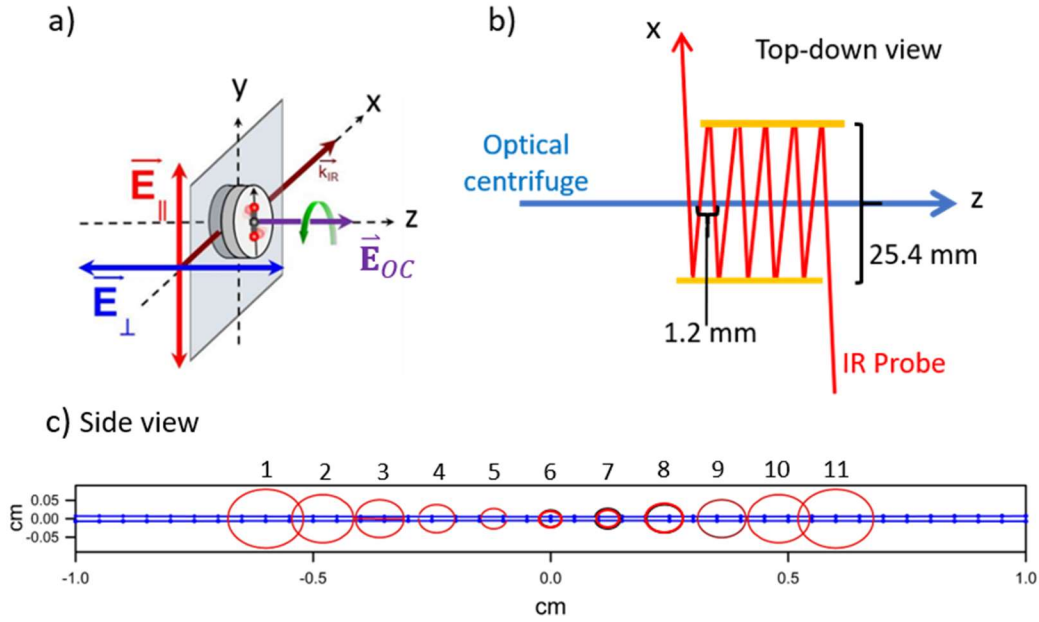


Figure 2.14 a) Optical centrifuge pulse and IR probe propagation and polarization configuration. b) Top-down view of the beam path of the multi-pass detection. c) Side-view of the multi-pass detection where the IR beam crosses the optical centrifuge beam 11 times.

Knowledge overlap pathlength of the optical centrifuge and IR probe is necessary to measure absolute number densities of centrifuged molecules. The beam waist w_0 of the optical centrifuge beam at the focal point is determined by

$$2w_0 = \frac{4\lambda}{\pi} \left(\frac{F}{D} \right), \quad (2.27)$$

where F is the focal length of the lens and D is the diameter of the input beam. The beam waist of the optical centrifuge at each IR beam crossing w_z has been calculated using the following expression:

$$w(z) = w_0 \sqrt{1 + \left(\frac{z}{z_R} \right)^2}, \quad (2.28)$$

where w_0 is the beam waist at the focal point, z is the distance from the focal point, and $z_R = \pi w_0^2 / \lambda$ is the Rayleigh length. The IR absorption pathlength is the sum of

the optical centrifuge beam diameter at each crossing and has a value of $\ell = 0.12 \text{ cm}$. At the optical centrifuge focal point, $w_o = 53 \text{ }\mu\text{m}$ and the sequential adjacent overlap points have $w_z = 54, 55, 56, 58, \text{ and } 61 \text{ }\mu\text{m}$.

2.2.3 Transient IR Absorption Signals

Transient IR absorption signals for individual rotational states of centrifuged molecules are collected on a digital oscilloscope interfaced to a LabVIEW program. Each transient signal is collected simultaneously on an AC-coupled channel and a DC-coupled channel. The oscilloscope is triggered by the optical centrifuge pulse using a photodiode located just before the sample cell. The trigger defines $t = 0$ for the transient absorption signals. The AC- and DC-coupled channels are used to determine the fractional change in absorption $\Delta I/I_0$ for the transient signal. Figure 2.15a shows AC- and DC-coupled channel transient signals for a negatively biased detector. The corresponding fractional absorption is related to the collected signals using Equation 2.29. Algebraic manipulation of these signals yields

$$\left| \frac{\Delta I}{I_0} \right| = \frac{\langle AC \rangle}{\langle DC \rangle - \langle AC \rangle}. \quad (2.29)$$

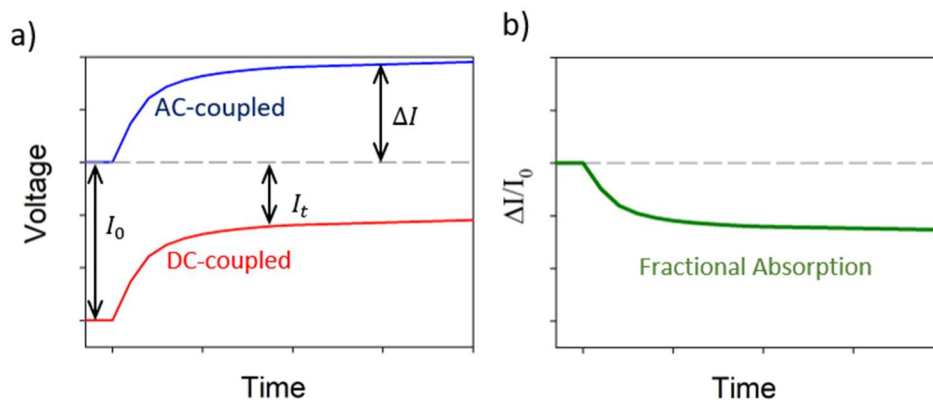


Figure 2.15 a) An example of AC- and DC-coupled signals collected simultaneously from InSb IR detectors. b) Corresponding fractional absorption signal.

2.2.4 Doppler-Broadened Line Profiles

Gas-phase molecules have line profiles that are Doppler shifted by the distribution of molecular speeds as

$$\nu = \nu_0 \left(1 \pm \frac{\text{vel}}{c} \right), \quad (2.30)$$

where ν_0 is the line-center frequency, vel is velocity, and c is the speed of light. Molecules moving toward the IR light absorb at higher frequencies while molecules moving away from the IR light absorb at lower frequencies. We measure state-specific Doppler-broadened line profiles to determine the translational temperature T of the centrifuged molecules. The line profile is measured by collecting transient signals at discrete IR frequencies across the profile. The data are fit to a Gaussian function to determine the translational temperature.

The Boltzmann distribution in its most general form is

$$P(E) dE = Ae^{-E/k_B T} dE, \quad (2.31)$$

where A is a proportionality constant, E is the energy, k_B is Boltzmann's constant, and T is the temperature.

For an isotropic distribution of velocities, the Boltzmann distribution of molecular speeds is given by

$$P_v(\text{vel})d\text{vel} = \sqrt{\frac{m}{2\pi k_B T}} e^{\left(\frac{-m\text{vel}^2}{2k_B T}\right)} d\text{vel}. \quad (2.32)$$

Using Equation 2.30, the Boltzmann distribution is written as a function of frequency as

$$P_v(v)dv = \sqrt{\frac{mc^2}{2\pi k_B T v_0^2}} e^{\frac{-mc^2(v-v_0)^2}{2k_B T v_0^2}} dv. \quad (2.33)$$

Equation 2.33 has the general form of a Gaussian function:

$$f(x) = ae^{\left(\frac{-x^2}{2b^2}\right)}, \quad (2.34)$$

where the FWHM is $2\sqrt{2 \ln 2} b$. The parameter b in the fitting function that depends on the FWHM of the Doppler-broadened profile such that

$$b = \sqrt{\frac{k_B T}{m} \frac{v_0}{c}}. \quad (2.35)$$

The FWHM of the Doppler-broadened profile Δv_{Dopp} is

$$\Delta v_{Dopp} = \sqrt{\frac{8 \ln 2 k_B T}{mc^2}} v_0. \quad (2.36)$$

Rearranging Equation 2.36 to solve for T gives

$$T = \frac{mc^2}{8 \ln 2 k_B} \left(\frac{\Delta v}{v_0}\right)^2. \quad (2.37)$$

Collecting the constants yields an expression for Doppler broadening given by

$$\frac{\Delta v_{Dopp}}{v_0} = 7.2 \times 10^{-7} \sqrt{\frac{T(K)}{m \text{ (amu)}}}. \quad (2.38)$$

2.2.5 State-Specific Number Densities

This section describes how fractional IR absorption measurements ($\Delta I/I_0$) are converted to state-specific number densities n_{Jv} . A description for the conversion of fractional absorption to number density is provided, followed by a description of how to determine state-specific number densities. Fractional absorption measurements are related to a number density through Beers Law:

$$1 - \frac{\Delta I}{I_0} = \frac{I_t}{I_0} = e^{-\alpha \ell}. \quad (2.39)$$

The overlap pathlength of the optical centrifuge with the IR probe is $\ell = 0.12$ cm as described in Section 2.2.2. The natural log of Beers Law gives

$$-\ln\left(\frac{I_t}{I_0}\right) = \alpha p \ell. \quad (2.40)$$

The total number density of the absorbing species (n/V) is related to Beers Law using the ideal gas law:

$$\frac{n}{V} = \frac{p}{RT} = \frac{-\ln\left(\frac{I_t}{I_0}\right)}{\alpha \ell} = \frac{-\ln\left(\frac{I_t}{I_0}\right)}{Sf(0)N\ell} \quad (2.41)$$

The state-specific number density is given by

$$\frac{n_{Jv}}{V} = \frac{-\ln\left(\frac{I_t}{I_0}\right)}{Sf(0)l} f_J f_v \quad (2.42)$$

where f_v and f_J are the fractional populations in the lower vibrational and rotational states, respectively, at a reference temperature. For the high- J rotational states probed in these experiments, S values have not been reported. To determine state-specific number densities for the high- J states, S was estimated for the high- J states by removing the Boltzmann component of the line strength values and accounting for the transition frequency dependence.

Transient measurements involve molecules that are not at equilibrium. The line shape factor must be scaled to the FWHM of the observed Doppler profile as shown in Equation 2.43.

$$\frac{n_{Jv}}{V} = \frac{-\ln\left(\frac{I_t}{I_0}\right)}{Sf(0)\ell} f_{Jf} f_v \frac{\Delta v_{obs}}{\Delta v_{Dopp}}. \quad (2.43)$$

The resulting number densities correspond to a transient population with no assumption about the rotational temperature.

2.2.6 Polarization-Sensitive IR Absorption Measurements

This section describes how polarization-sensitive IR probing is used to measure the orientational anisotropy r of the centrifuged molecules. The optical centrifuge prepares a highly anisotropic ensemble of molecules that rotate in the xy -plane with their angular momentum vectors along the z -axis. Determination of Doppler-broadened line profiles and populations originate from a series of transient measurements. Here we present how orientational anisotropy of transient absorption signals is determined.

Figure 2.14a shows the IR polarization configurations and the plane of molecular rotation prepared by the optical centrifuge. Deconvolution of polarization-sensitive measurements is used to extract the subsets of in- and out-of-plane angular momentum components. In-plane transient signals $S_z(t)$ result from molecules with a component of their angular momentum vectors along the z -axis, and out-of-plane transient signals $S_x(t)$ and $S_y(t)$ result those with a component of their angular momentum vector along the x - and/or y -axis.

Polarization-sensitive transient measurements of the in-plane signals are defined by

$$S_z(t) = 2S_{\parallel}(t) - S_{\perp}(t) \quad (2.44)$$

where $S_{\parallel}(t)$ and $S_{\perp}(t)$ are transient signals collected with IR polarization parallel and perpendicular to the plane of centrifuge rotation, respectively. Transient measurements of the out-of-plane components are defined by

$$S_x(t) = S_y(t) = S_{\perp}(t). \quad (2.45)$$

The orientational anisotropy $r(t)$ is given as

$$r(t) = \frac{S_z(t)}{S_x(t) + S_y(t) + S_z(t)} = \frac{2S_{\parallel}(t) - S_{\perp}(t)}{2S_{\parallel}(t) + S_{\perp}(t)}. \quad (2.46)$$

A detailed derivation of Equations 2.44 and 2.45 is provided below. The notation used for this derivation is: $t_{\mu}^J \equiv \text{transient}_{\text{transition dipole}}^{\text{angular momentum}}$. For example, t_x^y is a transient signal from a molecule whose transition dipole has a component along the x -axis, and a component of its angular momentum along y -axis.

The optical centrifuge prepares a molecular ensemble with cylindrical symmetry along the z -axis, therefore transient signals from molecules with a component of angular momentum along the x -axis is the same as the signal from molecules with a component along the y -axis. Table 2.1 provides all possible configurations for the in-plane and out-of-plane components.

Table 2.1 Possible configurations of transition dipole and angular momentum vectors for in- and out-of-plane signals.

In-plane	Out-of-Plane
t_x^z	t_z^y
t_y^z	t_y^x
	t_x^y
	t_z^x

The symmetry created by the optical centrifuge yields the following descriptions of in- and out-of-plane signals.

$$\text{In - Plane} = 2t_x^z \quad (2.47)$$

and

$$\text{Out - of - plane} = 4t_y^x. \quad (2.48)$$

In the laboratory, transient signals are collected using two orthogonal IR polarizations. Each IR polarization probes a distinct subset of molecules. The subsets probed by each probe polarization are given by Equations 2.49 and 2.50.

$$S_{\parallel}(t) = t_y^x + t_y^z \quad (2.49)$$

and

$$S_{\perp}(t) = t_z^y + t_z^x \quad (2.50)$$

Equations 2.49 and 2.50 can be rewritten using the cylindrical symmetry created by the optical centrifuge. The result is

$$S_{\parallel}(t) = t_y^x + t_x^z \quad (2.51)$$

and

$$S_{\perp}(t) = 2t_y^x. \quad (2.52)$$

Therefore, in- and out-of-plane signals are written in terms of the two orthogonal polarizations used in the laboratory as

$$\text{In - Plane} = 2t_x^z = 2S_{\parallel}(t) - S_{\perp}(t) \quad (2.53)$$

and

$$\text{Out - of - plane} = 4t_y^x = 2S_{\perp}(t). \quad (2.54)$$

Chapter 3: Spectroscopy and Dynamics of N₂O Super Rotors with $J \leq 205$ Initially Prepared in an Optical Centrifuge

3.1 Introduction

This chapter presents an experimental investigation of the spectroscopy and collisional dynamics of optically centrifuged N₂O molecules. Transient IR absorption spectroscopy was used to measure IR transition frequencies of N₂O high- J states that had not previously been observed. Polarization-sensitive transient absorption spectroscopy was used to measure the time-dependent orientational anisotropy of the centrifuged N₂O molecules. Doppler-broadened transient line profiles were measured to yield translational temperatures for individual rotational states of N₂O. This study focused on the $J = 92$ - 205 states of N₂O with energies of $E_{rot} \approx 3,600 - 17,700 \text{ cm}^{-1}$.

Two previous studies of optically centrifuged N₂O have been reported.^{9, 16} The first study measured new spectral lines with transient IR absorption spectroscopy.⁹ The second measured coherent Raman scattering for the first ~ 500 ps after the centrifuge excitation.¹⁶ The HITRAN database reports IR transition frequencies for N₂O up to the $J = 92$ state.²⁰ Previous experiments from the Mullin group measured new IR transitions of optically centrifuged N₂O up to the $J = 100$ state.⁹ This study reported the appearance of population into rotational states with $J = 87 - 100$. These states were populated through collisions of optically centrifuged molecules. Although the full extent of rotational excitation of the centrifuged molecules was not known at the time, we estimated that states with $J > 270$ ($E_{rot} \approx 30,000 \text{ cm}^{-1}$) were prepared

by the optical centrifuge pulse, based on the spectral bandwidth. The previous data were collected using single-pass IR detection and a pressure of 10 Torr.

To study higher rotational states, we needed to identify state-specific transitions frequencies for rotational states with $J > 100$. We predicted IR frequencies for N₂O *R*-branch antisymmetric stretch ($00^01 \leftarrow 00^00$) transitions with $J > 100$. The rotational energy of a molecule in the ground vibrationless state is a perturbative expansion of the rigid rotor energy given by

$$E_{rot} = BJ(J + 1) - D(J(J + 1))^2 + H(J(J + 1))^3, \quad (3.1)$$

where B is the rotational constant, D is the centrifugal distortion constant, and H is the proportionality constant for third-order term. The rotational energy of a molecule in an excited vibrational state is given by adding the vibrational energy ν_0 to Equation 3.1 and using constants for the excited vibrational state. Known rotational energies of the (00^00) and (00^01) vibrational states up to $J = 92$ were fit to a 3rd order polynomial in $J(J + 1)$. The resulting fitting parameters were used to extrapolate the rotational energies to high- J states. The fitting parameters were found to be $B_0 = 0.419 \text{ cm}^{-1}$, $D_0 = -1.7609 \times 10^{-7} \text{ cm}^{-1}$, and $H_0 = -1.6687 \times 10^{-14} \text{ cm}^{-1}$ for the (00^00) vibrational state and $B_1 = 0.415 \text{ cm}^{-1}$, $D_1 = -1.7547 \times 10^{-7} \text{ cm}^{-1}$, and $H_1 = -1.3351 \times 10^{-14} \text{ cm}^{-1}$ for the (00^01) state. IR transition frequencies for the *R*-branch were determined based on

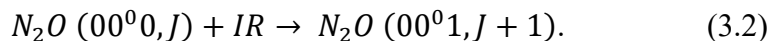


Figure 3.1 shows the Fortrat diagram for predicted IR transition frequencies of the N₂O antisymmetric stretch ($00^01 \leftarrow 00^00$) band. This diagram shows that the IR

probe laser is tunable to N₂O states with $30 < J < 210$. A band head is predicted near $J = 116$.

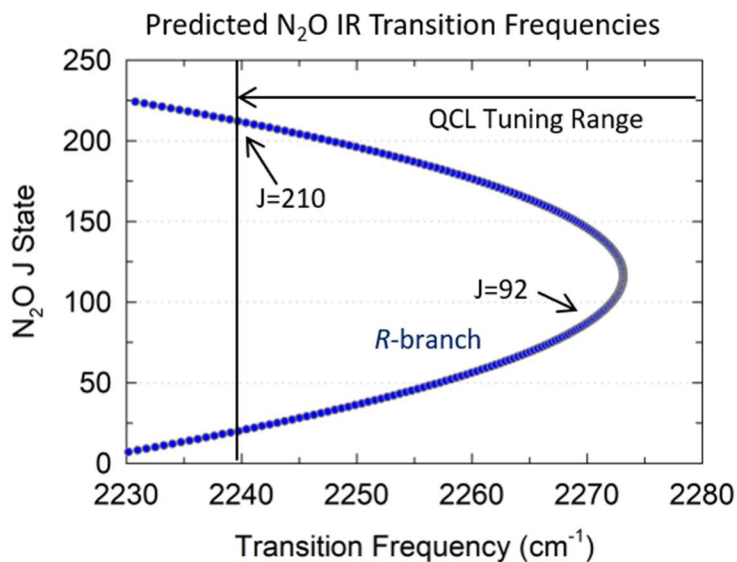


Figure 3.1 The Fortrat diagram for predicted N₂O IR transition frequencies for the antisymmetric stretch ($00^0_1 \leftarrow 00^0_0$) band.

The development of a multi-pass detection setup in 2017 improved signal levels and enabled access to a previously inaccessible regime of states of optically centrifuged N₂O. The multi-pass detection has led to a ten-fold increase in signal-to-noise levels for optically centrifuged CO₂ in $J = 100$.^{14, 15}

The study reported here measured the appearance in N₂O rotational states that are far removed from thermal equilibrium at 300 K. High-resolution transient IR absorption spectroscopy was used to detect a number of transitions for N₂O states with $92 \leq J \leq 205$. State-specific Doppler-broadened line profiles of high- J states were measured to yield J -specific translational energies. These data provide insights into the energy transfer mechanisms of centrifuged molecules and the time-dependent orientational anisotropy of the optically centrifuged molecules. This study lays the groundwork for measuring new IR transition frequencies of high- J molecules and

investigating the energy transfer and reorientation dynamics in a previously inaccessible high energy regime.

3.2 Experimental Details

The details of the optical centrifuge, high-resolution, transient IR absorption spectrometer used in this study are described in Chapter 2. This experiment was performed using the multi-pass detection setup described in Section 2.2.2. A 300 K sample of N₂O was optically centrifuged into extreme rotational states. The cell pressure was 5 Torr, corresponding to a gas kinetic collision time of 20 ns. The optical centrifuge traps and spins a subset of the 300 K distribution to final angular frequencies that are based on the spectral bandwidth of the centrifuge pulse. The spectra of the pulses used in this experiment is shown in Figure 3.2a. One optical component in the beam path of the positively-chirped pulse had a non-reflective coating at 788 nm, leading to an optical trap with a full-width at half-maximum (FWHM) of 4.2×10^{13} rad s⁻¹ as shown in Figure 3.2b.

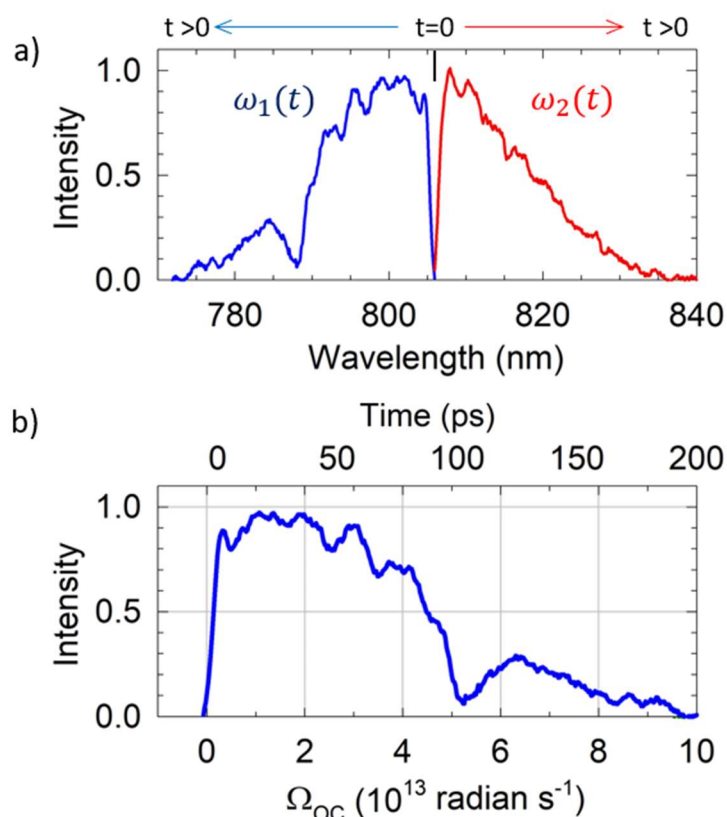


Figure 3.2 a) Spectra of the chirped pulses. b) Optical centrifuge intensity used to rotational excite N_2O .

Polarization-sensitive spectroscopy provides detailed information about the orientation of the centrifuged molecules. The optical centrifuge induces a dipole moment in N_2O that interacts with the electric field of the optical centrifuge (\vec{E}_{OC}) to trap molecules, as shown in Figure 3.3a. The optical centrifuge propagates along the z -axis and prepares rotationally excited N_2O molecules such that they rotate unidirectionally in the xy -plane, as shown in Figure 3.3b. The IR probe beam propagates along the x -axis and has either parallel (\vec{E}_{\parallel}) or perpendicular (\vec{E}_{\perp}) polarization relative to the plane of centrifuge rotation. The combination of measurements using the two orthogonal IR probe polarizations allows the extrapolation of transient measurements with molecules that have angular momentum

components in the x , y , and z directions, referred to as $S_x(t)$, $S_y(t)$, and $S_z(t)$.¹⁵ A description of the deconvolution into the individual components is described in Section 2.2.6.

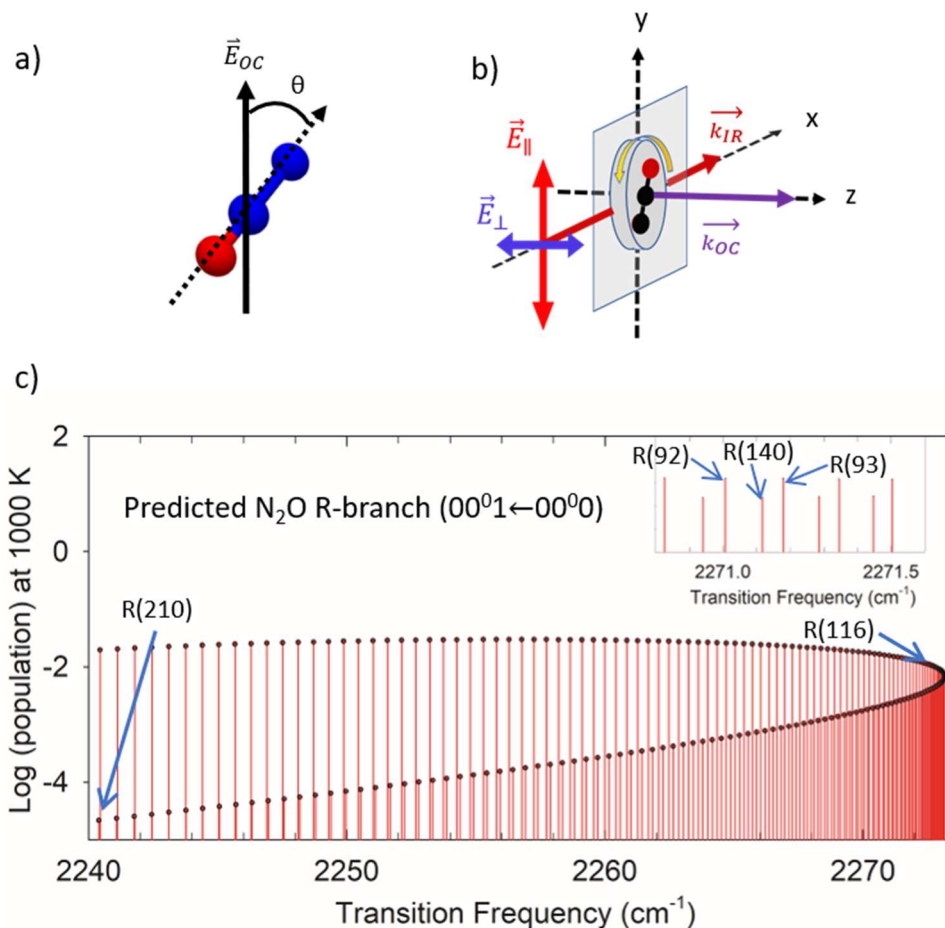


Figure 3.3 a) The optical centrifuge aligns N₂O with the optical field. b) N₂O molecules trapped by the centrifuge rotate in the xy -plane. The IR probe beam propagates along the x -axis and intersects the optical centrifuge beam at 90°. c) Predicted IR transition frequencies for the R-branch absorption of the antisymmetric stretch of N₂O ($00^0_1 \leftarrow 00^0_0$).

IR transition frequencies were determined for $100 < J < 205$ using high-resolution transient fingerprint spectroscopy. Figure 3.3c shows the predicted R-branch transitions up to $J = 210$ based on Equations 3.1 and 3.2 at a sample temperature of 1000 K. A band head is predicted at $J = 116$, thus high- J states have

absorption frequencies found between lower J transitions. Transient fingerprint spectra were recorded by starting at a known N_2O transition and stepping the IR frequency in steps of $\delta_\nu < 0.001 \text{ cm}^{-1}$.

Doppler-broadened line profiles were measured for N_2O states with $J = 92, 160, 180$ and 195 . Polarization-sensitive spectroscopy of the Doppler-broadened line profiles for high- J N_2O states yield translational temperatures, populations, and orientational anisotropies as a function of rotational energy.

3.3 Results and Discussion

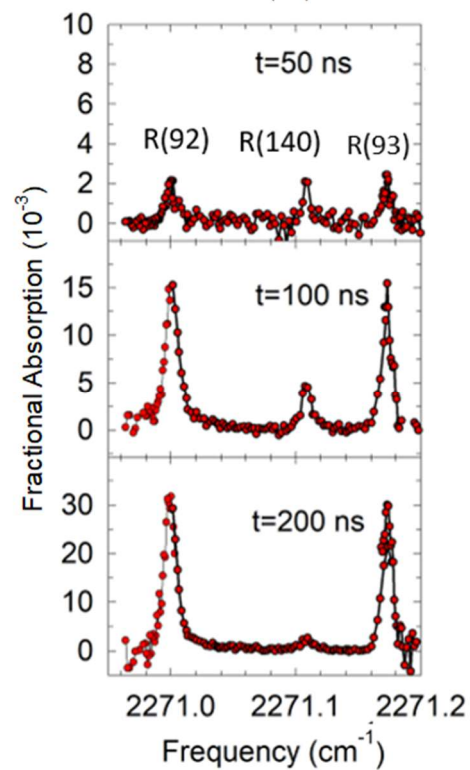
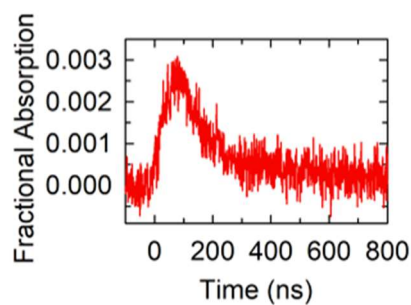
The collision dynamics of N_2O molecules that were rotationally excited by an optical centrifuge are presented here. We used spectral fingerprinting to identify IR transition frequencies for previously unobserved high- J states of N_2O and measured state-specific Doppler-broadened line profiles using polarization-sensitive high-resolution transient IR absorption spectroscopy. The translational temperatures and relative populations were determined from the Doppler profiles. Integrated line profile signals are combined to determine the orientational anisotropy r of individual J states. These results are used to elucidate the energy transfer mechanisms of molecules with extreme amounts of rotational energy.

3.3.1 Spectroscopy of N_2O High- J States

Figure 3.4a shows transient fingerprinting for $R(140)$ of N_2O . The $R(140)$ transition frequency was identified by scanning between the IR frequencies for $R(92)$ and $R(93)$. The time-dependent signals show that the $J = 140$ signal intensity

increases from $t = 50$ to $t = 100$ ns and then decreases at $t = 200$ ns. The $J = 92$ and 93 signal intensities increase ten-fold from $t = 50$ to $t = 200$ ns. This finding illustrates how the centrifuged population relaxes through a collisional cascade toward thermal equilibrium. Figure 3.4b shows transient fingerprinting for the $R(195)$ transition. The $R(195)$ transition frequency was identified using nearby $R(68)$ transitions of the $(01^11 \leftarrow 01^10)$ bend of N_2O . In contrast to the time dependence of the $J = 140$ state, the $J = 195$ signal is most intense at $t = 50$ ns. Fingerprint spectra were measured for six R -branch transitions of N_2O using this approach. Line-center transition frequencies are reported in Table 3.1 along with the predicted values and the differences.

a) R(140)



b) R(195)

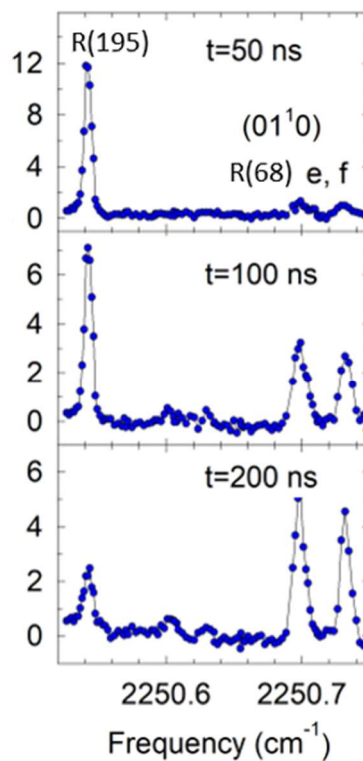
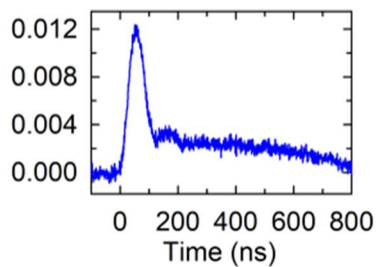


Figure 3.4 Line-center transient absorption measurements with IR probe polarization parallel (\vec{E}_{\parallel}) to the original plane of centrifugation and snapshots of frequency tuned absorption at $t = 50, 100,$ and 200 ns after optical centrifuge excitation for a) $J = 140$ and b) $J = 195$ states.

Table 3.1 Observed and predicted *R*-branch N₂O (00⁰1←00⁰0) IR transition frequencies.

N ₂ O <i>J</i> State	Energy (cm ⁻¹)	ν_{obs} (cm ⁻¹) (± 0.002 cm ⁻¹)	ν_{pred} (cm ⁻¹)	$\nu_{obs} - \nu_{pred}$ (cm ⁻¹)
140	8,300	2271.108	2271.116	-0.008
160	10,800	2266.197	2266.199	-0.002
180	13,600	2258.348	2258.35	-0.002
195	16,000	2250.544	2250.541	-0.003
203	17,300	2245.710	2245.703	0.007
205	17,700	2244.431	2244.42	0.011

The deviations for the line-center transition frequencies are $< \pm 0.012$ cm⁻¹.

The differences for the observed transition frequencies from the predicted are shown in Figure 3.5. These data show that the rigid rotor expansion based on transitions for $J < 92$ is valid as a description for states up to $J = 205$, indicating that the potential energy surface has not changed significantly.

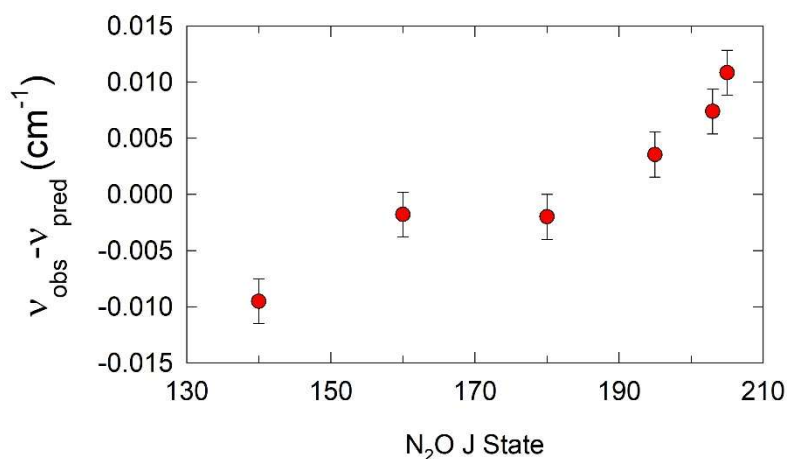
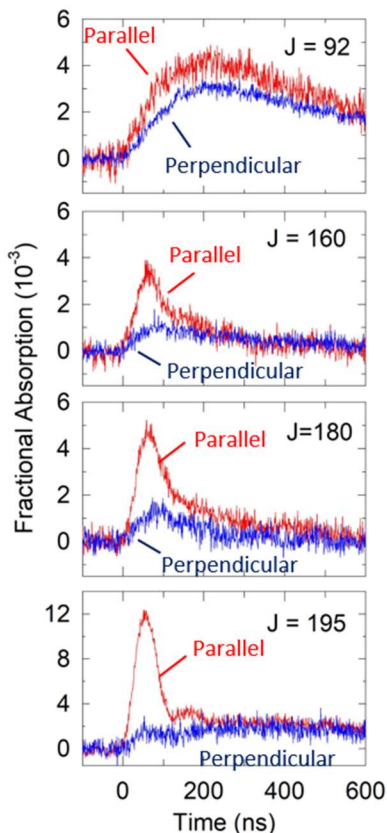


Figure 3.5 Deviations (observed-predicted) for *R*-branch IR transition frequencies of N₂O for $J = 140$ -205.

3.3.2 Polarization-Sensitive Transient IR Absorption Signals of N₂O

Line-center polarization-dependent transient absorption signals for the $J = 92$, 160, 180, and 195 states are shown in Figure 3.6a. The transient signals in Figure 3.6a have been transformed into transient signals that describe the subset of in-plane molecules ($S_z(t)$) and out-of-plane molecules ($S_x(t)$ and $S_y(t)$) shown in Figure 3.6b. The signals show that there are more in-plane molecules than out-of-plane molecules for this set of states out to 200 ns (10 collisions) following the optical centrifuge pulse. These data show that N₂O has a population inversion at $t = 50$ ns, with the highest state probed ($J = 195$) having the largest absorption signal.

a) Parallel (s-pol) vs. perpendicular (p-pol)



b) In- ($S_z(t)$) and out-of-plane ($S_x(t) = S_y(t)$)

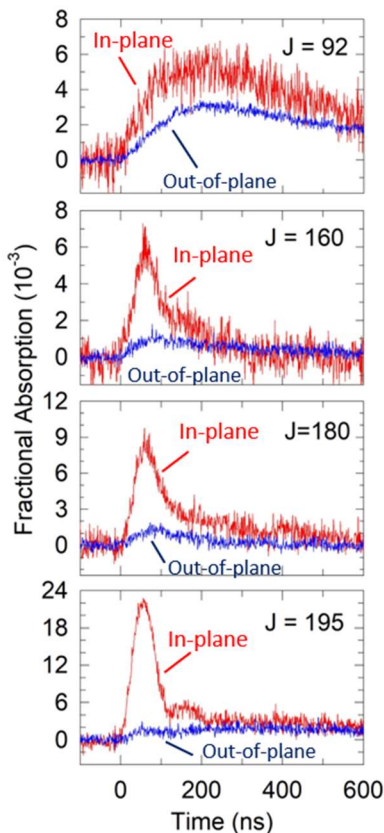


Figure 3.6 a) Polarization-dependent line-center transient measurements for N_2O states with $J = 92, 160, 180, 195$. b) Transient signals resulting from molecules with a component of their angular momentum along the z -axis are denoted as $S_z(t)$ (red) and those along x and y are denoted $S_x(t) = S_y(t)$ (blue).

Figure 3.6b shows that N_2O states with $J = 160, 180,$ and 195 appear promptly after the centrifuge pulse and that the $J = 92$ state is slower to appear since it is populated through collisions. The decay of the transient signals for the states with $J = 160, 180,$ and 195 show two distinct populations, a large prompt component and a slower less intense component. Molecules that are formed in high- J states can result from dropping out of the optical centrifuge trap and as products of collisional energy transfer.

Figure 3.7 shows the J -dependent fractional absorption at three times $t = 50$, 150, and 250 ns. These data illustrate that the population in the high states relaxes through collisions and populates the lower J states. Figure 3.7a shows a population inversion at $t = 50$ ns after the optical centrifuge pulse with large orientational anisotropy for the highest J states. At $t = 150$ ns (or 7-8 gas kinetic collisions), the intensity of the $J = 92$ state increases and the high- J state intensity decreases as the ensemble relaxes. By $t = 250$ ns (or 12-13 gas kinetic collisions), little orientational anisotropy is present of the centrifuged molecules. Interestingly, the $J = 195$ state remains populated after 12-13 collisions. This observation is an indication that the maximum J -state populated by the optical centrifuge is much higher than $J = 195$.

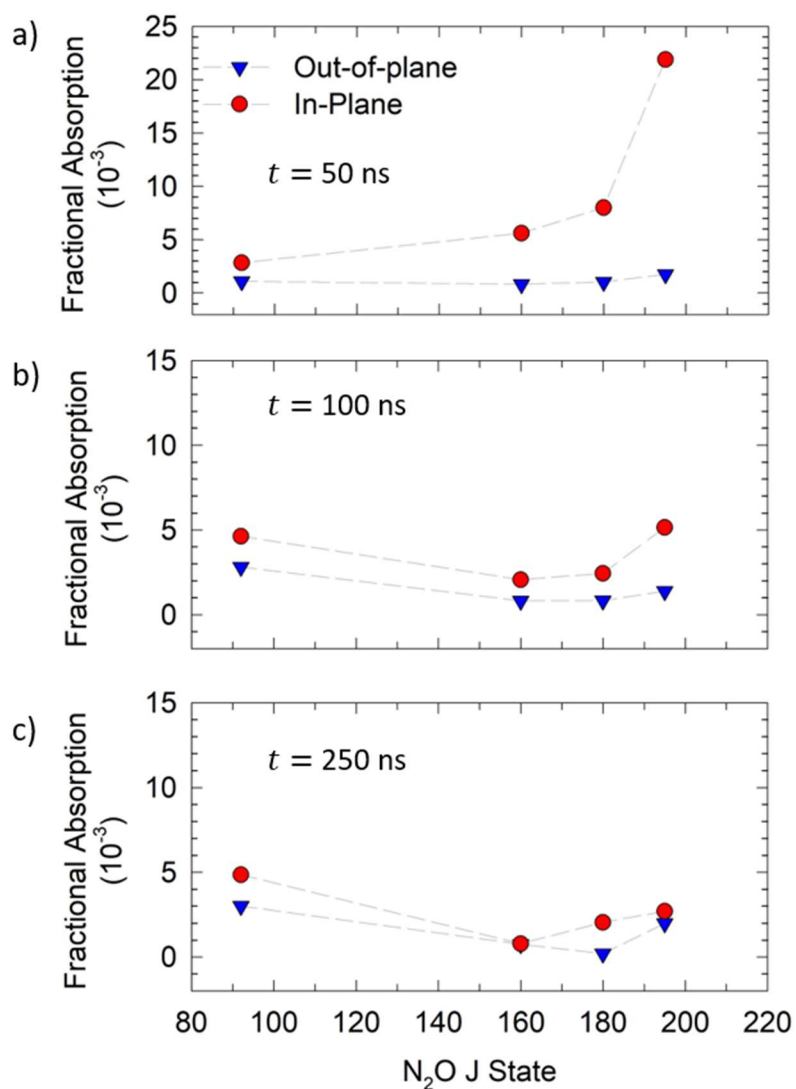


Figure 3.7 J -dependent fractional absorption intensities for N₂O at three times $t =$ a) 50, b) 150, and c) 250 ns after the optical centrifuge excitation. In-plane signals are shown with red circles and out-of-plane are shown with inverted blue triangles. Dotted lines are a guide for the eye.

3.3.3 Polarization-Sensitive Translational Temperatures of N₂O

Polarization-sensitive, Doppler-broadened line profiles measure the translational temperatures and relative populations for in- and out-of-plane N₂O molecules. Doppler-broadened line profiles for the $J = 92, 160, 180,$ and 195 states

are shown in Figure 3.8. A Doppler profile for the $J = 92$ state is shown at $t = 200$ ns, while the profiles for $J = 160$ -195 states are shown at $t = 60$ ns.

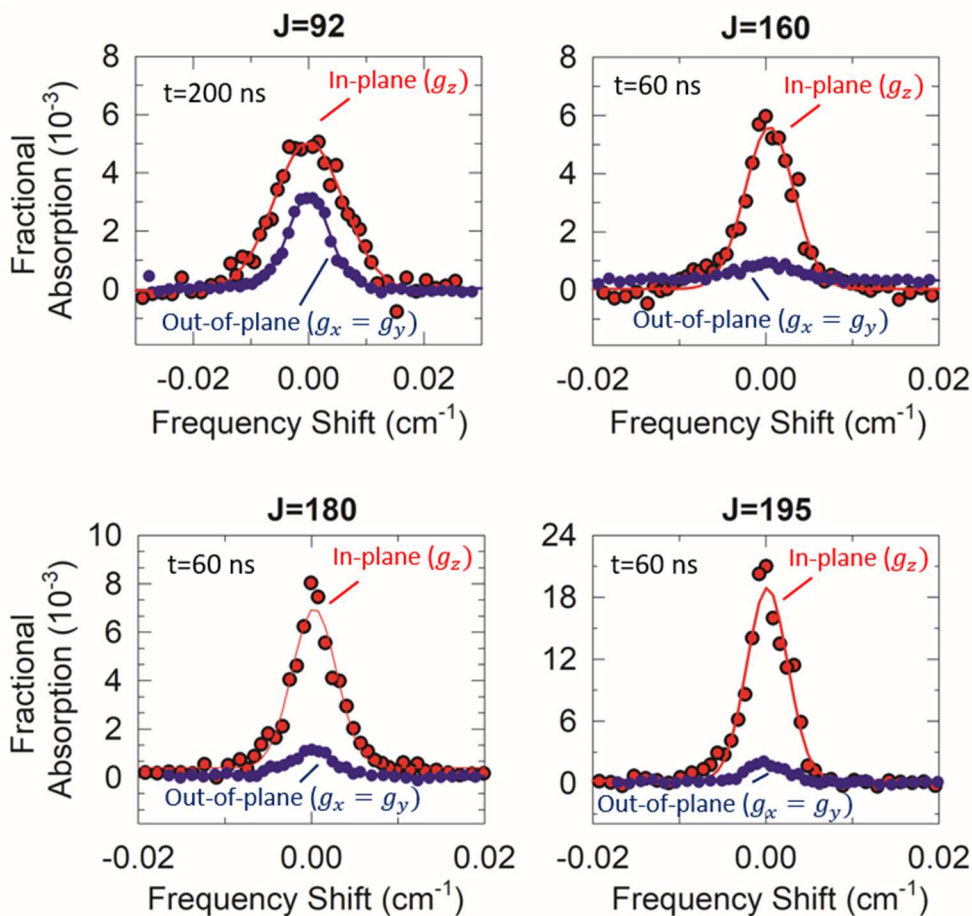


Figure 3.8 Doppler-broadened line profiles for in- and out-of-plane molecules for states with $J = 92, 160, 180, 195$. The $J = 92$ state is shown at $t = 200$ ns after the centrifuge pulse and the $J = 160, 180,$ and 195 are shown at $t = 60$ ns after the centrifuge pulse.

The translational temperature for a given state and at a given time is determined from the width of the Doppler profile. The translational temperatures of the in- and out-of-plane signals are shown in Figure 3.9 for the $J = 92, 160, 180$ and 195 states at $t = 50$ and 100 ns after the optical centrifuge excitation.

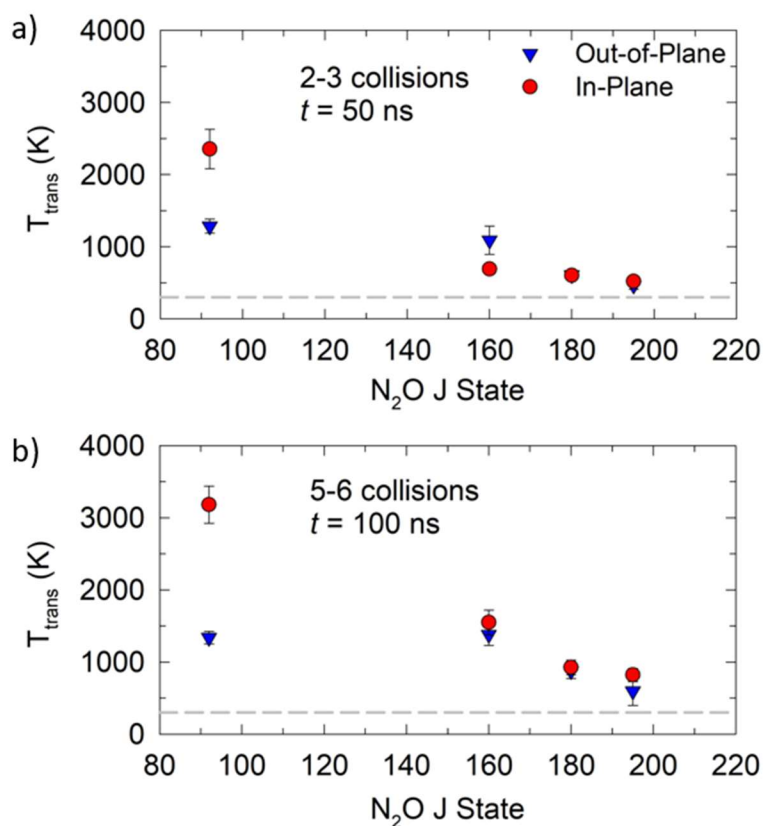


Figure 3.9 Translational temperatures for in- (red circles) and out-of-plane (inverted blue triangles) N_2O molecules in the $J = 92, 160, 180,$ and 195 states at a) $t = 50$ ns, and b) $t = 100$ ns.

State-specific translational temperature measurements for centrifuged N_2O molecules provide insight on the pathways for energy transfer of molecules with extreme amounts of angular momentum. The translational temperature of the in-plane component of the $J = 92$ state is 2500 K at $t = 50$ ns and increases to 3200 K at $t = 100$ ns. The gain in translational energy for the $J = 92$ state is evidence of non-resonant rotation-to-rotation energy transfer. Consider a collision between a N_2O ($J = 200$) donor molecule and a N_2O ($J = 91$) acceptor molecule that involves $\Delta J \pm 1$. The energy down is $\Delta E \approx 167 \text{ cm}^{-1}$ and the energy up is $\Delta E \approx 76 \text{ cm}^{-1}$. Thus, 91 cm^{-1} is available for translation. The in-plane translational temperatures decrease

as a function of J at $t = 50$ ns. The in-plane component of the $J = 195$ state has a translational energy of 600 K at $t = 50$ ns and increases to 750 K at $t = 100$ ns. For all states shown in Figure 3.9, the in-plane molecules gain some amount of translational energy from $t = 50$ ns to $t = 100$.

3.3.4 Orientational Anisotropy Measurements

The population in a given rotational state is measured by integrating the state-specific Doppler-broadened line profile. Polarization-sensitive spectroscopy enables deconvolution to obtain in- and out-of-plane populations from which the orientational anisotropy $r(t)$ of the system is determined by:

$$r(t) = \frac{(2p_{\parallel}(t) - p_{\perp}(t))}{(2p_{\parallel}(t) + p_{\perp}(t))} = \frac{p_z(t)}{p_x(t) + p_y(t) + p_z(t)}. \quad (3.3)$$

Here, $p_{\parallel}(t)$ and $p_{\perp}(t)$ is the relative population for signals collected with IR probe polarization parallel and perpendicular, respectively, and $p_z(t)$ and $p_x(t)$, $p_y(t)$ are the population of in-plane and out-of-plane molecules. The time-dependent orientational anisotropy $r(t)$ is a measure of the extent to which the centrifuged molecules maintain their original orientation.

Figure 3.10 shows the orientational anisotropy for N_2O $J = 92-195$. For the highest state measured ($J = 195$), $r(t)$ is greater than 0.8 at 50 ns (or 2-3 gas kinetic collisions), indicating that the population in this state is predominantly rotating in the xy -plane. After 5 gas kinetic collisions, 80% of the molecules in this state maintain their original orientation. As the system relaxes toward equilibrium, collisions reorient the molecules and the system becomes more isotropic with an ultimate

anisotropy of $r(\infty) = 1/3$. As population appears into the $J = 92$ state, collisions have started to randomize the original orientation of the molecules, as seen with an orientational anisotropy that starts at ≈ 0.6 . The $J = 160 - 195$ states lose population before the anisotropy returns to equilibrium conditions. As an energy accepting state, $J = 92$ has an anisotropy well above $1/3$ beyond $t = 800$ ns.

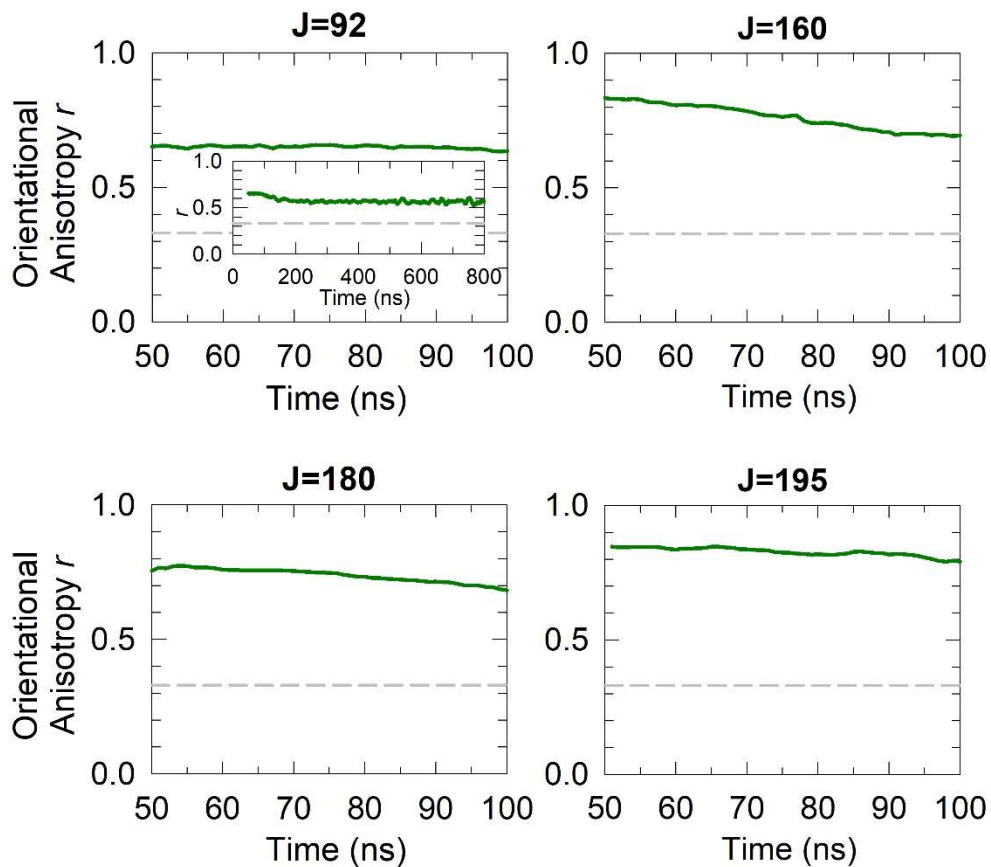


Figure. 3.10 Time-resolved orientational anisotropy of N_2O states with $J = 92, 160, 180,$ and 195 . Orientational isotropy is denoted with a dotted grey line at $1/3$.

These data show that molecules with high rotational energy behave in ways that are consistent with the classical physics of a gyroscope. The Mullin group has previously shown similar behavior for optically centrifuged CO_2 molecules. Polarization-sensitive measurements showed that the lifetimes for orientational

anisotropy decay decreased with increasing J for CO_2 states with $J = 76-100$.¹⁴ Simulations of the relaxation of centrifuged molecules have also found large orientational anisotropies at early times after the centrifuge excitation.^{21,22}

3.4 Conclusion

These experiments highlight that the optical centrifuge can be used to prepare an inverted population distribution of highly rotationally excited molecules. Polarization-sensitive high-resolution transient IR absorption spectroscopy has been used to identify new high- J transition frequencies for N_2O up to $J = 205$. The observed N_2O transition frequencies for states up to $J = 205$ were measured to be within $< \pm 0.012 \text{ cm}^{-1}$ of predicted frequencies, based on low- J spectral constants. This observation shows that low energy rotational models are valid for N_2O states with rotational energies up to $E_{rot} = 17,700 \text{ cm}^{-1}$. The new transitions have been used to investigate the energy transfer dynamics of N_2O molecules with large amounts of rotational energy.

These studies also measured the J -dependent orientational anisotropy of optically centrifuged N_2O . The results illustrate that molecules with larger amounts of angular momentum have larger orientational anisotropy and slower decay constants. The time-evolution of N_2O translational temperatures indicates that the mechanism of energy transfer of highly rotationally excited molecules occurs by near-resonant rotation-to-rotation energy transfer for high- J states and that low- J states have larger translational energies from non-resonant rotation-to-rotation energy transfer.

Chapter 4: High-Resolution Transient IR Absorption Spectroscopy of CO₂ $J = 186$ -280: Observation of Spectral Perturbations

4.1 Introduction

The optical centrifuge coupled to a high-resolution IR absorption spectrometer is used in this chapter to launch CO₂ molecules into extremely high rotational states and to measure their line-center transition frequencies. The spectral lines of high rotational states of CO₂ have been used to study combustion processes, and the atmospheres of Venus and exoplanets.^{17, 23-27} These studies have relied on calculated transition frequencies to identify the high- J CO₂ states. Populating high- J states by thermal heating leads to large amounts of spectral broadening. Spectral broadening makes identification of state-resolved transition frequencies extremely difficult.

State-resolved IR transitions for CO₂ have been reported up to $J = 128$ in the HITRAN database and observed up to $J = 146$ in a flame.^{20, 28} The HITEMP database reports transitions up to $J = 200$ based on semi-empirical calculations. The Carbon Dioxide Spectral Database at 4000 K (CDSD4000) reports IR absorption transitions for CO₂ at 4000 K based on effective Hamiltonian calculations that include 41 vibrational states and 300 rotational states.^{29, 30}

The results in Chapter 3 show that a 3rd-order polynomial expansion of the rigid rotor model is a reasonable approach for predicting high- J transition frequencies of N₂O. The same approach is taken here for CO₂. Known transition frequencies of the CO₂ antisymmetric stretch were used to predict absorption frequencies for higher

J states. The predicted transitions are based on a 3rd-order polynomial expansion in $J(J + 1)$ of the (00^00) and (00^01) states of CO_2 using energies for $J \leq 128$. The expansion is

$$E_{rot} = BJ(J + 1) - D(J(J + 1))^2 + H(J(J + 1))^3. \quad (4.1)$$

The fitting parameters used to extrapolate the CO_2 rotational energies to high- J are $B_0 = 0.3902 \text{ cm}^{-1}$, $D_0 = -1.3337 \times 10^{-7} \text{ cm}^{-1}$, and $H_0 = 1.3285 \times 10^{-1} \text{ cm}^{-1}$ for the (00^00) state, and $B_1 = 0.3871 \text{ cm}^{-1}$, $D_1 = -1.3302 \times 10^{-7} \text{ cm}^{-1}$, and $H_1 = 1.4176 \times 10^{-14} \text{ cm}^{-1}$ for the (00^01) state. The resulting fitting parameters were used to extrapolate the rotational energies to high- J states. IR transition frequencies for the CO_2 R -branch were determined using

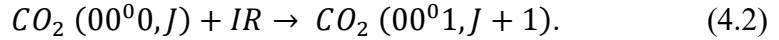


Figure 4.1 shows a Fortrat diagram of the observed and predicted rovibrational transition frequencies for one-quantum absorption in the antisymmetric stretch $(00^01 \leftarrow 00^00)$ of CO_2 . In Figure 4.1, the IR tuning range of the quantum cascade probe laser (QCL) is shown by two vertical black lines, indicating that the P -branch can be probed up to $J < 104$ (up to $E_{rot} \approx 4,200 \text{ cm}^{-1}$) and the R -branch can be probed from $J = 0 - 60$ and $J = 186 - 338$ states ($E_{rot} \approx 13,500 - 44,000 \text{ cm}^{-1}$). The experiments in this chapter focus on probing CO_2 with high- J R -branch transitions.

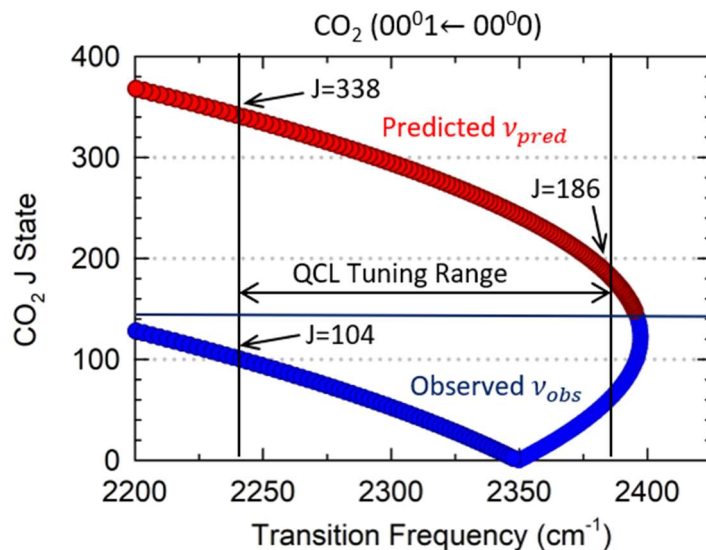


Figure 4.1 A Fortrat diagram of predicted rovibrational IR transition frequencies for the antisymmetric stretch ($00^0 1 \leftarrow 00^0 0$) absorption of CO_2 based on a 3rd-order polynomial expansion in $J(J + 1)$. Previously measured transition frequencies are shown in blue and predicted transition frequencies are shown in red.

The results in Chapter 3 show that the optical centrifuge excites N_2O to $J > 205$, corresponding an optical trap with angular frequency $\Omega_{oc} = 3.2 \times 10^{13} \text{ rad s}^{-1}$. Based on this result, we estimate that CO_2 is spun to $J > 220$. This study seeks to measure transient IR transitions of optically centrifuged CO_2 in high- J states.

The Mullin research group has previously investigated optically centrifuged CO_2 by probing P -branch transitions for states with $J < 104$.^{10-12, 15} In the first of these studies in 2011, single-pass IR detection was used to investigate the collision dynamics of centrifuged CO_2 molecules with $62 \leq J \leq 88$.¹⁰ With the single-pass IR detection, a polarization-sensitive study of the $J = 76$ state of CO_2 state showed that even after 1000 collisions, there was a preference for population to remain in the original plane or rotation.¹¹ In 2015, a J -dependent survey of CO_2 states $0 \leq J \leq 100$ was performed and showed that collisions of centrifuged molecules preferentially involve a translationally cool subset of molecules from the low- J states. In 2017 and

2018, increased signal intensities from a multi-pass detection setup enabled studies of CO₂ $J = 76-100$ that highlighted anisotropic kinetic energy release caused by collisions of centrifuged molecules and the importance of rotational adiabaticity in collisions of centrifuged CO₂ with buffer gases.

In the study reported here, the multi-pass detection setup was used to measure line-center IR transition frequencies for CO₂ high- J states that have not previously been reported. R -branch transition frequencies were measured for CO₂ states with $J \geq 186$ to investigate the extent of rotational excitation in optically centrifuged CO₂. The $J = 186$ state has more than $18,000 \text{ cm}^{-1}$ of rotational energy. Identifying the spectral lines for the high- J states of CO₂ is the first step toward studying the properties and dynamics of CO₂ with large amounts of rotational energy and oriented angular momentum.

4.2 Experimental Details

The optical centrifuge high-resolution transient IR absorption spectrometer used in this study is described in Chapter 2. The optical centrifuge pulse traps a subset of molecules in a 300 K sample of CO₂ and spins it into extreme rotational states and with oriented angular momentum. The ensemble of excited CO₂ is spun to final angular frequencies based on the spectral bandwidth of the optical centrifuge pulse. The spectra of the pulses used for this experiment is shown in Figure 4.2.

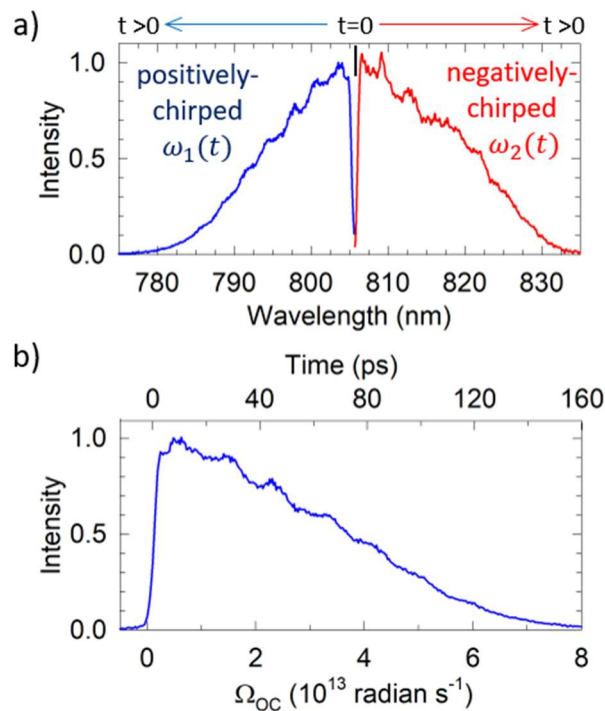


Figure 4.2 a) Spectra of the chirped pulses of the optical centrifuge. b) Optical centrifuge intensity as a function of angular frequency.

High-resolution transient IR absorption spectroscopy was used to measure the line-center transition frequencies for CO_2 states with $J \geq 186$. This study used multi-pass detection as described in Section 2.2.2. Figure 4.3 shows the propagation and polarization geometries of the optical centrifuge pulse and IR probe laser. The optical centrifuge pulse was propagated in the $+z$ direction and spun molecules in the xy -plane. The IR probe beam was propagated in the $+x$ direction and had vertical polarization such that it was parallel to the plane of molecular rotation. The pressure used in this experiment was 5 Torr, corresponding to a gas kinetic collision time of ~ 20 ns.

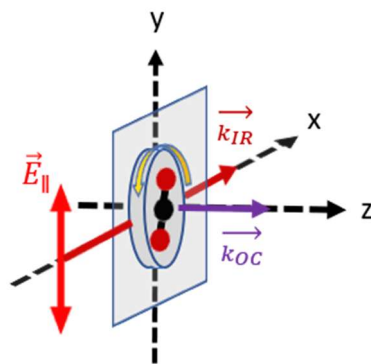


Figure 4.3 Geometry of the optical centrifuge beam and IR probe propagation, IR polarization, and molecular rotation imparted to the CO₂ molecules by the optical centrifuge.

For the individual rotational states measured in this study, the line-center transition frequencies were determined by collecting transient absorption signals at discrete IR frequencies in steps of $\delta_\nu \leq 0.003 \text{ cm}^{-1}$. At each IR frequency step, the IR frequency was determined using a calibrated wavemeter with resolution better than $\Delta\nu_w = \pm 0.001 \text{ cm}^{-1}$. The probe laser resolution is $\Delta\nu_{IR} = 0.0002 \text{ cm}^{-1}$. Figure 4.4a shows examples of transient absorption signals that were used to identify the CO₂ $R(196)$ transition as the IR laser was tuned over the spectral profile. Figure 4.4b shows the fractional absorption at $t = 100 \text{ ns}$ after the centrifuge pulse as a function of IR frequency. A Gaussian function is plotted as a guide to identify the line-center transition frequency. For the $R(196)$ transition, line-center $\nu_0 = 2379.421 \pm 0.003 \text{ cm}^{-1}$. Such scans were collected for 29 R -branch transitions.

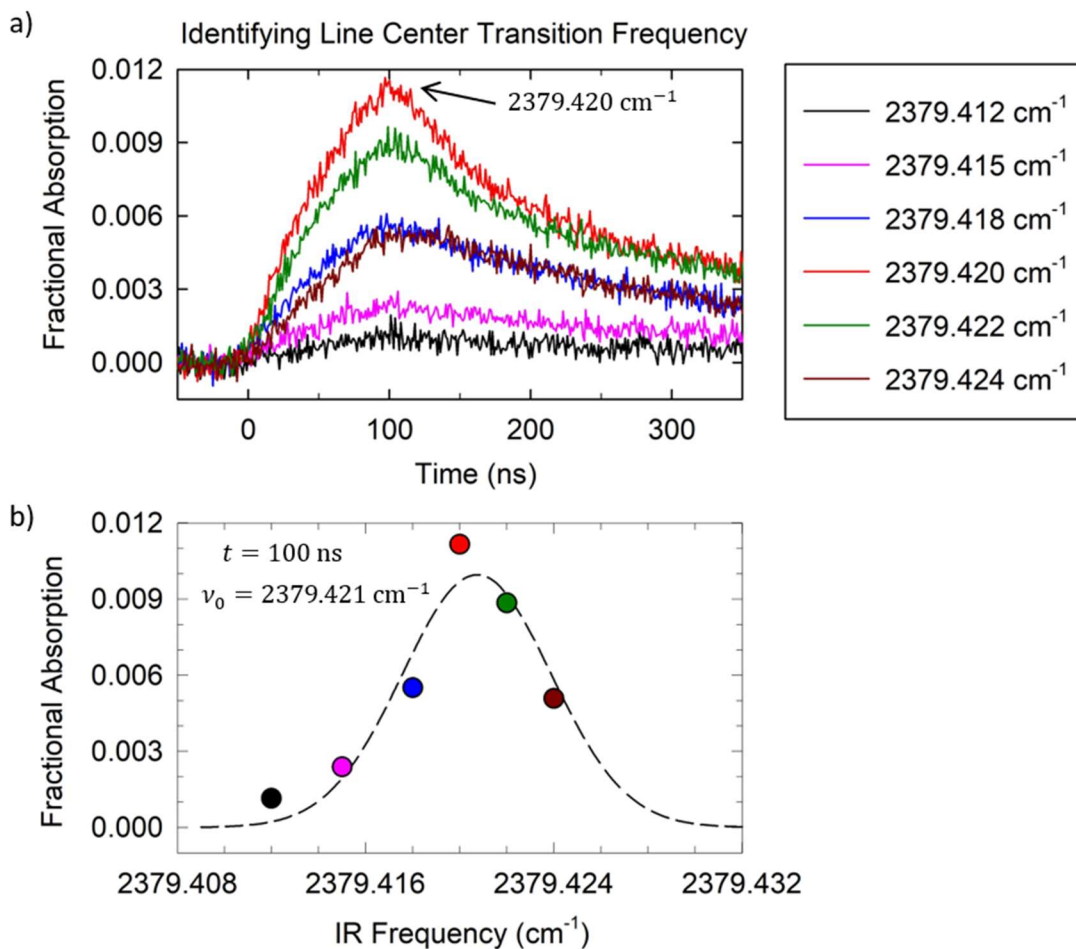


Figure 4.4 a) Transient signals of the CO₂ $R(196)$ transition collected as a function of IR frequencies. b) The signals at $t = 100$ ns are used to identify the line-center frequency. A Gaussian fit is used as a guide to identify line-center.

Figure 4.5a shows transient absorption scans for the $(00^0_1 \leftarrow 00^0_0)$ $R(212)$ and $(01^1_1 \leftarrow 01^1_0)$ $R(56)$ transitions at $t = 90$ and 200 ns after the centrifuge pulse, along with the transient signals near line-center in Figure 4.5b. The transient spectra also give dynamical information. The appearance of the (00^0_0) $J = 212$ state is prompt, showing that it is made directly in the optical centrifuge, followed by collision-induced population loss. In contrast, the appearance of the (01^1_0) $J = 56$ state is much slower and results from rotation-to-vibration energy transfer from collisions of centrifuged molecules.

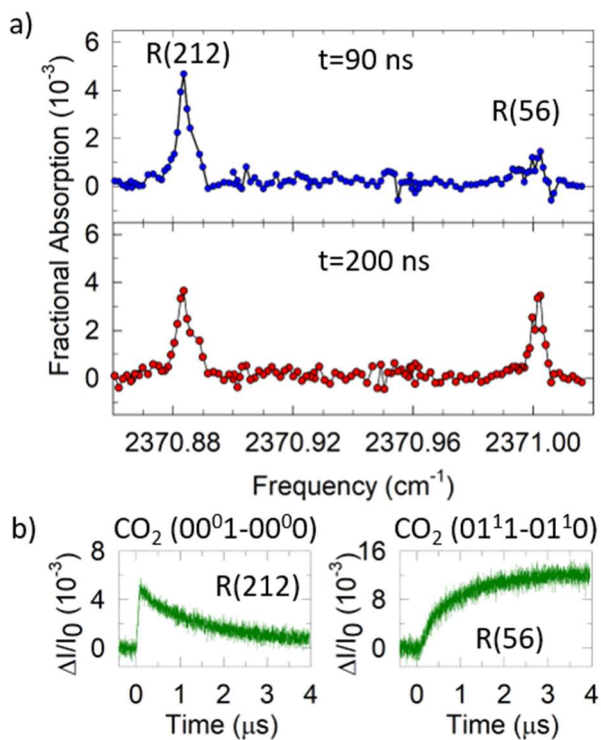


Figure 4.5 a) Spectral fingerprinting of the CO_2 (00^01-00^00) $R(212)$ transition relative to the ($01^{11}-01^{10}$) $R(56)$ transition. b) Line-center transient absorption signals of the (00^00), $J = 212$ state and the (01^{10}) $J = 56$ state.

4.3 Results and Discussion

The IR R -branch transition frequencies for CO_2 states with $J \geq 186$ are identified using an optical centrifuge coupled to a high-resolution transient IR absorption spectrometer. Observed ν_3 rovibrational transition frequencies are compared to predicted rovibrational transition frequencies based on a 3rd-order polynomial expansion in $J(J + 1)$ for rotational energies of the (00^00) and (00^01) states, using known state energies for $J \leq 128$. Spectral perturbations are observed for states with $J > 220$ and the observed frequency shifts are explained using effective Hamiltonian calculations.

4.3.1 IR Transition Frequencies for CO₂ States with $J = 186$ -280

Figure 4.6 presents line-center transient absorption signals for a number of CO₂ states collected at a pressure of 5 Torr. Identifying the transition frequencies for individual CO₂ rotational states began with the $J = 186$ state and proceeded in steps of $\Delta J = 2$. In some cases, overlapping absorption from thermally populated rotational states interfered with the detection of new transitions. For the states shown here, states with $J \leq 228$ have relatively constant signal intensities. The signal intensity for $J = 238$ is larger, consistent with a population inversion for molecules prepared in an optical centrifuge.

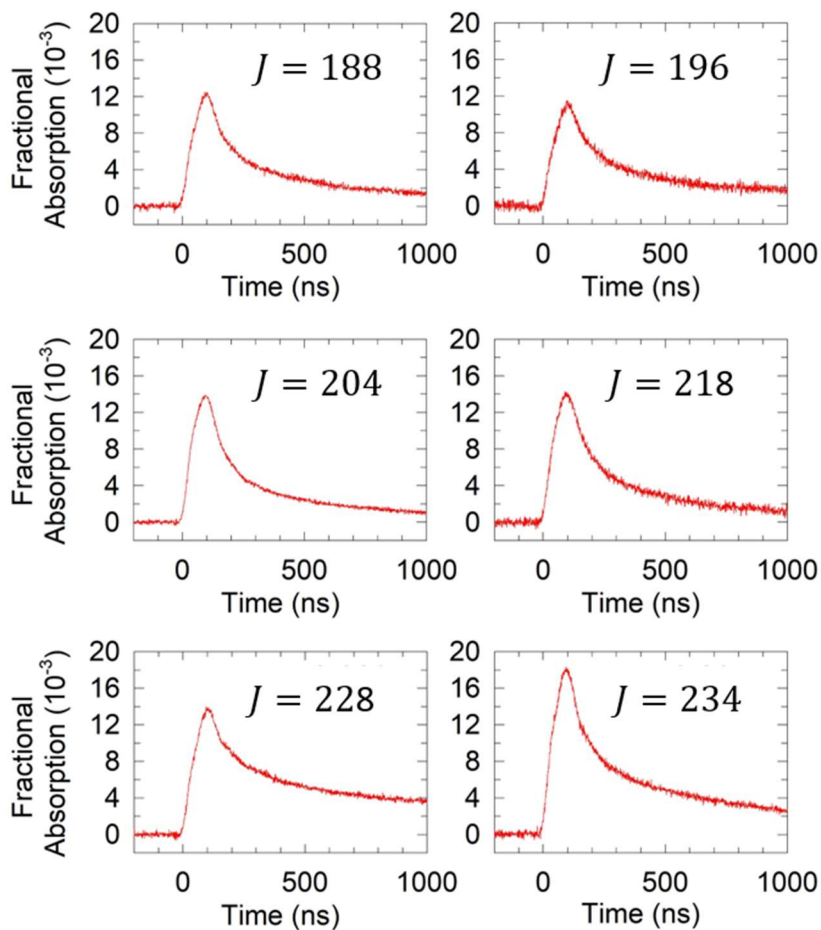


Figure 4.6 Line-center transient absorption signals for a number of CO₂ states with $J = 188$ -234 at a pressure of 5 Torr.

This section describes line-center transient measurements for 22 new CO₂ IR transitions ranging from $R(186)$ to $R(256)$. Figure 4.7 compares the observed CO₂ IR transition frequencies (ν_{obs}) from those predicted by the 3rd-order polynomial expansion in $J(J + 1)$ (ν_{pred}). The transition frequencies for states with $J \leq 218$ are within 0.01 cm⁻¹ of the predicted frequencies. However, starting at $R(220)$ the observed transition frequencies start to deviate exponentially from the predicted transition frequencies up to $R(256)$. The observed deviation for the $R(256)$ transition is 3.2 cm⁻¹.

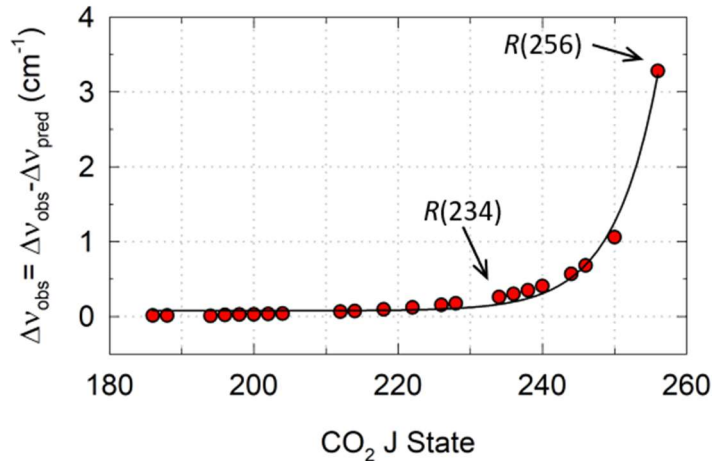


Figure 4.7 Deviations (observed-predicted) in IR transition frequencies for 22 CO₂ states with $186 \leq J \leq 256$.

An exponential fit of the spectral deviations predicted a frequency deviation for the $R(258)$ transition of 4.43 cm⁻¹. However, the $R(258)$ transition was not observed in the laboratory. The deviations from the predicted transition frequencies presented in Figure 4.7 are characteristic of a spectral perturbation. To identify the source of the observed deviations, the calculated rotational energies of the (00⁰0) and (00⁰1) states from the predicted values from the 3rd-order polynomial expansion were compared to CDSD4000.²⁹

Figure 4.8a compares the calculated transition frequencies (ν_{calc}) from the CDSD4000 with the predicted transition frequencies (ν_{pred}). The difference of the calculated and predicted transition frequencies show evidence of two spectral perturbations near $J = 258$ and at $J = 292$. The perturbation at $J = 258$ explains why we were unable to observe the $R(258)$ transition.

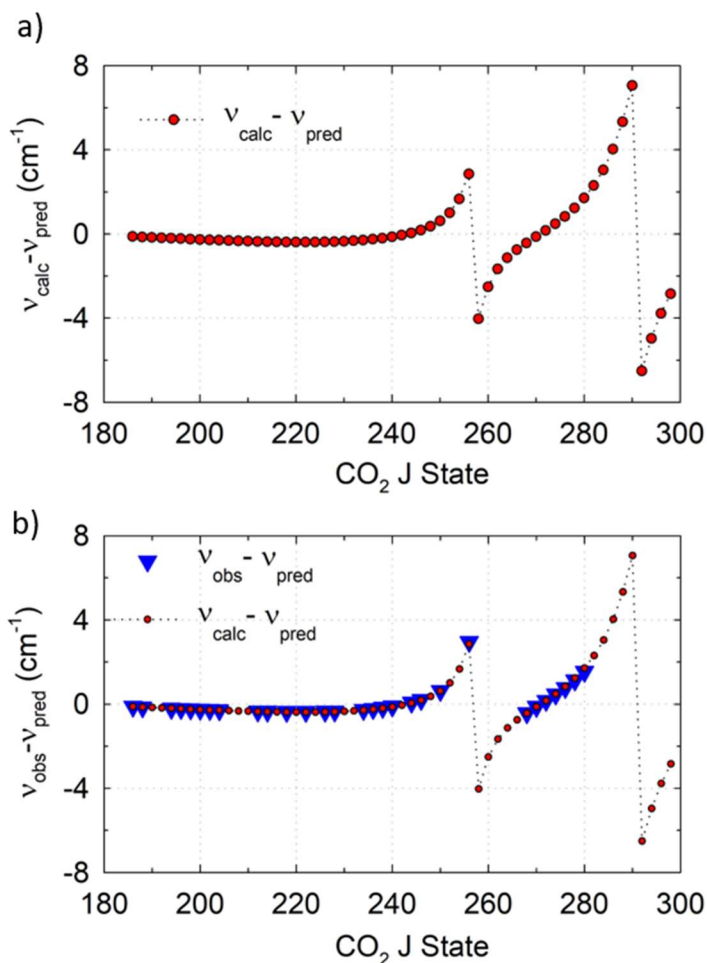


Figure 4.8 a) A comparison of calculated (ν_{calc}) and predicted transition frequencies (ν_{pred}) for CO_2 R-branch transitions. b) A comparison of observed transition frequencies (ν_{obs}) with those calculated using rotational energies reported in the CDSD4000.

Using the calculated frequencies as a guide, we observed the $R(268)$ to $R(280)$ transitions. The $R(258)$ to $R(266)$ transitions remain elusive. Figure 4.7b shows

excellent agreement between the observed transition frequencies (ν_{obs}) and calculated transition frequencies (ν_{calc}). These measurements are evidence that our optical centrifuge is capable of driving CO₂ into rotational states as high as $J = 280$, with an angular frequency of $\Omega_J \sim 4.1 \times 10^{13} \text{ rad s}^{-1}$ and an energy of $E_{rot} \approx 30,000 \text{ cm}^{-1}$. Table 4.1 lists the *R*-branch transitions measured in this study, along with the calculated values and their deviations.

Table 4.1 Observed (ν_{obs}) and calculated (ν_{calc}) IR transition frequencies in the R-branch of the antisymmetric stretch ($00^01 \leftarrow 00^00$) of CO₂ and their differences.

CO ₂ J State	ν_{obs} (± 0.003 cm ⁻¹)	ν_{calc} (cm ⁻¹) ^a	$\Delta\nu_{obs} - \Delta\nu_{calc}$ (cm ⁻¹)
186	2383.921	2383.914	0.008
188	2383.070	2383.065	0.005
194	2380.360	2380.365	-0.005
196	2379.421	2379.413	0.008
198	2378.443	2378.435	0.008
200	2377.441	2377.432	0.009
202	2376.413	2376.402	0.011
204	2375.359	2375.347	0.012
212	2370.885	2370.87	0.015
214	2369.704	2369.688	0.016
218	2367.267	2367.247	0.020
222	2364.730	2364.707	0.023
226	2362.095	2362.071	0.024
228	2360.743	2360.717	0.026
234	2356.552	2356.522	0.030
236	2355.113	2355.083	0.030
238	2353.658	2353.625	0.033
240	2352.186	2352.151	0.035
244	2349.208	2349.172	0.036
246	2347.712	2347.682	0.030
250	2344.796	2344.78	0.016
256	2341.879	2341.775	0.104
268	2327.177	2327.168	0.009
270	2325.475	2325.466	0.009
272	2323.728	2323.73	-0.002
274	2321.958	2321.979	-0.021
276	2320.175	2320.227	-0.052
278	2318.398	2318.494	-0.096
280	2316.637	2316.803	-0.166

^a Tashkun, S. A.; Perevalov, V. I., CDS-4000: High-resolution, high-temperature carbon dioxide spectroscopic databank. *Journal of Quantitative Spectroscopy & Radiative Transfer* **2011**, *112* (9), 1403-1410.

4.3.2 Identifying the Origin of the Perturbations

Figure 4.9 is a Fortrat diagram of the *R*-branch transitions for the $(00^01 \leftarrow 00^00)$ absorption band of CO_2 , based on the energies reported in the CDSD4000. The Fortrat diagram shows discontinuities in the *R*-branch spectrum for CO_2 states near $J = 258$ and $J = 292$. To understand the vibrational states responsible for the perturbations, the CDSD4000 (00^00) and (00^01) energies were fit to a 3rd-order polynomial expansion in $J(J + 1)$ with $J \leq 300$. The results were used to predict unperturbed high- J energies for both vibrational states. The deviations from the calculated and predicted energies are shown in Figure 4.9. The (00^00) state in Figure 4.10a shows no J -dependent structure, but the (00^01) state in Figure 4.10b shows distinct energy deviations near $J = 259$ and $J = 293$. The (00^01) state is coupled to other CO_2 vibrational states, thus leading to perturbations in the *R*-branch transitions.

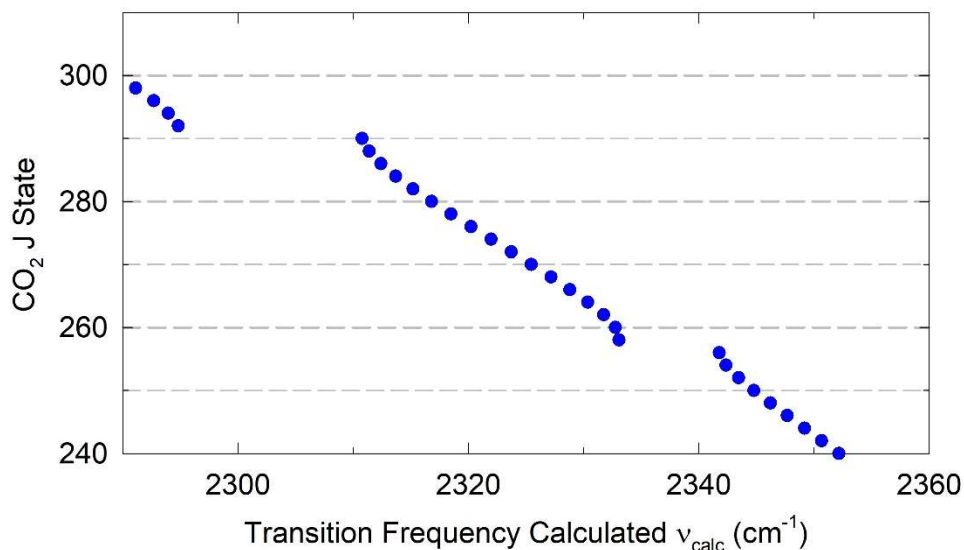


Figure 4.9 A Fortrat diagram of calculated IR transition frequencies based on rotational energies of the (00^00) and (00^01) states reported in the CDSD4000.

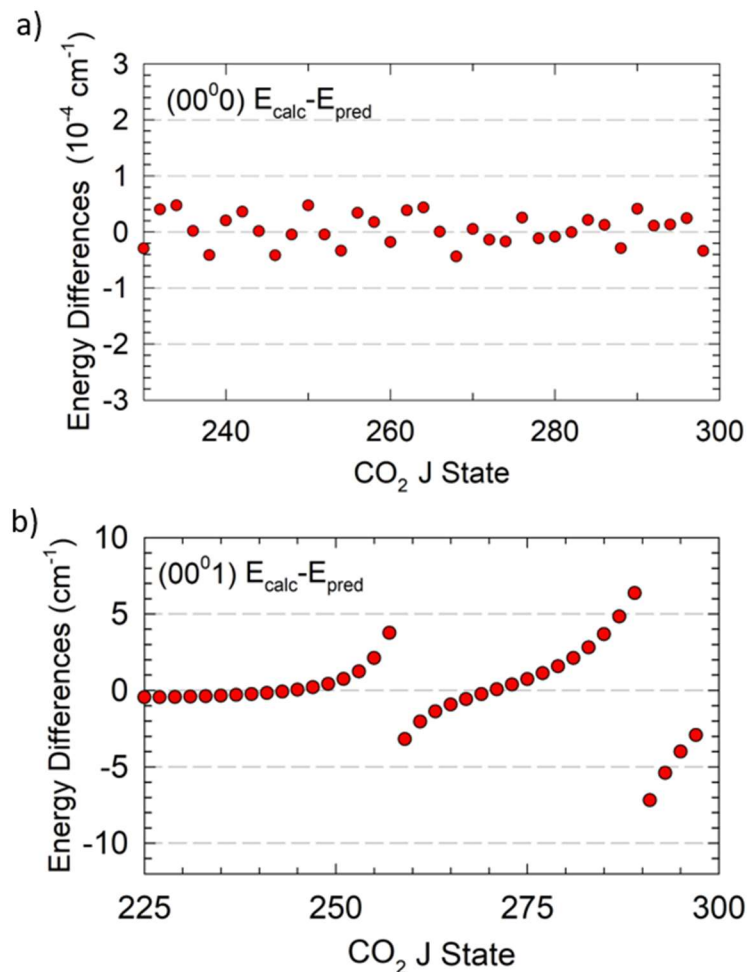


Figure 4.10 Deviations for calculated and predicted rotational energies for the a) (00^0) states and b) (00^1) state.

The rotational energies for the (00^0) and (00^1) vibrational states reported in the CDSD4000 are based on an effective Hamiltonian. The effective Hamiltonian for CO₂ was developed using a polyad structure of vibrational states.³¹ The model accounts for three interacting vibrational states of CO₂ that interact with the (00^1) state. The interacting vibrational states are (03^3_0) , $(11^1_0(1))$, and $(11^1_0(2))$ where (1) and (2) identify Fermi-mixed states. Based on this model, energy level crossings are present near the $J = 259$ rotational state of the (00^1) and (03^3_0) vibrational states and near the $J = 291$ rotational state of the (00^1) and $(11^1_0(1))$ vibrational states. The

(11¹0(2)) state interacts indirectly through the (03³0) state. Based on the effective Hamiltonian, the authors identify Fermi, Fermi + L-type, and Coriolis coupling as being responsible for the perturbation.

The energy level crossings are illustrated here. Figure 4.11a shows the energies of the (00⁰1) and (03³0) states and shows that the energies cross near the $J = 259$ state. Figure 4.11b plots the energies of the (00⁰1) and (11¹0(1)) states to show the crossing near the $J = 291$ state. The results presented here are the first high-resolution look at the state coupling of high rotational states based on interactions with vibrationally excited states.

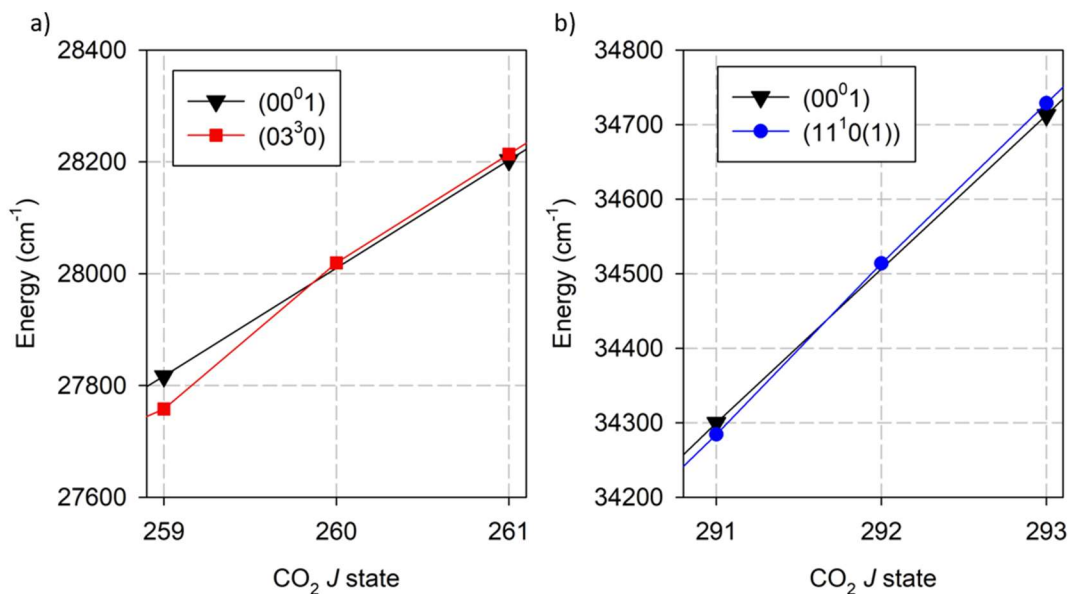


Figure 4.11 Energy-level crossings for the a) (00⁰1) and (03³0) states and b) (00⁰1) and (11¹0(1)) states.

4.4 Conclusion

This study has measured new IR transitions of optically centrifuged CO₂ molecules for $J = 186$ to 280. In this study, spectral line positions were identified for

29 new *R*-branch transitions with rotational energies $E_{rot} \approx 13,500 - 30,000 \text{ cm}^{-1}$. These results lay the foundation for future studies to detect high-*J* molecules, to measure the collision dynamics of rotationally excited molecules and to investigate the dynamics of mixed states, such as those seen in the spectral perturbations reported here.

Chapter 5: Characterization and Collision Dynamics of Optically Centrifuged CO

5.1 Introduction

The optical centrifuge traps and spins molecules into extreme rotational states. The extent of rotational excitation is dependent on the spectral bandwidth of the optical centrifuge pulse. One estimate of the rotational energy imparted to the trapped molecules is based on the full-width at half-maximum (FWHM). Based on this estimate, we anticipated that the optical centrifuge rotationally could excite CO molecules to a rotational quantum state of $J \approx 50$ with energy $E_{rot} \approx 4,900 \text{ cm}^{-1}$. IR probe transition frequencies are known for CO states up to $J = 93$.³² This chapter describes experiments designed to identify and characterize the full distribution of optically centrifuged CO molecules using high-resolution transient IR absorption spectroscopy.

In the Mullin research group, an early spectroscopic study of optically centrifuged CO was performed using single-pass IR detection.¹³ One challenge of this study was that visible emission was observed when the optical centrifuge was operated at full power. The source of the emission was determined to be the C₂ Swan bands, showing that the optical field was intense enough to initiate reactions of CO that ultimately form C₂. To avoid emission that interfered with transient IR spectroscopy, the previous experiments were performed using reduced optical centrifuge power and a cell pressure of 10 Torr. The CO $J = 29$ -39 states were investigated, but they did not show a population inversion that one expects for an

optically centrifuged sample. In addition, transient Doppler profiles revealed that the $J = 29-39$ states had high translational temperatures resulting from non-resonant rotation-to-rotation collisional energy transfer. These results clearly show that the centrifuged sample had already undergone substantial collisional relaxation at the time of the IR probe.

The experiments reported in this chapter have the advantage of increased signal-to-noise levels, due to the development of a multi-pass IR detection cell in which the IR probe crosses the optically centrifuged sample 11 times. With increased signal-to-noise levels, we were able to reduce the CO pressure to as low as 2.5 Torr. The decrease in pressure enabled the use of a more intense optical trap, resulting in larger number densities of rotationally excited CO molecules while avoiding collisional relaxation and reactions that form C₂.

In this study, IR probe transition frequencies for CO with $J = 29-80$ were identified using high-resolution transient IR absorption spectroscopy. Polarization-sensitive IR absorption spectroscopy was used to characterize the full distributions of optically centrifuged CO made with two different spectral bandwidths of the optical centrifuge. Doppler-broadened line profiles were measured to characterize the energy transfer dynamics of the nearly-nascent distribution. Directly measuring the extent of rotational excitation from optical centrifuge excitation provides important information about the ultimate angular frequencies for other molecules in an optical centrifuge.

5.2 Experimental Details

The instrumental set up for the optical centrifuge high-resolution transient IR absorption spectrometer is described in Chapter 2. In this study, two different spectral bandwidths were used to rotationally excite CO to high- J states with oriented angular momentum. Spectrum-I (SI) is shown in Figure 5.1a and Spectrum-II (SII) is shown in Figure 5.1b. For SI, the positively-chirped pulse had an accidental drop in optical intensity at ~ 788 nm caused by reduced reflectivity from damage on a dielectric coating after the pulse shaper. The pulse energy for each of the pair of chirped pulses are shown in Figures 5.1a and 5.1b. In Figures 5.1c and 5.1d, the intensities of the related optical centrifuge pulses are shown as a function of the optical angular frequency Ω_{OC} . State-specific, polarization-sensitive transient IR absorption measurements were collected to identify distributions and orientational anisotropies of the optically centrifuged CO. A quantum cascade laser (QCL) operating at $\lambda = 4.3 \mu\text{m}$ was used to probe CO ($1 \leftarrow 0$) R -branch transitions for $J = 29-80$.

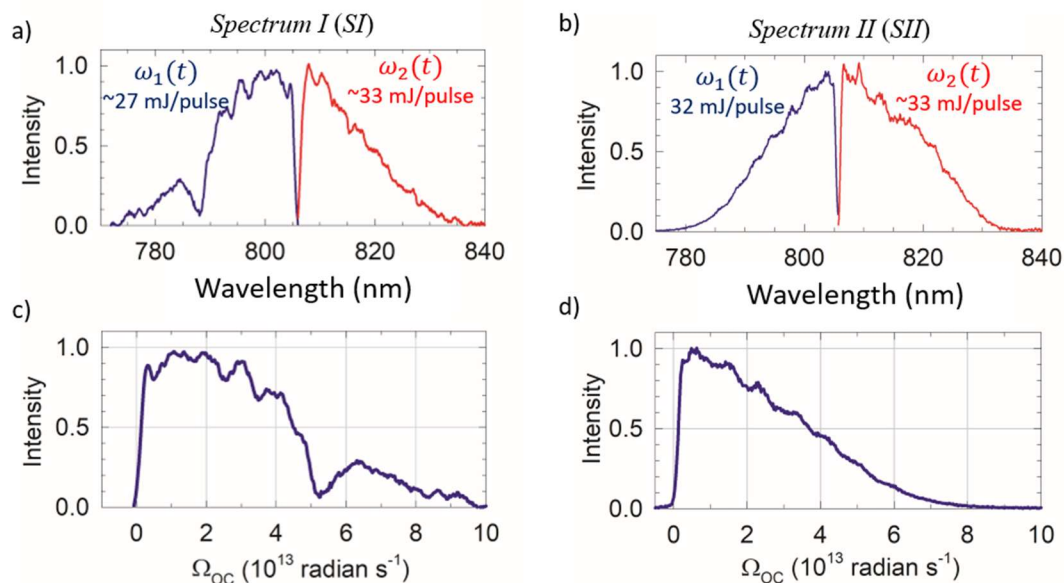


Figure 5.1 Chirped pulse spectra for a) Spectrum I and b) Spectrum II. Optical damage to a reflector led to a drop in intensity near $\lambda = 788$ nm of SI. Optical centrifuge intensities for c) SI and d) SII as a function of trap angular frequencies.

Transition frequencies for CO states with $J > 58$ have not been reported previously in the HITRAN database. However, CO states have been reported by Guelachvili and coworkers up to $J = 93$ and $v = 41$.³² Dunham coefficients have been reported that describe rovibrational energies for diatomic molecules based on expansions of rotational and vibrational energies and their couplings. IR transition frequencies up to $J = 100$ for CO were calculated using their Dunham coefficients and are listed in Appendix I.

Figure 5.2 shows a Fortrat diagram of the predicted transition frequencies for CO J states with $J = 0-100$ based on the Dunham coefficients. The tuning range for the QCL enables IR probing with CO R-branch transitions from $J = 29$ to beyond $J = 100$, as indicated by the two vertical black lines.

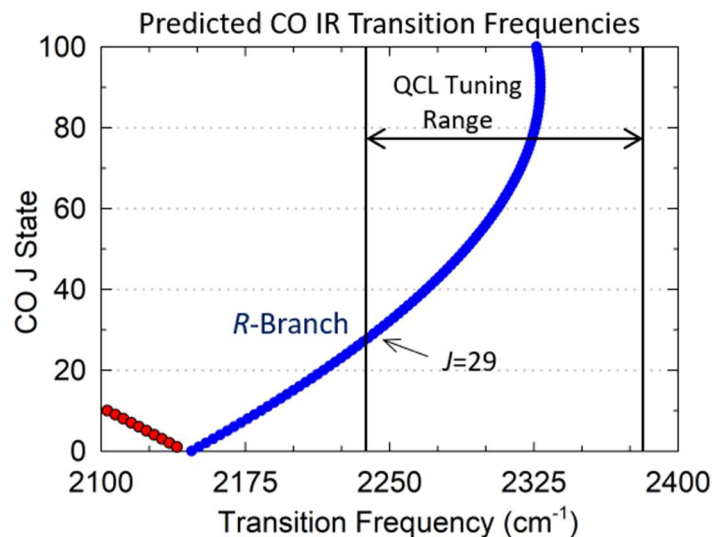


Figure 5.2 Predicted IR transition frequencies for CO for rotational states up to $J = 100$ based on Dunham coefficients of the rotational energies of the ground and first excited vibrational states.

The overlap of the CO transitions with the IR probe laser tuning range made CO an attractive candidate for this study. However, the IR absorption strength for CO is a factor of 9 weaker than for CO₂, and some experiments had low signal-to-noise levels.

In the first set of experiments, a centrifuge with the SI bandwidth (Figure 5.1a) was used to rotationally excite CO with a cell pressure of 5 Torr, corresponding to a gas kinetic collision time of 20 ns. Polarization-sensitive transient IR absorption signals were collected for CO states with $J = 29-67$ to characterize the full distribution of optically centrifuged CO. Polarization-sensitive signals were converted to in- and out-of-plane signals to distinguish molecules with in-plane angular momentum components from those with out-of-plane components. The conversion to in-plane and out-of-plane signals is described in Section 2.2.6.

In the second experiment, the SII bandwidth (Figure 5.1b) was used to excite CO molecules to high- J states. The distribution of optically centrifuged molecules was further characterized by measuring polarization-sensitive absorption signals for CO states with $J = 62-78$ at a reduced pressure of 2.5 Torr.

Finally, state-specific Doppler-broadened line profiles were measured for eight different CO rotational states with $J = 62-80$. These measurements were performed using a CO pressure of 5 Torr and with an IR probe polarization that was parallel (s-pol) to the plane of centrifuge rotation.

5.3 Results and Discussion

Here we present the results from transient IR absorption measurements of optically centrifuged CO. We characterized the distribution of CO prepared by two different optical centrifuge spectral bandwidths, SI and SII. Using both spectral bandwidths, the extent of rotational excitation was measured by high-resolution transient IR absorption spectroscopy. Time-resolved Doppler-broadened line profiles were measured for a number of CO states using SII bandwidth.

5.3.1 CO Excited in an Optical Centrifuge with SI Bandwidth

Figure 5.3 presents in- and out-of-plane absorption signals for CO prepared by the optical centrifuge with SI bandwidth (Figure 5.1a). The in-plane signals arise from molecules with a component of their angular momentum along the z -axis and the out-of-plane signals correspond to molecules with angular momentum components along the x - or y -axis. Transient absorption signals are shown for nine

CO rotational states with $J = 29-66$. The in-plane signal intensities increase from the $J = 29$ state to the $J = 62$ state, and then decrease for states with $J > 62$. The out-of-plane absorption signal intensities are significantly smaller than the in-plane signals and are relatively J -independent.

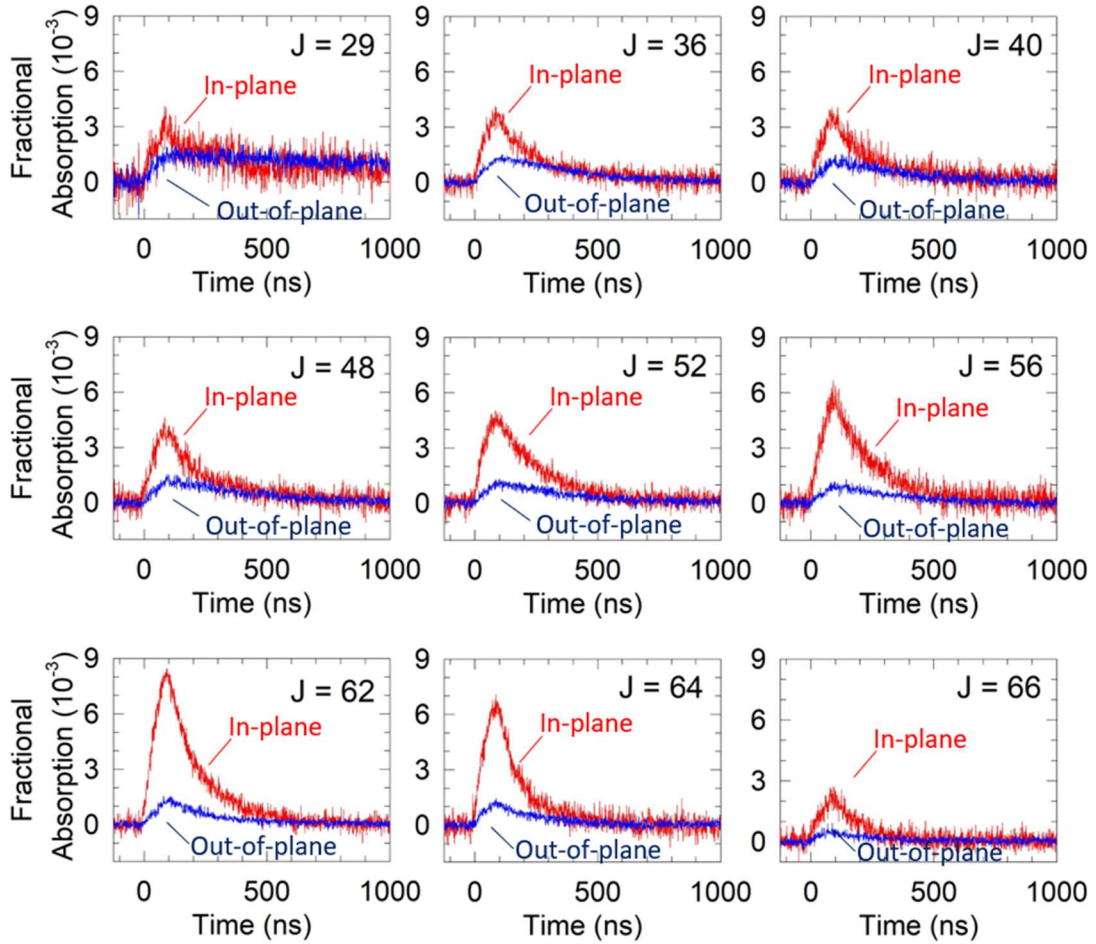


Figure 5.3 In- ($S_z(t)$) and out-of-plane ($S_x(t)$ and $S_y(t)$) transient IR absorption signals for CO states with $J = 29-66$ prepared using the optical centrifuge with SI.

Figure 5.4 shows the orientational anisotropy $r(t)$ after 5, 10, and 15 gas kinetic collisions given by

$$r(t) = \frac{S_z(t)}{S_x(t) + S_y(t) + S_z(t)} \quad (5.1)$$

An isotropic sample has an $r(\infty) = 0.33$, as shown by a horizontal dashed line in Figure 5.4. The CO states with $J > 55$ have $r \approx 0.75$ after 5 collisions corresponding to 100 ns. These values decrease to $r \approx 0.65$ after 15 collisions (300 ns) with the exception of $J = 64$, which has $r \approx 0.5$ at this time. In comparison, the lowest state measured ($J = 29$) has $r \approx 0.5$ after 5 collisions (100 ns) and drops to $r \approx 0.33$ after 15 collisions (300 ns). These data illustrate that molecules with more angular momentum take a longer time to reorient themselves.

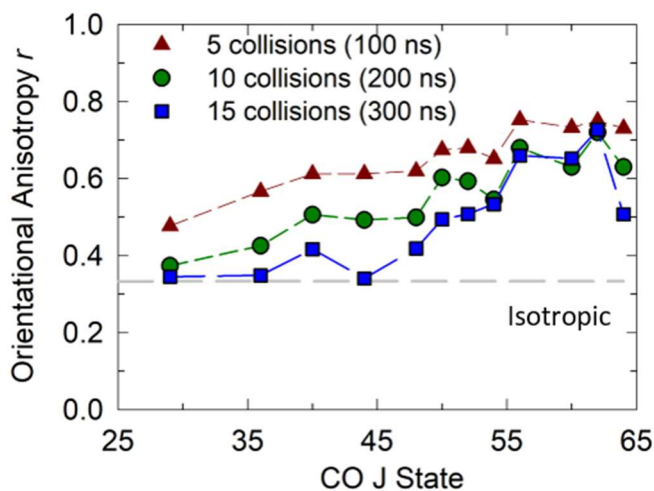


Figure 5.4 Orientational anisotropy $r(t)$ based on line-center transient absorption signals. $S/N < 1$ are not included. A dashed grey line shows the $r(\infty) \approx 0.33$ for an isotropic distribution.

This survey study was used to identify the most populated J -states after the centrifuge pulse excitation, based on the peak intensities from Figure 5.3. Most transient signal intensities peak near $t = 100$ ns. These intensities at $t = 100$ ns are plotted in Figure 5.5a. The in-plane signals show an overall population inversion, with the $J = 62$ intensity three times larger than those for $J = 29$. The out-of-plane measurements are nearly J -independent and are much less intense than the in-plane.

At $J = 62$, the in-plane intensities are eight times larger than the out-of-plane. Some in-plane intensity measurements appear smaller than expected based on the overall population inversion. This set of data was collected as a survey scan and did not include a common reference state. Nevertheless, the population inversion near $J = 62$ is clear. In-plane and out-of-plane intensity comparisons have uncertainties less than 10%. For this set of data, intensity comparisons between J states have uncertainties as high as 30%.

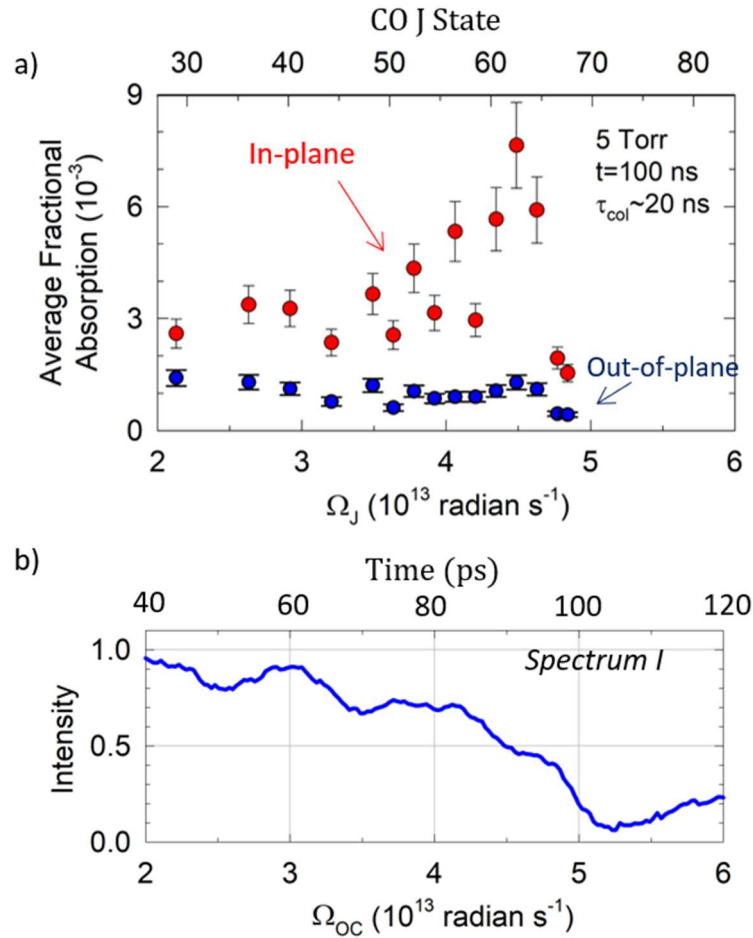


Figure 5.5 a) The distribution for in- (red) and out-of-plane (blue) CO signals at 5 Torr. b) Spectral intensity of SI vs the angular frequency of the optical field.

Figure 5.5b shows the spectral intensity of the optical field used to rotationally excite CO as a function of the optical angular frequency Ω_{OC} . A trapped molecule rotates with the same angular frequency as the optical field, such that $\Omega_J = \Omega_{OC}$. The relative intensity of SI decreases from 0.5 at $\Omega_{J=62}$ to less than 0.1 at $\Omega_{J=7}$. The decrease in the optical field intensity is consistent with the decreasing signals for states with angular frequencies $> 4.5 \times 10^{13} \text{ rad s}^{-1}$. Once the trap has reached $\Omega_{oc} = 5.0 \times 10^{13} \text{ rad s}^{-1}$, the intensity of the field is no longer sufficient to retain the molecules in the field. This result is the first experimental indication in our laboratory of the minimum pulse intensity required to keep molecules in the optical trap.

5.3.2 CO Excited in an Optical Centrifuge with SII Bandwidth

A second set of studies was performed to measure optically centrifuged CO molecules with an uninterrupted spectral bandwidth and at a reduced pressure. The optic with a damaged dielectric coating used for SI studies was replaced and the CO distribution was again characterized. Figure 5.6 shows polarization-sensitive transient IR absorption signals for CO states with $J = 62, 73, \text{ and } 80$ at a pressure of 2.5 Torr. The transient signals were collected using IR probe polarization that was parallel (s-pol) and perpendicular (p-pol) to the plane of centrifuge rotation. For these data, the perpendicular signals are smaller than the parallel signals and are relatively J-independent.

For these measurements, the signals were not converted to in- and out-of-plane signals for all times, because of the low signal intensities of the perpendicular

measurements. Instead, the peak intensities of the parallel and perpendicular data were converted to in- and out-of-plane signals.

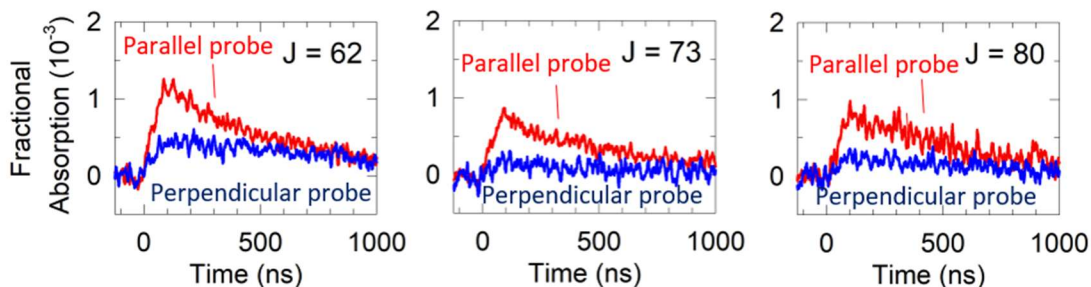


Figure 5.6 Transient absorption signals using IR probe polarization parallel (red) and perpendicular (blue) to the plane of centrifuge rotation. Shown are CO states with $J = 62$, 73 , and 80 at a CO pressure of 2.5 Torr. These signals were measured for optically centrifuged CO prepared with the SII bandwidth.

Figure 5.7a shows the fractional absorption at the peak intensity ($t = 100$ ns) for the in-and out-of-plane signals. At a pressure of 2.5 Torr, the average gas kinetic collision time is 40 ns. The data in Figure 5.7a represent the distribution of optically centrifuged CO after 2-3 gas kinetic collisions. For the CO $J = 64$ state, the in-plane signal is three times larger than the in-plane signal for $J = 80$. The $J = 64$ in-plane signal is 20-fold larger than the out-of-plane signal at that state. A comparison of the SI and SII distributions shows an increase in the relative population for states with $J > 64$ and an increase in the orientational anisotropy $r(t)$ of the centrifuged sample at all times measured. Increased orientational anisotropy is a result of fewer collisions under reduced pressure conditions.

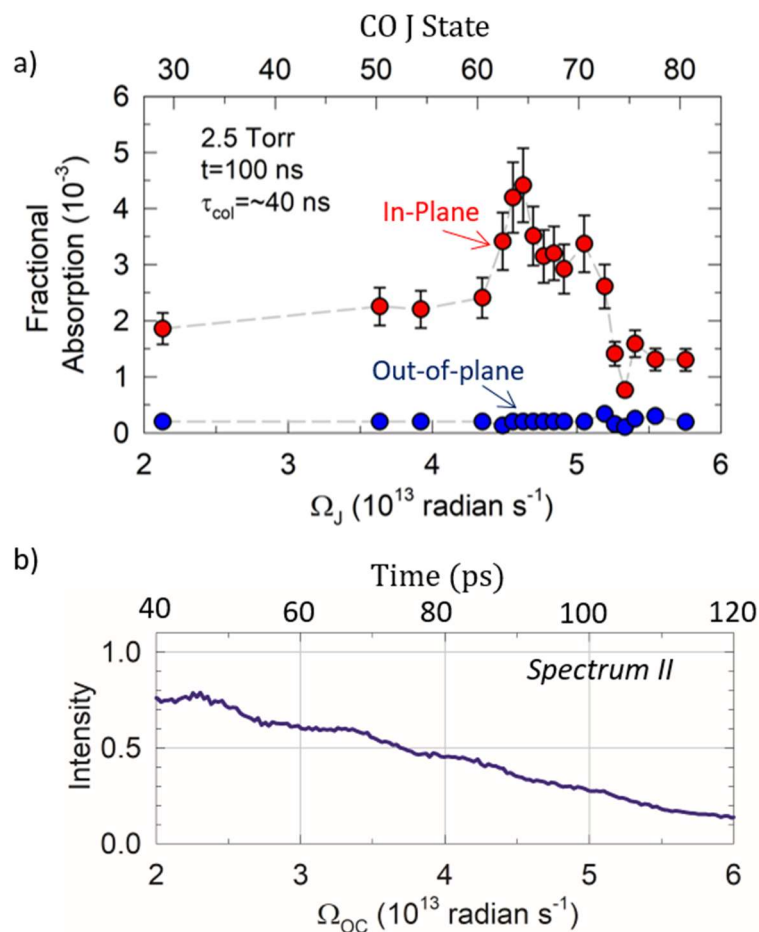


Figure 5.7 a) The distribution for measurements for in- and out-of-plane signals at a pressure of 2.5 Torr. b) Spectral intensity of SII vs angular frequency of the optical field.

Figure 5.7b shows the intensity profile of the optical centrifuge for SII as a function of the trap angular frequency. The optical field intensity for the SII decreases gradually between $4.6 - 6 \times 10^{13}$ rad s^{-1} from a relative intensity of 0.35 to 0.15. The more gradual intensity decrease for SII is responsible for the broader distribution shown in Figure 5.7a. The two distributions were collected at two different pressures, so it is not possible to make a direct intensity comparison. However, it is clear that the intensity of the optical centrifuge bandwidth and its slope affect the extent of rotational excitation and the width of the rotational distribution.

5.3.3 Collision Dynamics of Optically Centrifuged CO

Here we report on studies that investigate the collision dynamics of the optically centrifuged CO molecules using the SII bandwidth. Transient Doppler-broadened line profiles for eight high- J states of CO were measured to determine the translational energy of the optically centrifuged molecules. Figure 5.8 shows Doppler-broadened line profiles for four CO rotational states with $J = 62-75$ 100 ns after the centrifuge pulse. The profiles were measured with a pressure of 5 Torr. The IR probe polarization was parallel to plane of centrifuge rotation. Each profile was fit to a Gaussian function. The fit residuals are shown in Figure 5.8. The translational temperature for each state was determined from the FWHM of the Doppler-broadened line profile. Figure 5.9 shows duplicate measurements of the average translational temperature for CO states with $J = 62-80$ for the first 10 collisions to illustrate the reproducibility of these measurements.

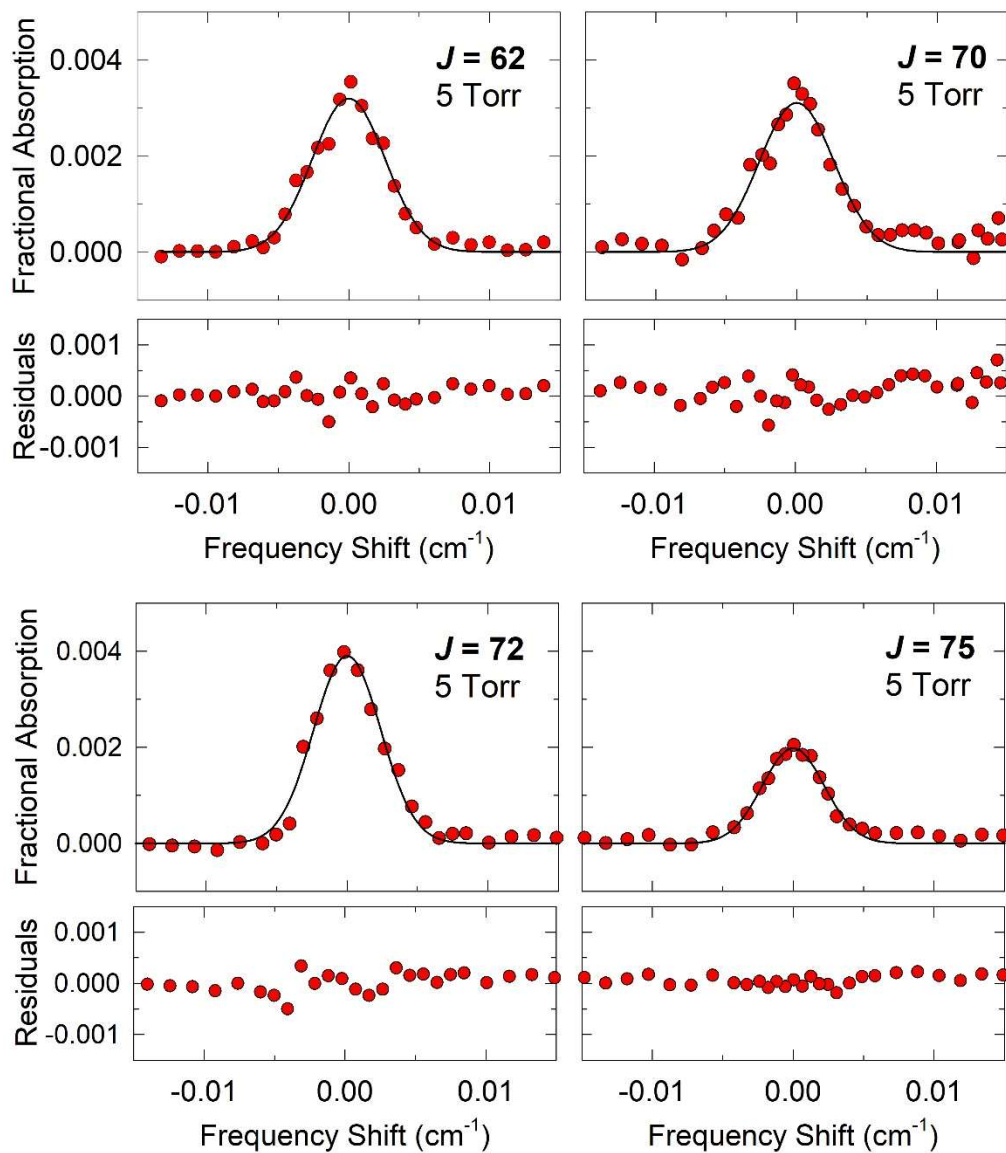


Figure 5.8 Transient Doppler-broadened line profiles for CO rotational states with $J = 62$, 70 , 72 , and 75 with a CO pressure of 5 Torr collected at $t = 100$ ns after the optical centrifuge pulse. Residuals for the Gaussian fit are shown below each profile. The IR probe polarization was parallel with the plane of centrifuge rotation.

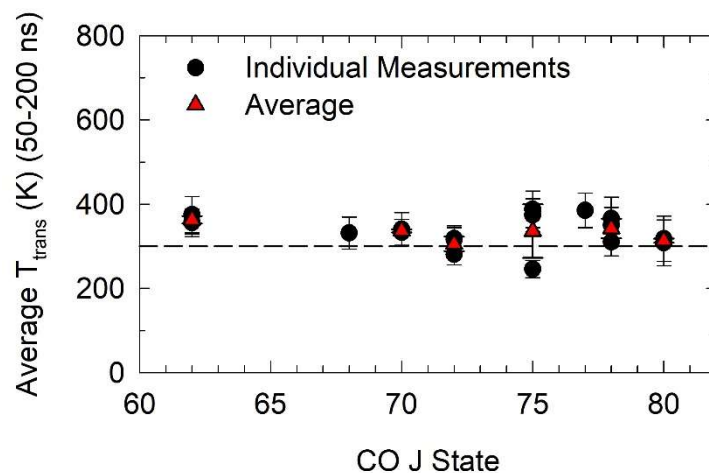


Figure 5.9 The average translational temperature over the first 10 collisions are shown. Individual measurements are shown in black circles, and the average translational temperature for each J state is shown with a red triangle. The dotted line indicates 300 K.

Figure 5.10 shows the translational temperatures for the four states in Figure 5.8 as a function of time. The translational temperatures start near 300 K and remain constant for at least 600 ns. The number of collisions is also included in Figure 5.10. Based on a gas kinetic collision time of 20 ns at 5 Torr, the translational temperatures remain constant for at least 30 collisions, indicating that little translational energy is gained through collisions of high- J CO molecules.

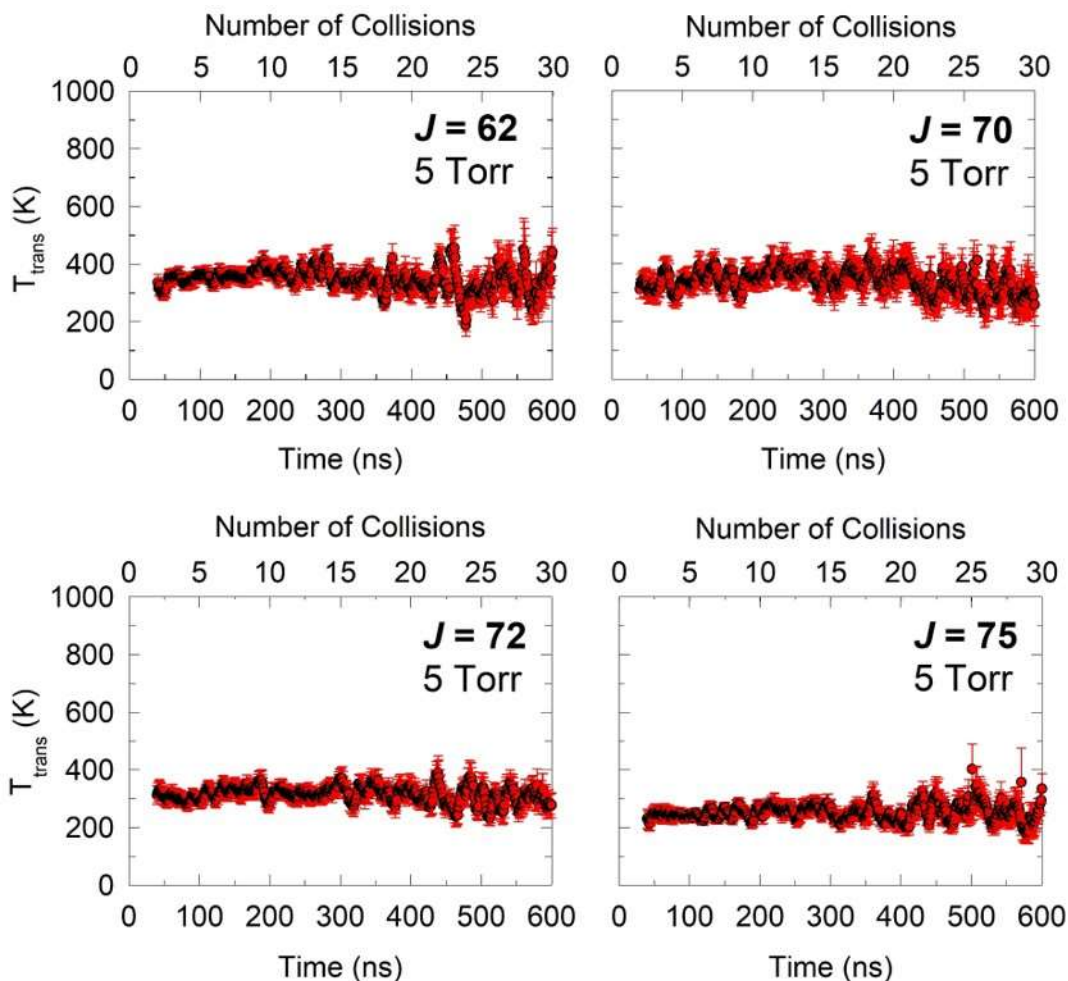


Figure 5.10 Time-evolution of translational temperatures for CO rotational states with $J = 62, 70, 72,$ and 75 at a pressure of 5 Torr and IR probe polarization parallel to the plane of centrifuge rotation. The number of collisions are included in each plot based on the average time between collisions is 20 ns at 300 K.

The low and nearly constant translational energies observed for CO states with $J = 62-75$ indicate that little rotation-to-translation energy transfer occurs through collisions of centrifuged molecules. This observation shows that near-resonant rotation-to-rotation collisional energy transfer is the dominant relaxation pathway for CO super rotors. To illustrate this phenomenon, consider energy transfer from a CO ($J = 70$) donor molecule to a CO ($J = 68$) acceptor molecule that involves $\Delta J \pm 1$. The energy down is $\Delta E_{\text{rot}} \approx 260$ and the energy up is $\Delta E_{\text{rot}} \approx 257$. This

situation leaves only 3 cm^{-1} remaining for translational energy. In contrast, collisions of high- J CO molecules with thermal CO molecules is likely to occur by non-resonant rotation-to-rotation energy transfer that results in large amounts of translational energy. As an example, collisions of a CO ($J = 70$) donor with a CO ($J = 29$) acceptor that undergo $\Delta J \pm 1$ exchange have 145 cm^{-1} available for translation. This phenomenon was reported in the previous study in the Mullin research group where the CO $J = 29$ state had a translational temperature of $T_{trans} = 900 \text{ K}$ after the centrifuge pulse and at a pressure of 10 Torr.¹³

5.3.4 Estimating Rotational Excitation of Other Molecules in the Optical Centrifuge

The results reported in this chapter provide important information about the extent of rotational excitation in an optical centrifuge. For the SII bandwidth, most of the CO population is found with $J \leq 75$, for which $\Omega_{OC} \approx 5.4 \times 10^{13} \text{ rad s}^{-1}$. Based on the CO results presented here, we estimate that the full bandwidth of the optical centrifuge is capable of driving CO_2 to rotational states with at least $J \approx 370$ and N_2O to rotational states with $J \approx 350$. This information was used to design experiments using a tunable optical centrifuge that will be described in Chapter 6.

5.4 Conclusion

The CO experiments reported here show that changes in pressure and the spectral bandwidth of the optical centrifuge influence the extent of rotational energy imparted to CO molecules in an optical centrifuge. These experiments are the first transient IR absorption measurements of the full distribution of centrifuged

molecules. Polarization-sensitive signals illustrate the highly anisotropic nature of the distribution prepared by the optical centrifuge, where the intensity of in-plane signals is much larger than the out-of-plane signals. This study also provides the first experimental evidence of resonant rotation-to-rotation energy transfer in which centrifuged molecules gain almost no translational energy through collisions. This study demonstrates the extent to which optical angular frequency is converted to molecular rotation.

Chapter 6: Nascent Distributions of CO and CO₂ made with a Tunable Optical Centrifuge: Measuring Capture and Acceleration Efficiencies

6.1 Introduction

An optical centrifuge is a strong-field, laser-based technique that uses shaped optical pulses to trap and angularly accelerate molecules into high rotational states. A number of studies have used an optical centrifuge to prepare high- J molecules to investigate their collisional energy transfer, orientational relaxation dynamics, chemical reactions, spectroscopy and decoherence. An important question for future studies of molecular super rotors is the extent to which different molecules are effectively trapped and accelerated in an optical centrifuge. Here, we address this question using high-resolution transient IR absorption spectroscopy to measure nascent rotational distributions of CO and CO₂ that are prepared in a tunable optical centrifuge.

Transient absorption spectroscopy is a state- and time-resolved probe that can yield absolute number densities of centrifuged molecules before collisions redistribute the rotational energy. A tunable optical centrifuge enables control over the nascent distribution by varying the spectral bandwidth of the shaped pulses.^{7, 16} By combining these approaches, we measure the capture and acceleration efficiencies of CO and CO₂ made in optical traps with variable bandwidth.

The interaction responsible for trapping molecules is a field-induced dipole $|E|^2 \Delta\alpha$. The interaction energy is $U(\theta) = -U_0 \cos(\theta) = -\frac{1}{4} \Delta\alpha |E|^2 \cos(\theta)$ where θ

is the angle between the optical field vector and the molecular axis with the largest polarizability. The polarizability anisotropy values for CO₂ and CO are $\Delta\alpha = 2.05 \text{ \AA}^3$ and 0.53 \AA^3 , respectively.

The requirements for effective capture in an optical centrifuge have been discussed previously.^{7, 33} When Karczmarek et al. first proposed the optical centrifuge, they identified the time criteria for effective optical trapping with a turn-on time that is bracketed by two criteria.⁷ The turn-on time must be long enough for the nuclei to respond, but not so long that the rotational energy surpasses the trap energy U_0 . For a linear optical chirp, the angular frequency Ω of the trap depends linearly on the chirp rate β such that $\Omega(t) = \beta t$. For efficient trapping, the turn-on time is bracketed by $\sqrt{2\pi/\beta} < t_{on} < \sqrt{U_0/I\beta^2}$, where I is the moment of inertia. The inequality can be rewritten as $(\Delta\alpha/I) > (8\pi\beta/E^2)$, with the molecular parameters for effective trapping on the left hand side. The ratio of $\Delta\alpha/I$ is 30% larger for CO than for CO₂.

Armon and Friedland have theoretically investigated capture probabilities in an optical centrifuge.^{33, 34} They identify a quantum regime in which rotational excitation is achieved by sequential ladder climbing through stimulated Raman excitation that involves single pairs of states with the same symmetry. They also identify a classical regime in which molecules are rotationally excited through an autoresonance that involves sustained phase locking with the chirped drive. The autoresonance mechanism involves the simultaneous excitation of multiple pairs of states. They characterize capture efficiencies based on representative time scales for the drive sweep, the Rabi drive and molecular rotation. Based on its relatively small

moment of inertia, CO is in the quantum regime but its capture is fairly inefficient because its interaction energy with the field is relatively weak. CO₂ is in the classical excitation regime and is predicted to be more efficiently centrifuged than CO based on CO₂'s larger interaction energy.

The shaped pulses that comprise the optical centrifuge are based on overlapping, in time and space, a pair of oppositely-chirped laser pulses $\omega_1(t)$ and $\omega_2(t)$, each with opposite circular polarization and the same initial optical frequency ω_0 . The net result is a linear optical field that angularly accelerates during the pulse. The instantaneous angular frequency $\Omega_{oc}(t)$ of the optical trap results from the time-dependent frequency difference of the two chirped pulses such that $\Omega_{oc}(t) = \Delta\omega = \frac{1}{2}(\omega_1(t) - \omega_2(t))$. Here, $\omega_1(t)$ is the frequency of the positively-chirped pulse and $\omega_2(t)$ is the frequency of the negatively-chirped pulse. Molecules that are trapped in the field are angularly accelerated to a rotational angular frequency Ω_J , such that $\Omega_J = \Omega_{oc}$. A tunable optical centrifuge is obtained by reducing $\Delta\omega$.^{7, 16} This reduction is achieved by blocking the highest frequencies of the positively-chirped pulse in a controlled way. This technique reduces the maximum value of Ω_J that a trap can effect, thereby enabling control over the nascent rotational distributions.

Prior to the work reported here, nascent rotational distributions of optically centrifuged molecules had not been observed directly with transient IR absorption spectroscopy. The full-width half-maximum (FWHM) spectral bandwidth of our optical centrifuge corresponds to $\Omega_J(\text{FWHM}) = 3.5 \times 10^{13} \text{ rad s}^{-1}$ and rotational excitation in CO to $J \approx 49$ and CO₂ to $J \approx 236$. For this study, we introduced three sequential reductions (or “clips”) in the bandwidth of the optical trap so that its

angular frequency could be varied over $\Omega_J(\text{FWHM}) = (2.8 - 3.5) \times 10^{13} \text{ rad s}^{-1}$. We identified five rotational states each of CO and CO₂ with rotational angular frequencies that correspond to the range of trap frequencies in the tunable optical centrifuge and measured how the nascent CO and CO₂ distributions respond to changes in the effective upper limit of the trap frequency. These states are listed in Table 6.1, along with their energies and classical rotational frequencies. Fundamental IR probe transitions for CO have been reported for states up to $J = 93$.³² For CO₂, observed ν_3 IR transitions have been reported up to $J = 128$; semi-empirical transition frequencies have been reported for CO₂ up to $J = 300$ in the 4000 K Carbon Dioxide Spectral Database (CDSD4000).^{20, 29} Here we identify and report experimental values of IR transition frequencies for five CO₂ states with $200 \leq J \leq 240$.

Table 6.1: Rotational energies and Ω_J values for selected J -states of CO and CO₂

CO J	$E_J \text{ (cm}^{-1}\text{)}^a$	$\Omega_J \text{ (10}^{13}\text{rad s}^{-1}\text{)}$	CO ₂ J	$E_J \text{ (cm}^{-1}\text{)}^b$	$\Omega_J \text{ (10}^{13}\text{rad s}^{-1}\text{)}$
41	3,292	2.99	200	15,472	2.93
43	3,616	3.14	212	17,350	3.10
46	4,128	3.35	228	20,012	3.33
48	4,488	3.49	234	21,057	3.41
49	4,674	3.57	240	22,127	3.50

a. Energies for CO states are from HITRAN database.²⁰

b. Energies for CO₂ are from semi-empirical calculations CDSD4000.²⁹

6.2 Experimental Details

The optical-centrifuge high-resolution transient IR absorption spectrometer has been described in detail previously.¹⁵ The key elements are an amplified ultrafast

Ti:sapphire laser system with a chirped pulse shaper and secondary amplification, a single-frequency quantum cascade laser (QCL) for transient IR probing, and a multi-pass detection cell. The optical centrifuge chirped pulse shaper has been modified to add a tunable beam block to control the spectral bandwidth of the positively-chirped pulse.

6.2.1 Controlling the Angular Frequency of the Optical Centrifuge

The key to measuring nascent distributions of the centrifuged molecules is the ability to change the spectral bandwidth of the optical centrifuge pulse reproducibly. To achieve this goal, an adjustable beam block with micrometer control was added to the chirped pulse shaper shown in Section 2.1.3. The beam block removes the high frequency components of the positively-chirped beam. The spectrum of the pulses are shown in Figure 6.1a. Figure 6.1b shows how the bandwidth of the optical trap is reduced by clipping the blue wing of the positively-chirped pulse. The full bandwidth is referred to as Clip 0, and the three reduced bandwidth spectra are Clips 1-3. Figure 6.1c shows the angular frequency $\Omega_{oc}(\text{FWHM})$ of each clip based on the FWHM spectra. The CO and CO₂ states listed in Table 6.1 were chosen to overlap with the range of angular frequencies in Figure 6.1c. For the experiments reported here, the pulse energy of the multi-pass amplifier pump laser was reduced by 30% relative to energies used in previous measurements to avoid damaging the multi-pass amplifier when the input pulses had reduced bandwidth.

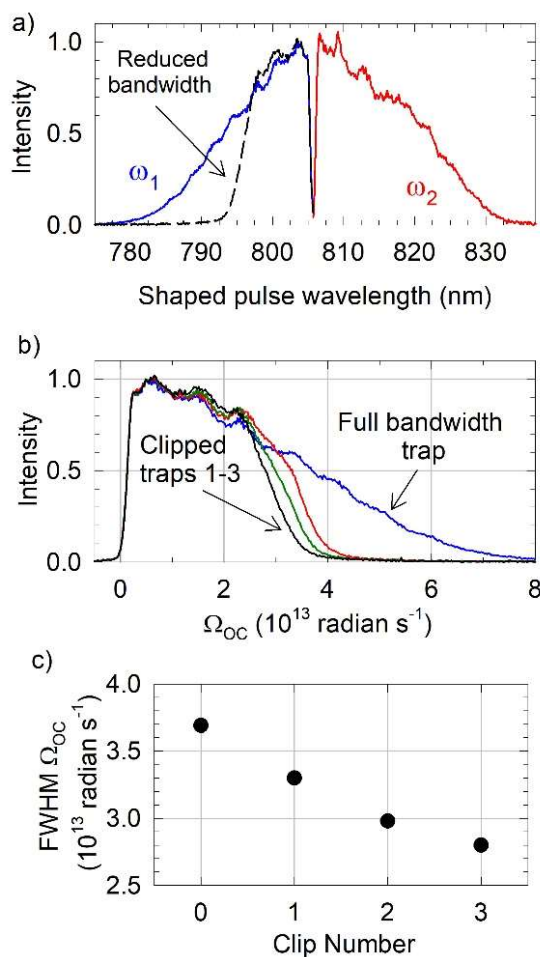


Figure 6.1 a) Spectra of optical centrifuge pulses. Bandwidth reduction of the positively-chirped pulse ω_1 reduces the rotational excitation in the trap. b) Optical trap intensity as a function of angular acceleration. c) Angular frequency of the optical trap at full-width half-maximum (FWHM) as a function of clipping the positively-chirped pulse. Clip 0 corresponds to the full bandwidth trap; Clips 1-3 have sequentially smaller ultimate angular frequencies.

6.2.2 High-Resolution Transient IR Spectroscopy of Centrifuged CO and CO₂

A continuous-wave single-frequency quantum cascade laser is used for transient IR detection of centrifuged CO and CO₂. The quantum cascade laser has tunable IR output near $\lambda = 4.3 \mu\text{m}$ and a spectral resolution of $\Delta\nu_{IR} < 0.0002 \text{ cm}^{-1}$. The 11-pass IR beam path has a range of overlap path lengths of $\ell = 0.052 - 0.12 \text{ cm}$, based

on the centrifuge beam diameter that is used to determine the overlap. The smaller path length results when the full cross section of the pulse beam is used. When the diameter is based on 50% of the Gaussian cross section, the smaller path length is obtained.¹⁴ Number densities for centrifuged molecules reported here are based on an absorption pathlength of $\ell = 0.12$ cm and represent lower limits. The IR laser is wavelength-stabilized with active feedback control by locking either to the peak of known IR transitions using a reference gas cell or to a fringe of a tunable Fabry-Perot etalon. The IR wavelength is determined using known IR transitions of thermally populated states and a calibrated wavemeter to a resolution better than $\Delta\nu_w = \pm 0.001$ cm⁻¹. The transmitted IR intensity is collected as a function of time on an InSb detector with a 10-90 rise time of ~ 50 ns. Transient signals are averaged on a 500 MHz digital oscilloscope (Tektronix) for approximately 100 laser pulses. The IR polarization is vertical (parallel) to coincide with the plane of molecular rotation in the optical centrifuge. Spectroscopic grade CO and CO₂ were used. Transition measurements for CO₂ used a cell pressure of 2.5 Torr. Nascent distributions were measured with a cell pressure of 500 mTorr at $t = 100$ ns following the optical centrifuge pulse. At 500 mTorr, the gas kinetic collision time is approximately 200 ns.

Nascent distributions of CO ($v=0, J$) and CO₂ ($00^0_0, J$) were probed using IR fundamental transitions near $\lambda=4.3$ μm , shown schematically in Figure 6.2. The IR probe transitions for CO₂ involves absorption of the ν_3 antisymmetric stretching mode. To find the probe transitions for CO₂ (00^0_0) states with $J \geq 200$, we used transient absorption fingerprinting to identify a number of *R*-branch transitions.

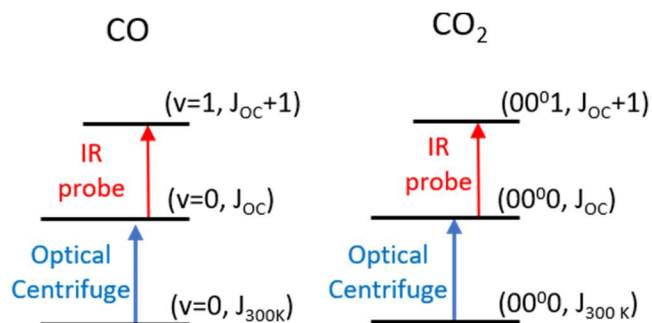


Figure 6.2 Schematic energy levels and *R*-branch transitions for transient IR probing of optically centrifuged CO and CO₂. The optical centrifuge excites molecules to a set of centrifuged rotational states with J_{OC} . The transient IR probe measures state-specific number densities for the nascent distribution of centrifuged molecules.

6.3 Results and Discussion

Here we report capture and acceleration efficiencies in an optical centrifuge based on measurements of nascent rotational distributions of centrifuged CO and CO₂ using high-resolution transient IR absorption spectroscopy. We focus on the set of rotational states listed in Table 1 that have rotational frequencies that coincide with the FWHM angular frequencies of a tunable optical centrifuge.

First, we describe the transient spectroscopy of CO₂ fundamental ν_3 R-branch transitions for $J \geq 200$, followed by two experiments to measure the total number density of rotationally excited molecules. The first experiment uses the full spectral bandwidth to measure a number density of molecules with Ω_J values that are significantly below Ω_{OC} . In the second experiment, the nascent CO and CO₂ distributions are measured for reduced-bandwidth optical traps. Combining these two measurements yields the number density of molecules captured and accelerated by the optical field and as a function of Ω_{OC} , from which the capture and acceleration efficiencies of CO and CO₂ are compared.

6.3.1 Transient IR Probe Transitions of CO ($\nu=0, J = 41-49$) and CO₂ ($00^0_0, J = 200-240$)

IR frequencies for CO₂ ($00^0_1 \leftarrow 00^0_0$) *R*-branch transitions with $J = 200 - 240$ were determined using spectral fingerprinting and a high-resolution calibrated wavemeter as described in Chapter 4. Transient IR absorption signals were collected as a function of IR wavelength in frequency steps of $\delta\nu \leq 0.001 \text{ cm}^{-1}$ between neighboring IR transitions. When possible, the transitions were measured relative to known IR transitions.

Table 6.2 lists the IR probe frequencies for CO and CO₂ used in this study and compares the CO₂ probe transition frequencies with predicted frequencies from CDSD4000. The observed (00^0_0) *R*-branch transition frequencies for $J \leq 240$ are very close to values predicted from effective Hamiltonian calculations using CO₂ polyads and $J \leq 300$. (CDSD4000).²⁹

Table 6.2 IR probe transition frequencies for CO and CO₂ used in this study.

CO <i>J</i> state	$\nu \text{ (cm}^{-1}\text{)}$ ^a	CO ₂ <i>J</i> state	$\nu \text{ (cm}^{-1}\text{)}$ ^b observed	$\nu \text{ (cm}^{-1}\text{)}$ ^c (CDSD4000)	$\Delta\nu \text{ (cm}^{-1}\text{)}$ obs-calc
41	2271.345	200	2377.441	2377.432	0.009
43	2275.719	212	2370.885	2370.870	0.015
46	2281.970	228	2360.743	2360.717	0.026
48	2285.928	234	2356.552	2356.522	0.030
49	2287.843	240	2352.186	2352.151	0.035

a. HITRAN database.²⁰

b. The uncertainty in the observed CO₂ transition frequencies is $\Delta\nu = \pm 0.003 \text{ cm}^{-1}$.

c. Predicted transition frequencies from the CDSD4000.²⁹

6.3.2 Rotational Excitation Using the Full Bandwidth of the Optical Centrifuge

Two types of measurements were performed with the full bandwidth optical centrifuge (Clip 0). First, the distribution of CO ($J = 29 - 68$) was characterized using the full bandwidth centrifuge to identify the most populated states. Figure 6.3a shows the intensity of the unclipped optical trap as a function of angular frequency. Figure 6.3b shows the CO population distribution at $t = 100$ ns after the optical centrifuge pulse and a pressure of 2.5 Torr. The CO distribution peaks at $J = 64$ ($E_{rot} \approx 7,900 \text{ cm}^{-1}$), which has a rotational angular frequency $\Omega_J = 4.6 \times 10^{13} \text{ rad s}^{-1}$. Population is seen in the $J = 68$ state, showing that the optical trap has sufficient intensity to angularly accelerate CO molecules to $\Omega_{OC} = 4.8 \times 10^{13} \text{ rad s}^{-1}$. The population decreases for states with $J > 64$ as the trap intensity tails off at higher angular frequencies. The CO distribution in Figure 6.3b also has some component of collisional energy transfer that reduces the peak intensity and increases the intensities at lower rotational frequencies.

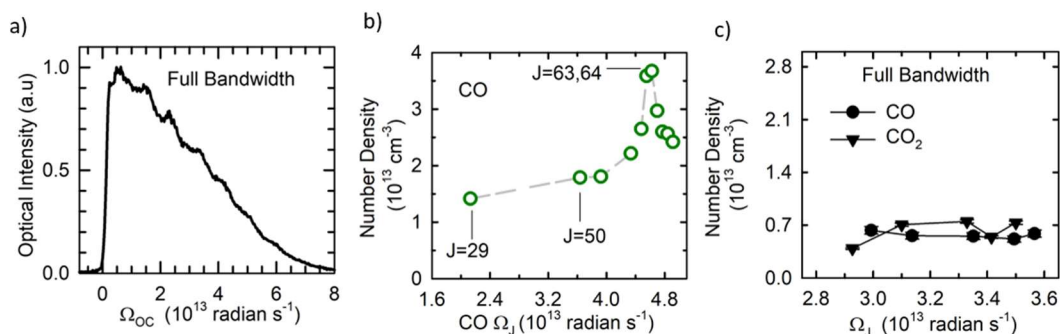


Figure 6.3 a) The full bandwidth optical trap intensity as a function of angular frequency. b) The population distribution of CO with $J = 29 - 68$ made using the full bandwidth trap and a pressure of 2.5 Torr. c) Number densities of CO ($J = 41 - 49$) and CO_2 ($J = 200 - 240$) made with the full bandwidth centrifuge at 500 mTorr.

The second measurement used the full-bandwidth optical centrifuge to determine the nascent distributions of CO ($J = 41 - 49$) and CO_2 ($J = 200 - 240$).

These states have rotational angular frequencies $\Omega_J = 2.9 \times 10^{13} - 3.6 \times 10^{13} \text{ rad s}^{-1}$, all of which are below the trap frequency of the CO peak population, $\Omega_{OC} = 4.5 \times 10^{13} \text{ rad s}^{-1}$. The pressure was reduced to 500 mTorr and nascent populations were measured at 100 ns. Figure 6.3c shows that population observed in these states is J -independent and that CO and CO₂ have similar number densities on a per state basis. The average number densities are $5.7 \times 10^{12} \text{ cm}^{-3}$ per state for CO and $6.2 \times 10^{12} \text{ cm}^{-3}$ per state for CO₂. Transient signals for these states are prompt, showing that the states are populated directly in the optical centrifuge pulse. Two mechanisms can lead to nascent population in the lower- J states. Molecules will fall out of the optical trap when the cross-sectional intensity drops in the Gaussian wings. In addition, a small fraction of rotationally excited molecules are formed through sequential Raman transitions by the chirped pulses without angular acceleration from the optical field.

6.3.3 Nascent Distributions of CO and CO₂ from a Tunable Optical Centrifuge

Nascent rotational distributions were measured for CO ($J = 41 - 49$) and CO₂ ($J = 200 - 240$) using a tunable optical centrifuge for which Ω_{OC} was reduced to coincide with Ω_J for this set of states. Four optical bandwidths were used: the full bandwidth (Clip 0) and three reduced-bandwidth traps denoted Clips 1-3. Figure 6.4a shows the angular profiles for the four traps. As the optical bandwidth is decreased, the trap intensity at large Ω_{OC} values decreases, leading to less rotational energy in the trapped molecules. First, we illustrate the effect of reducing the centrifuge angular frequency by measuring the peak of the CO distribution as a function of the clip.

Figure 6.5b shows that the CO $J = 62$ state is populated in the unclipped centrifuge, and that no population is observed when the bandwidth is reduced in Clips 1-3. Comparing the relative intensity of the optical trap at the rotational angular frequency for CO $J = 62$ ($\Omega_J = 4.48 \times 10^{13}$ rad s $^{-1}$) shows that the clipped traps do not have sufficient intensity at the higher frequencies to ramp molecules into the $J = 62$ state.

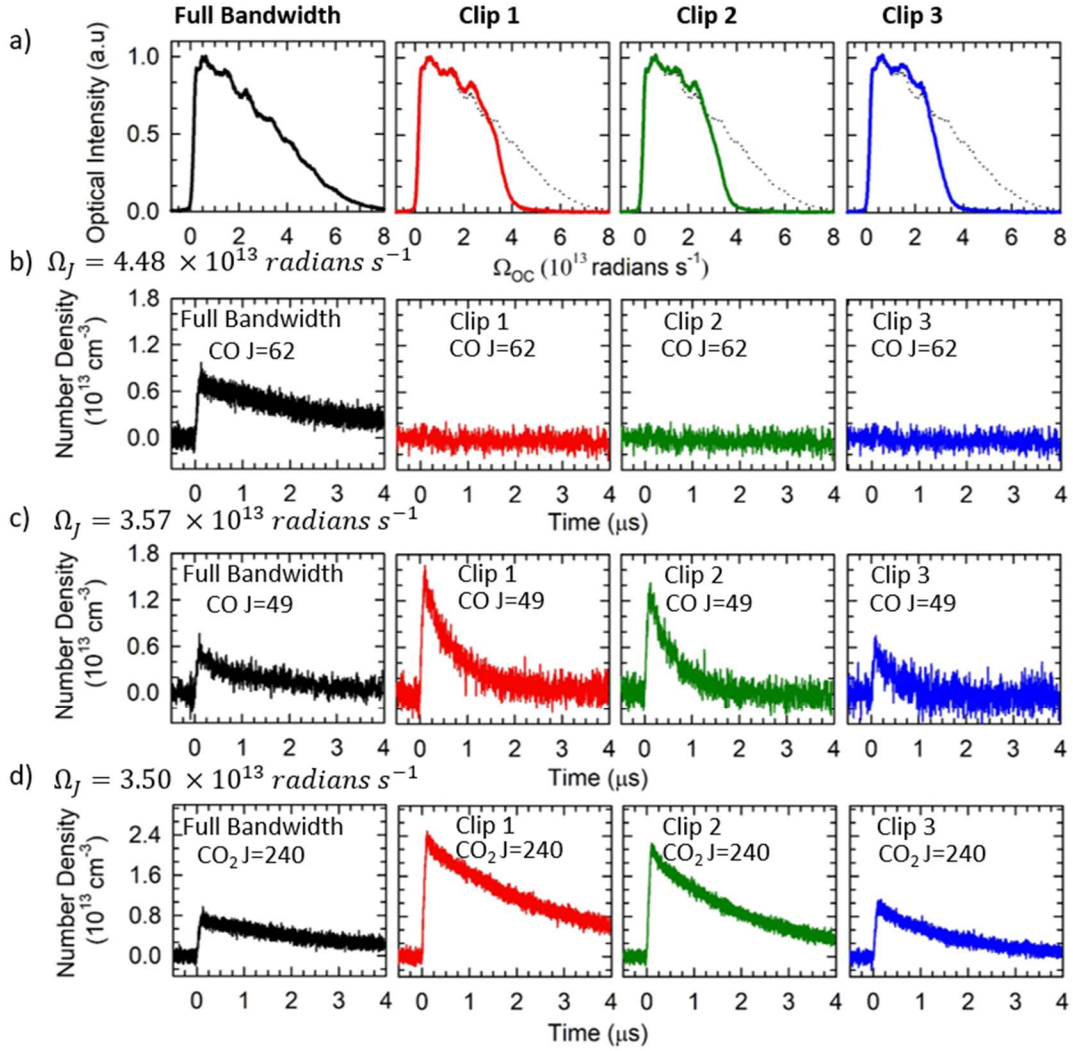


Figure 6.4 a) Full bandwidth spectrum (left-most), and three reduced bandwidth decreasing from left to right. Measurement of number densities for b) CO ($J = 62$), c) CO ($J = 49$), d) CO₂ ($J = 240$) at the four bandwidths.

Figure 6.4c shows the progression of population in CO $J = 49$ ($\Omega_J = 3.57 \times 10^{13}$ rad s^{-1}) as the bandwidth is sequentially decreased. The population increases nearly 3-fold when the full bandwidth is reduced to Clip 1. Further bandwidth reduction of Clips 2 and 3 leads to reduced population in CO $J = 49$. Figure 6.4d shows that the progression of the initial population in CO₂ $J = 240$ ($\Omega_J = 3.50 \times 10^{13}$ rad s^{-1}) is nearly identical to that for CO $J = 49$. These data

show that by reducing the trap bandwidth, it is possible to tune through the peak of the nascent rotational distribution.

Figures 6.5a-c show the nascent rotational distributions for CO ($J = 41 - 49$) and CO₂ ($J = 200 - 240$) made with sequentially-reduced bandwidths (Clips 1-3). The smallest bandwidth reduction (Clip 1) results in inverted rotational distributions for both CO and CO₂. Clip 2 shifts both distributions to lower J states. Further reduction of the bandwidth to Clip 3 results in rotational distributions shown in Figure 6.5c that are no longer inverted. The intensity of the optical trap at $\Omega_{OC} = 3.5 \times 10^{13} \text{ rad s}^{-1}$ is sufficiently reduced in Clip 3 to reduce the number densities in the higher J states. Figures 6.5d-f show the population of centrifuged molecules for each clip relative to the Clip 0 populations (Figure 6.3c). Clips 1-3 lead to population enhancements of as much as a factor of three and in the case of Clip 3, the lowest CO₂ state has an enhancement by nearly a factor of 5. These data quantify the extent to which rotational distributions are controlled in a tunable optical centrifuge.

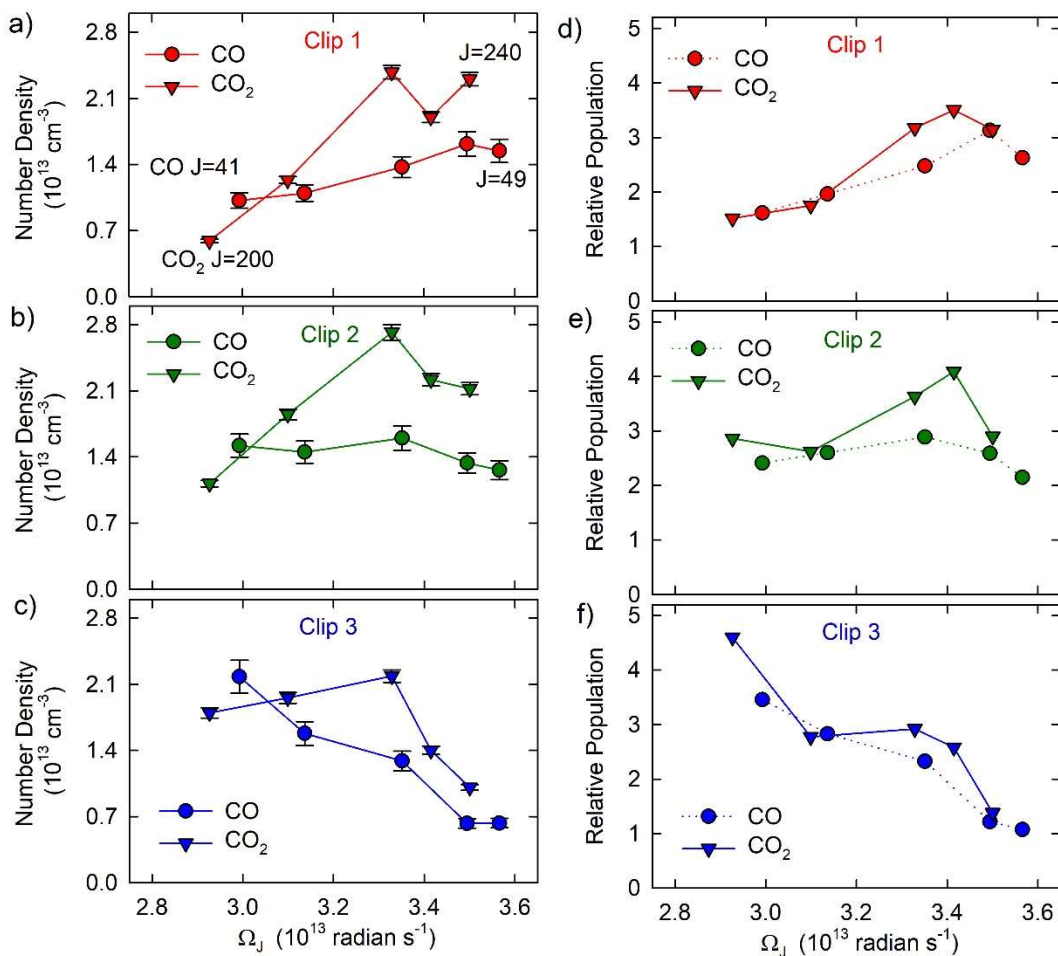


Figure 6.5 a-c) Nascent distributions of CO and CO₂ rotational states as a function of reducing the optical centrifuge spectral bandwidth. The lines are included as guides to identify the molecule. d-f) The populations measured with Clips 1-3 relative to populations made with the full bandwidth (Clip 0) centrifuge shown in Figure 6.3c.

The CO and CO₂ distributions have remarkably similar responses to clipping the optical centrifuge bandwidth. The extent of rotational excitation is sensitive to the angular frequency of the optical trap and its corresponding intensity at that frequency. In this range of rotational energies, CO and CO₂ are excited to similar angular frequencies, despite differences in their moments of inertia, rotational energies and anisotropic polarizabilities. At higher angular frequencies, the rotational energy will

influence the molecular potential energy in such a way as to result in differences in trapping behavior for CO and CO₂.

Capture and Acceleration Efficiencies

The nascent rotational distributions are used to determine the capture and acceleration efficiencies of CO and CO₂ in an optical centrifuge. The J -specific data from each clipped optical trap yield an integrated number density of centrifuged molecules by summing the nascent distributions. Figure 6.3c shows that the CO $J = 41 - 49$ and CO₂ $J = 200 - 240$ states made in the full bandwidth optical centrifuge have relatively small J -independent number densities. In this situation, the ultimate trap frequency Ω_{OC} is much greater than the rotational frequency so the bulk of the population is driven into higher J states. We estimate that $N = 5.7 \times 10^{12} \text{ cm}^{-3}$ per state for CO with $J < 41$ and that $N = 6.2 \times 10^{12} \text{ cm}^{-3}$ per state for CO₂ with $J < 200$. For the clipped bandwidth experiments, the data in Figure 6.5a-c were used directly and number densities were interpolated for missing states. The summed number densities include 49 CO states and 120 CO₂ states.

The total number densities from the three reduced-bandwidth measurements are shown in Figure 6.6a as a function of clip number, based on the upper limit to the IR path length of $\ell = 0.12 \text{ cm}$. The total number densities are independent of the bandwidth reduction, showing that the bandwidth changes moved population within the nascent distribution but are not so great as to tune the centrifuged molecules out of the IR probe window. The lower limit to the average total number densities of centrifuged molecules are $N_{OC}(CO) = 3.6 \times 10^{14} \text{ cm}^{-3}$ for CO and $N_{OC}(CO_2) =$

$10.1 \times 10^{14} \text{ cm}^{-3}$ for CO_2 . Using the lower limit of the IR path length ($\ell = 0.052 \text{ cm}$) yields number densities that are twice as large. The ratio of the number densities, shown in Figure 6.6b, shows that the capture efficiency of centrifuged CO_2 is 3-times larger than for CO. Based on the fractional excitation from a 500 mTorr sample, we determine capture and acceleration efficiencies of $P(\text{CO}_2) = 6 - 12\%$ for CO_2 and $P(\text{CO}) = 2 - 4\%$ for CO, where the factor of two spread comes from uncertainty in the IR path length. The ratio of CO_2 and CO number densities is not affected by path length uncertainty since the path length is the same for both measurements. The measured value of $P(\text{CO}_2)$ compares favorably to the classical non-linear dynamics calculations by Armon and Friedland.³⁴ Assuming a constant intensity optical trap and starting with a 300 K sample, they predict that $P(\text{CO}_2) = 14\%$. The calculated probability is expected to be higher than the measured value because of the non-uniform cross section of the trap intensity.

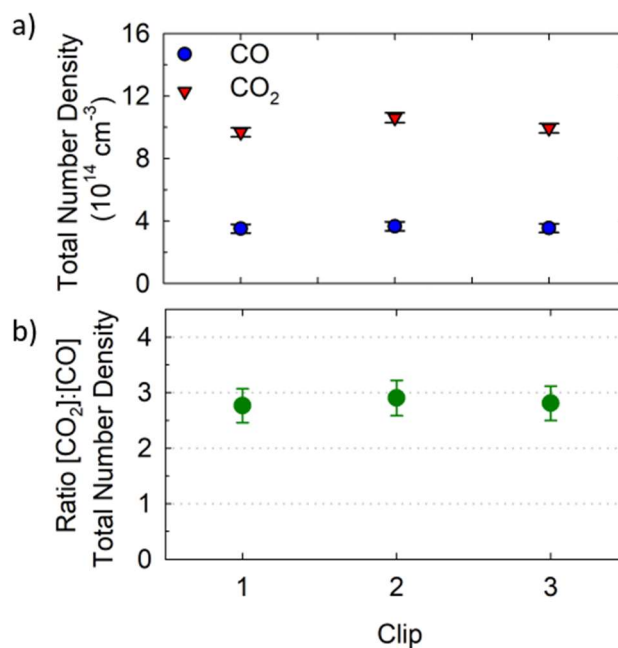


Figure 6.6 a) Total number densities of trapped molecules for CO and CO₂ from integrated nascent distribution measurements. b) The ratio of [CO₂] to [CO] shows that CO₂ has a capture and acceleration probability in the optical centrifuge that is nearly three times larger than that for CO.

The results presented here give us an opportunity to consider the features responsible for retention of molecules in the optical centrifuge trap. By reducing the centrifuge bandwidth, we reduce the field intensity at higher angular frequencies to the point that molecules are released from the trap. Similarly, the cross section of the centrifuge beam intensity has a Gaussian profile where the optical field intensity drops radially around the outer beam circumference. The lower field strength at the beam edges is responsible for the J -independent populations of molecules that drop out of the trap while the centrifuge spins the majority of trapped molecules into higher- J states.

Our results show that more CO₂ than CO drops out of the reduced-bandwidth traps, indicating that more CO₂ was initially captured and accelerated by the optical

centrifuge. Part of the greater trapping efficiency for CO₂ lies in its larger $\Delta\alpha$ value and correspondingly larger interaction energy with the trap. However, starting with a 300 K sample also introduces differences in the trapping efficiency that favors CO over CO₂. Simulations show that at 300 K, the highest trapping probabilities involve molecules that are poised to be trapped in the optical field.⁷ This group of molecules has angular momentum projection quantum numbers M_J that are equal to the quantum number J . At 300 K, the most populated CO state is $J_{pop} = 7$ and 7% of molecules in this state has $M_J = J$. For CO₂, the most populated state is $J_{pop} = 16$ and only 3% of this state has $M_J = J$. One count of the molecules poised for efficient trapping is the sum of population with $J = 0 - J_{pop}$ and $J = M_J$. This count is 6.2% for CO and 2.9% for CO₂. In addition, trapped molecules with $M_J < J$ are held in effectively weaker traps because of non-ideal overlap of the molecular polarizability and the optical field. Initial differences in M_J and J will persist throughout the angular acceleration based on $\Delta J = \Delta M_J = 2$ selection rules for ladder climbing. As J increases in the optical trap, M_J approaches J as the interaction energy increases. Trapped molecules with larger moments of inertia are more likely to have larger gaps between J and M_J , but the fractional gap will be smaller since higher J values are achieved for these molecules in the optical centrifuge. Future studies will investigate these ideas further using other candidate molecules in an optical centrifuge.

6.3.4 Intensity-Dependent Nascent Populations

The reduced-bandwidth population data are used here to illustrate how reducing the optical field strength affects the capacity of the optical centrifuge trap to retain molecules. Figure 6.7a shows the average instantaneous laser power (in mJ per ps) of the chirped pulses as a function of angular frequency for the four optical traps used in this study. The instantaneous laser power was determined based on a measured chirp rate of $\beta = 0.5 \times 10^{12} \text{ rad s}^{-1}\text{ps}^{-1}$. The nascent J -specific populations for CO₂ and CO are shown in Figures 6.7b and c, respectively. The similarity of the two data sets is striking. The maximum population is released from the trap at a similar optical intensity for both CO₂ and CO and for all J -states that show a maximum. The state-specific number densities are approximately 25% larger for CO₂ than CO, reflecting the higher capture efficiency of CO₂. This result, along with the higher state density for CO₂, accounts for the observed factor of 3 in overall capture efficiency for CO₂ relative to CO. These results lay the groundwork for future studies on quantifying trapping efficiencies in optical centrifuge traps.

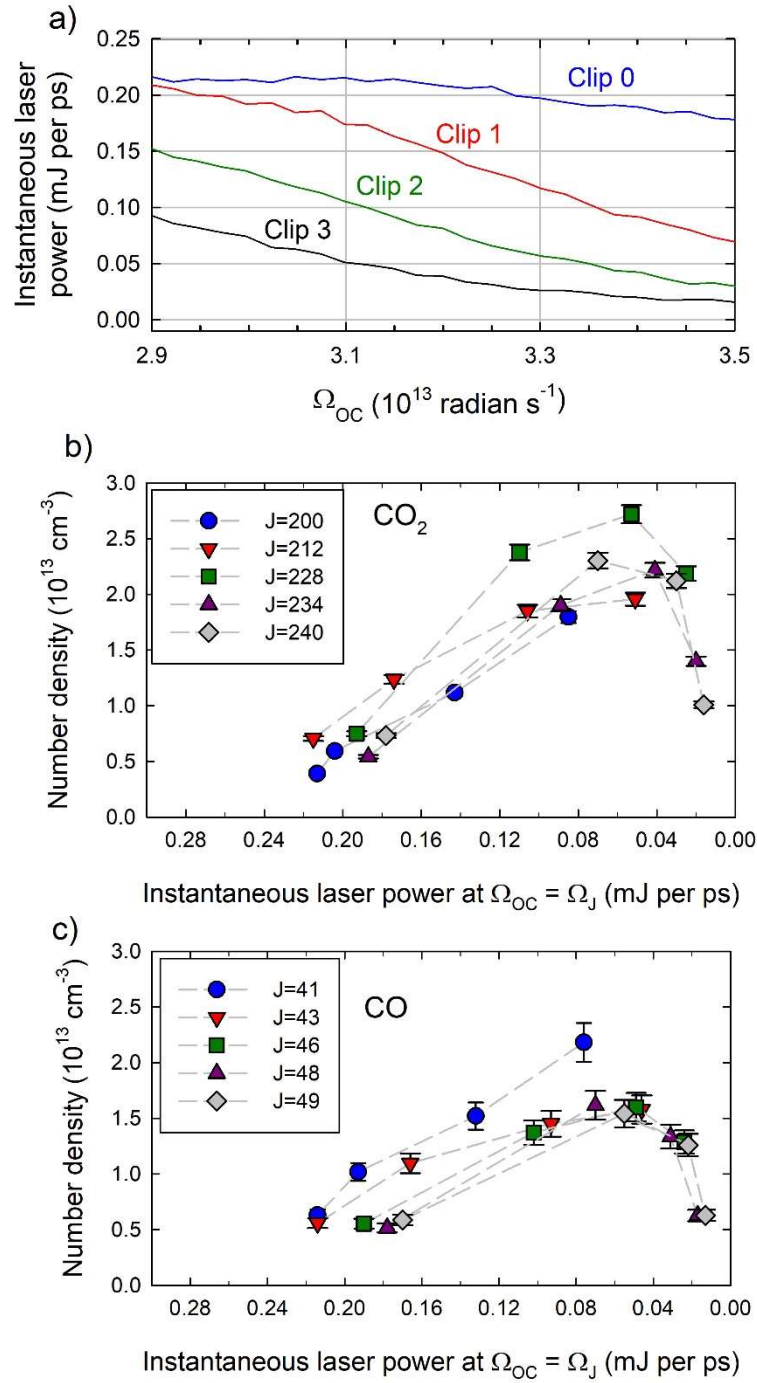


Figure 6.7 a) Instantaneous laser power of sequentially clipped pulses as a function of optical centrifuge angular frequency. Nascent J -specific populations at 100 ns of b) CO_2 and c) CO that are released from the optical trap as a function of instantaneous laser power.

6.4 Conclusion

Using a tunable optical centrifuge, we have characterized the nascent rotational distributions of CO ($J = 41 - 49$) and CO₂ ($J = 200 - 240$) using high-resolution transient IR absorption spectroscopy. These sets of states respond to controlled intensity reductions in the ultimate angular frequencies of the optical trap. When the field intensity has been reduced sufficiently, the centrifuged molecules are released from the trap and detected by transient IR spectroscopy. The J -specific response to reducing the trap intensity was similar for CO and CO₂, showing that both molecules mimic the intensity dependence of the angular trap.

A comparison of the nascent distributions reveals that three times more CO₂ than CO is optically centrifuged. More efficient optical trapping of CO₂ is consistent with its larger polarizability but this property alone does not account for the observed factor of three in trapping probability. Other influences include differences in the range of initial J states that are trapped and whether the rotational excitation occurs in a quantum regime through ladder climbing or a classical regime where the molecules are in autoresonance with the angularly accelerating trap. In future studies, it would be interesting to investigate how differences in J and M_J impact trapping probabilities and how trapping efficiency scales with $\Delta\alpha$ for other molecular species.

The experiments presented here demonstrate that nascent distributions of centrifuged molecules can be controlled and characterized quantitatively using high-resolution transient IR absorption spectroscopy. Identification of new IR transitions for CO₂ with $J \leq 240$ and $E_{rot} \leq 22,000 \text{ cm}^{-1}$ lays the groundwork for new dynamics studies of molecules with large amounts of oriented angular momentum

and provides important tests of semi-empirical calculations on high energy rotational states.

Chapter 7: The Effect of CO Rotation from Shaped Pulse Polarization on Reactions that form C₂

Adapted from: H. M. Ogden, T. J. Michael, M. J. Murray, Q. Liu, C. Toro, and A. S. Mullin, The Effect of CO Rotation from Shaped Pulse Polarization on Reactions that form C₂. *Phys. Chem. Chem. Phys.*, **21**, 14103-14110 (2019).

Power- and pressure-dependent emission was collected by Q. Liu, C. Toro, and A. S. Mullin. H. M. Ogden, T. J. Michael, M. J. Murray, and A. S. Mullin analyzed emission data, developed mechanism and kinetic model, performed transient IR absorption measurements, and prepared the manuscript.

7.1 Introduction

Optical fields have been used to influence chemical reactions by aligning and orienting molecules^{2, 4, 35-40} and by preparing reactants with specific amounts of vibrational or electronic energy.⁴¹⁻⁴⁶ In the past several decades, a number of approaches have been used to prepare molecules with both low^{1, 3, 47, 48} and high^{7, 9-16, 49} rotational energies, but the role of rotational energy in bimolecular reactions has not been widely explored. Most such studies to date have focused on low rotational energies.⁵⁰⁻⁶⁰ In some cases, rotational energy enhances reactive cross sections, whereas in other cases the cross sections are reduced by rotational energy. Many factors appear to contribute including thermochemistry, steric effects, anisotropic potential energy surfaces, centrifugal barriers in entrance channels, and rotational adiabaticity.⁵⁰⁻⁶⁰ Here we investigate how bimolecular reactions are affected when reactant molecules have amounts of rotational energy that are well beyond typical energies in a thermal ensemble.

In this study, we use strong optical fields based on shaped chirped pulses of 800 nm light. The shaped pulses excite CO through multiphoton absorption and C₂ Swan band emission is observed, evidence that electronically excited C₂ molecules

are formed from excited CO. We control the polarization of the pulsed light to either be angularly accelerating linear polarization or form a dynamic polarization grating. The angularly accelerating field is an optical centrifuge and is capable of preparing CO molecules with oriented angular momentum in rotational states up to $J = 80$. The dynamic polarization grating has a time-varying polarization that changes from linear to elliptical to circular and then back to linear within an optical cycle. The dynamic polarization grating does not impart appreciable torque to the aligned CO molecules. Using these two polarization schemes, we compare the Swan band emission characteristics to elucidate the role of rotation in reactions that form C_2 .

Here we study the effect that rotational energy has on bimolecular reactions initiated by strong optical fields with controlled polarization. The remainder of this chapter describes our experimental approach and presents our results. Power-dependent C_2 emission spectra are reported, providing information about the multiphoton nature of the CO excitation. A mechanism for production of C_2 is proposed based on known kinetic and photophysical data for CO. The extent of rotational excitation in CO is reported for both polarization configurations based on high-resolution transient IR absorption measurements. Relative reaction efficiencies are reported based on the observed emission intensities and finally the role of reactant rotational energy is discussed.

7.2 Experimental Details

Two polarization configurations of the pulsed 800 nm light are used in these experiments: optical centrifuge polarization (OCP) and a dynamic polarization

grating (DPG). Both optical polarizations are based on pairs of oppositely chirped pulses that are merged using a polarizing beam cube, then overlapped in time and space at the sample cell.

The instrumentation used to generate the pulses in this experiment is described in detail in Section 2.1.2. Figure 7.1 shows the spectral profiles of the pair of oppositely chirped pulses and indicates the direction of the chirps. Before entering the sample cell, the pair of pulses are combined spatially in a polarizing beam cube and sent through a quarter-wave ($\lambda/4$) plate. This set-up induces opposite circular polarization in the pair of pulses and creates the optical centrifuge. For the dynamic polarization grating, the quarter-wave plate is removed, and the pair of pulses have orthogonal linear polarization. The resulting polarization configurations are described in detail in the Section 2.1.4.

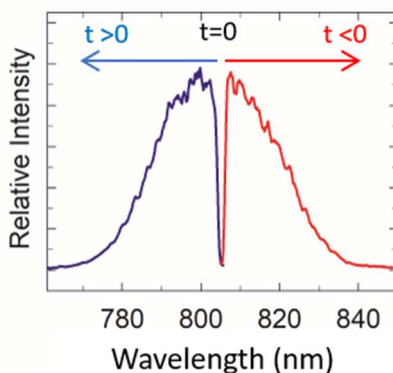


Figure 7.1 Spectral output from the pulse shaper.

The recombined pulses are focused to a beam waist of $w_0 = 53 \mu m$ at the center of a Pyrex sample cell containing spectroscopic grade CO gas (99.99% purity) at pressures of 25, 50, 75 or 100 Torr. In this study, the intensity of the

optical field ranges from $3.6 \times 10^{12} \text{ W cm}^{-2}$ (8 mJ/pulse) to $2.0 \times 10^{13} \text{ W cm}^{-2}$ (44 mJ/pulse).

Two types of measurements were performed with each polarization configuration. In the first, dispersed Swan band emission between $\lambda = 400 - 800 \text{ nm}$ was collected on an Ocean Optics 2000 spectrometer (1.5 nm FWHM) positioned at right angles to the pulsed laser propagation vector. The dispersed emission was collected as a function of laser power and CO pressure.

In the second type of measurement, high-resolution transient IR absorption signals were collected in a multipass cell (with 11 passes) for a number of CO ($X^1\Sigma^+, v = 0$) rotational states with $J = 62 - 73$ using polarization-sensitive IR spectroscopy. These measurements are used to establish the extent of rotational excitation in the CO sample with the optical centrifuge and with the dynamic polarization grating. A single frequency quantum cascade laser operating at $\lambda = 4.3 \mu\text{m}$ was tuned to the frequency of individual transitions and transient absorption was measured. This technique is described in Section 2.2.

7.3 Results and Discussion

Here we present the results of power- and pressure-dependent dispersed emission measurements when CO is excited by a strong optical field with the two different optical polarization. We analyze the multiphoton absorption of CO and consider the pathways that are likely to lead to C_2 formation. For both optical polarizations, the extent of CO rotational energy is characterized by high-resolution

transient IR absorption and the influence of rotation on the bimolecular reactions is discussed.

7.3.1 Dispersed Emission Measurements: C₂ Formation

Figure 7.2 shows the power-dependent emission spectra observed in a 100 Torr sample of CO. The spectra are identified as the well-known C₂ Swan bands ($d^3\Pi_g \rightarrow a^3\Pi_u$).⁶¹⁻⁶⁸ The Swan-band peaks correspond to different vibronic transitions from the excited $d^3\Pi_g$ state: the $\Delta v = 0$ peak is at $\lambda = 516$ nm and the $\Delta v = -1$ peak is at $\lambda = 467$ nm. Interestingly, no emission from the CO Angstrom bands ($B^1\Sigma^+ \rightarrow A^1\Pi$) was seen in our measurements.⁶⁹ The lack of observed emission is consistent with a short-lived CO $B^1\Sigma^+$ state that is collisionally quenched, given the pressures used in our experiments. The kinetics will be considered in more detail later.

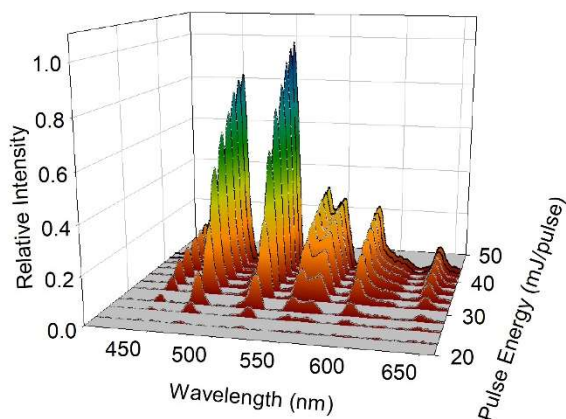


Figure 7.2 Power-dependent Swan-band emission spectra observed with a CO pressure of 100 Torr and optical centrifuge polarization.

The observation of Swan-band emission from a pure sample of CO is evidence that excited C₂ ($d^3\Pi_g$) is a reaction product when CO is excited in an

intense laser field. The emission intensity is a measure of the C_2 ($d^3\Pi_g$) yield. Figure 7.3 shows the power-dependent integrated emission at four CO pressures, ranging from 25 to 100 Torr, for both optical polarizations. The emission threshold decreases with increasing pressure. Above threshold, the emission intensity increases with increasing laser power and for pressures of 50-100 Torr, there is more emission for the DPG than the OCP at the higher powers.

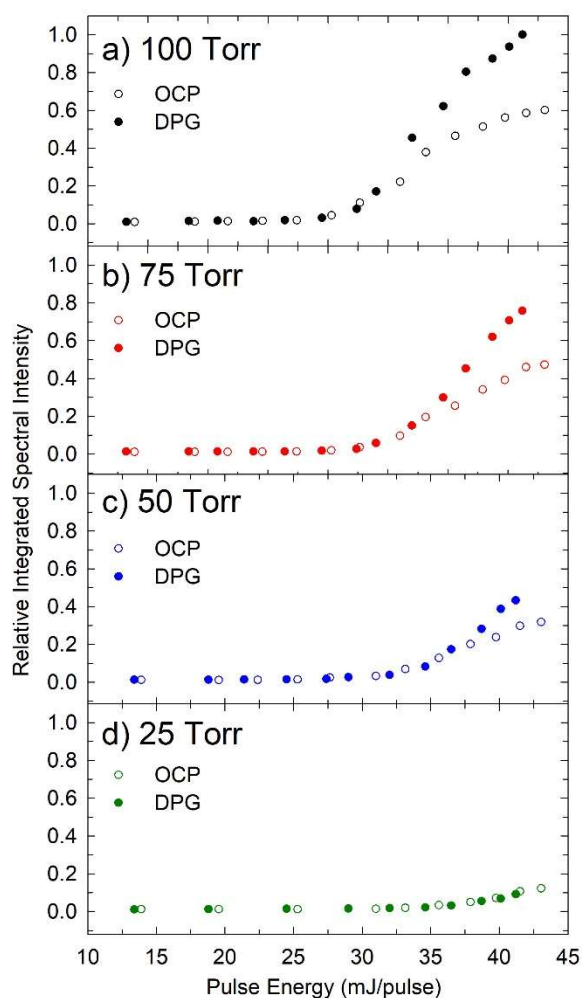


Figure 7.3. Relative integrated emission intensities at CO pressures of a) 100 Torr, b) 75 Torr, c) 50 Torr, and d) 25 Torr with either the optical centrifuge polarization (OCP) or dynamic polarization grating (DPG) configurations.

Figure 7.4 shows a comparison of the relative integrated C₂ emission intensity for the OCP and DPG configurations as a function of cell pressure with an optical intensity of $I = 1.8 \times 10^{13} \text{ W cm}^{-2}$ (41 mJ/pulse). The difference in emission for the two optical polarization schemes increases with increasing pressure from 50 to 100 Torr. At 100 Torr and the highest pulse energies, the DPG leads to nearly twice the emission of the OCP. This observation shows that the DPG is twice as effective at converting CO to C₂($d^3\Pi_g$) under these conditions.

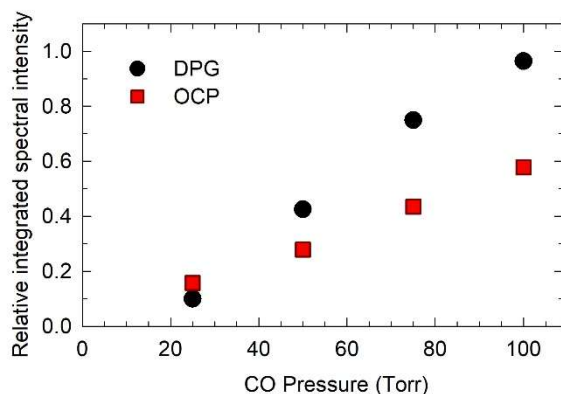


Figure 7.4. Comparison of relative integrated C₂ emission intensities for optical centrifuge polarization (OCP) and the dynamic polarization grating (DPG) as a function of cell pressure with $I = 1.8 \times 10^{13} \text{ W cm}^{-2}$ (41 mJ/pulse).

7.3.2 Multiphoton Absorption of CO

The multiphoton absorption of CO is characterized using the linear portions of the energy-dependent data in Figure 7.3. Figure 7.5 shows the logarithmic plots and with power-law fits for both optical polarizations. The slopes from the fitting analysis are listed in Figure 7.5 and indicate that CO absorbs at least seven photons prior to the formation of C₂ for both the OCP and DPG. The energy of seven 800-nm photons is enough to excite CO to the $B^1\Sigma^+$ state, as indicated by the red arrow in the energy

level diagram shown in Figure 7.6.⁶¹ Absorption of eight photons would excite CO to the $F^1\Sigma^+$ state.

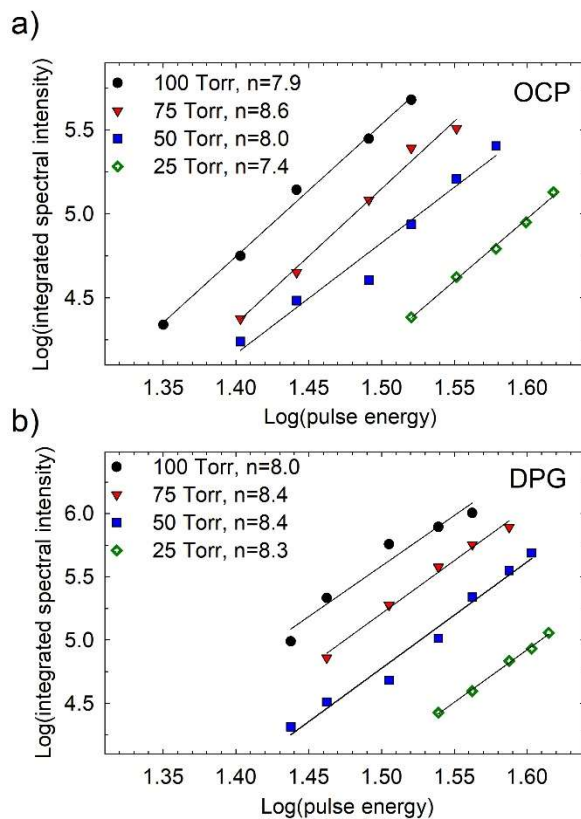


Figure 7.5. Power-dependent analysis to determine the lower limit for the number of photons absorbed by CO prior to formation of $C_2(d^3\Pi_g)$. Logarithmic plots of integrated spectral intensity vs pulse energy for (a) the optical centrifuge polarization (OCP) and (b) the dynamic polarization grating (DPG).

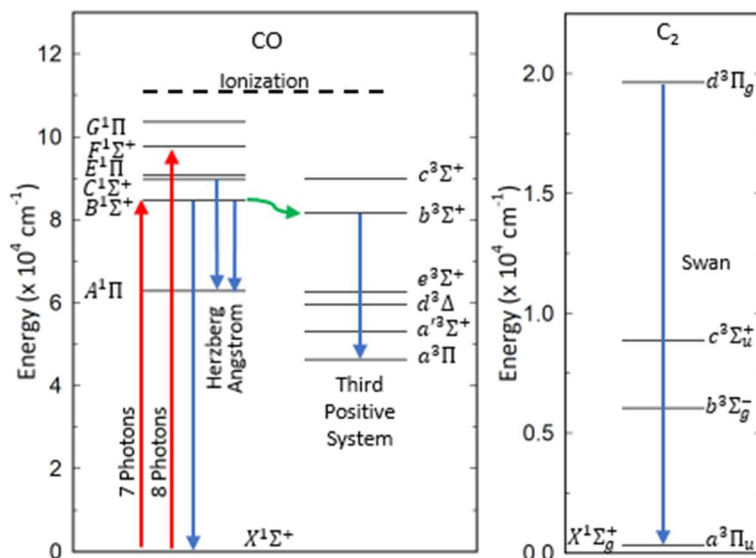
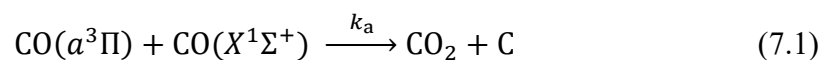


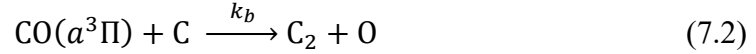
Figure 7.6. Electronic energy levels and terms for CO and C₂. The red arrows indicate multiphoton absorption of seven and eight 800 nm photons. Emission pathways are indicated with blue arrows and collision-induced intersystem crossing (denoted in green) leads to excitation of CO triplet states.

7.3.3 Mechanism of C₂ Formation

Here we consider the mechanism by which C₂ is formed following the multiphoton absorption of CO. In 1981, C₂ Swan-band emission was reported by Faust and coworkers after multiphoton UV excitation of CO.⁶² Their time-resolved emission data indicate the presence of a long-lived precursor to the formation of C₂ from excited CO. In 1991, Ivanov and coworkers identified the CO (*a*³Π) state as important in the production of C₂ in CO/He plasmas. They reported a relatively small rate constant of $k_a = 10^{-12} \text{ cm}^3 \text{ molecule}^{-1} \text{ s}^{-1}$ for the reaction of triplet CO with ground state CO:



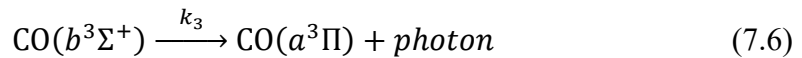
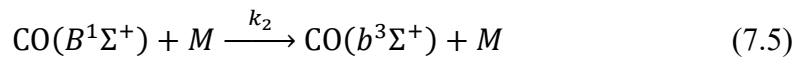
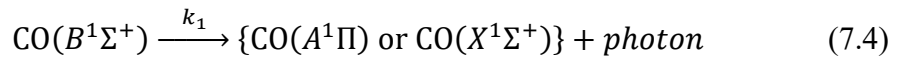
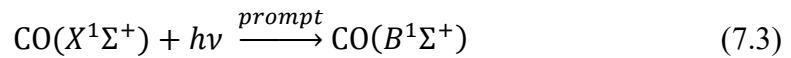
They postulated that the formation of C_2 occurs by reactions of $CO(a^3\Pi)$ and a C atom, as in Equation 7.2.

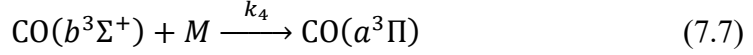


It is likely that the rate constant for the second reaction is fast compared to the production rate of C atoms.

The $CO(a^3\Pi)$ state is a likely reactant in C_2 formation, based on the CO/He plasma studies discussed above. Here we consider the kinetics of the $CO(B^1\Sigma^+)$ state that is prepared by multiphoton absorption and ultimately leads to formation of the $CO(a^3\Pi)$ state. Both radiative decay and collisional energy transfer are included in the kinetics. If higher energy CO states are prepared in the initial multiphoton step, it is likely that the relaxation will be even faster.

We treat the initial multiphoton excitation of CO as prompt, because the highest pulse intensity occurs early in the shaped pulses. In this analysis, we begin with initial excitation to the B state, as shown in Equation 7.3 and Figure 7.6. The B state can relax by emission to the X and A states (Equation 7.4) and by collision-induced intersystem crossing to the $CO(b^3\Sigma^+)$ state (Equation 7.5). The $CO(b^3\Sigma^+)$ state can relax by emission (Equation 7.6) and by collisions to the $CO(a^3\Pi)$ state (Equation 7.7).





We have modelled the time-dependent formation of the CO $a^3\Pi$ state using integrated kinetic equations for the species above. The rate constants are summarized in Table 7.1.

Table 7.1 Rate constants for formation of the CO($a^3\Pi$) state.

Rate constant	Value	Source
$k_1 = \frac{1}{\tau_A} + \frac{1}{\tau_X}$	$7.35 \times 10^8 \text{ s}^{-1}$	$\tau_A = 6.8 \times 10^{-8} \text{ s};$ ⁷⁰ $\tau_X = 1.7 \times 10^{-8} \text{ s};$ ⁷¹
k_2	$1.82 \times 10^{-10} \text{ cm}^3 \text{ molecule}^{-1} \text{ s}^{-1}$	70
k_3	$1.03 \times 10^7 \text{ s}^{-1}$	72
k_4	$1.01 \times 10^{-9} \text{ cm}^3 \text{ molecule}^{-1} \text{ s}^{-1}$	72

The kinetic equations for the formation of the CO ($a^3\Pi$) state following multiphoton excitation to the ($B^1\Sigma^+$) state are developed here. The following definitions are used in the kinetic equations: $B \equiv \text{CO}(B^1\Sigma^+)$, $A \equiv \text{CO}(A^1\Pi)$, $X \equiv \text{CO}(X^1\Sigma^+)$, $b \equiv \text{CO}(b^3\Sigma^+)$ and $a \equiv \text{CO}(a^3\Pi)$. Under pseudo-first order conditions, the loss of CO($B^1\Sigma^+$) are given by

$$\frac{d[B]}{dt} = -(k_1 + k_2[M])t \quad (7.8)$$

and

$$\frac{[B]}{[B]_0} = e^{-(k_1+k_2[M])t}. \quad (7.9)$$

The combined formation of CO($A^1\Pi$) and CO($X^1\Sigma^+$) are given by

$$\frac{d([A]+[X])}{dt} = k_1[B] = k_1[B]_0 e^{-(k_1+k_2[M])t} \quad (7.10)$$

and

$$\frac{[A]+[X]}{[B]_0} = \frac{k_1[B]_0}{k_1+k_2[M]} \left(1 - e^{-(k_1+k_2[M])t}\right). \quad (7.11)$$

The formation and decay of $\text{CO}(b^3\Sigma^+)$ are given by

$$\frac{d[b]}{dt} = k_2[M][B] - (k_3 + k_4[M])[b] \quad (7.12)$$

and

$$\frac{[b]}{[B]_0} = \frac{k_2[M]}{k_3+k_4[M]-k_2[M]} \left[e^{-(k_1+k_2[M])t} - e^{-(k_3+k_4[M])t} \right]. \quad (7.13)$$

Finally, the appearance of $\text{CO}(a^3\Pi)$ is given by

$$\frac{d[a]}{dt} = (k_3 + k_4[M])[b] \quad (7.14)$$

and

$$\frac{[a]}{[B]_0} = \beta \left[(k_1 + k_2[M]) \left[1 - e^{-(k_3+k_4[M])t} \right] - (k_3 + k_4[M]) \left[1 - e^{-(k_1+k_2[M])t} \right] \right], \quad (7.15)$$

where

$$\beta = \frac{k_2[M]}{[(k_1+k_2[M])-(k_3+k_4[M])](k_1+k_2[M])}. \quad (7.16)$$

Figure 7.7 shows the pressure-dependent kinetics for $[B]$, $[A]$, $[X]$, $[b]$ and $[a]$ using Equations 7.9, 7.11, 7.13 and 7.15 and the rate constants from Table 7.1. The number density of the $\text{CO}(a^3\Pi)$ state increases with increasing pressure because of the collisional energy transfer.

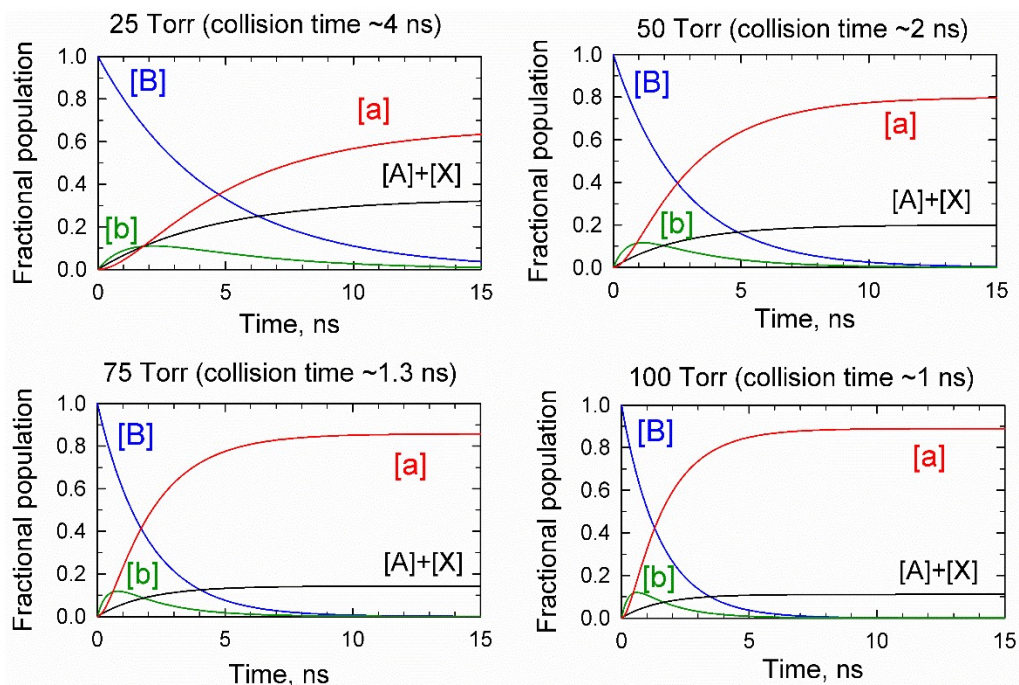


Figure 7.7. Time-dependent fractional populations of CO $B^1\Sigma^+(B)$, $A^1\Pi(A)$, $X^1\Sigma^+(X)$, $b^3\Sigma^+(b)$ and $a^3\Pi(a)$ for the four pressures used in our experiments. Formation of the $a^3\Pi$ state is enhanced at higher pressures shows the fractional populations for the CO states at 100 Torr pressure. The relaxation of the b state occurs readily at pressures of 25-100 Torr and is predominantly collision induced.

The modelling shows that at the pressures of our experiments, the CO ($a^3\Pi$) state is formed rapidly, with the collisional quenching steps occurring much faster than CO emission. The yield of the CO ($a^3\Pi$) state, relative to the initial number density of the B state, increases from 66% at 25 Torr to 98% at 100 Torr. The natural lifetime for appearance of the CO ($a^3\Pi$) state decreases from 5 ns at 25 Torr to less than 2 ns at 100 Torr. The average time between collisions is 4 ns at 25 Torr and 1 ns at 100 Torr. Although the formation of the CO ($a^3\Pi$) state occurs rapidly under our conditions, its reaction with ground state CO proceeds slowly (Equation 7.1). These results suggest that the long-lived precursor identified by Faust and coworkers in their time-resolved C_2 emission studies is likely the CO ($a^3\Pi$) state.⁶²

7.3.4 Effect of Rotational Excitation on CO Reactivity

The relative emission intensities in Figure 7.4 show that the optical field polarization influences the amount of C_2 ($d^3\Pi_g$) that results from strong field excitation of CO. At the highest powers, we see that multiphoton CO excitation in the dynamic polarization grating yields twice as much C_2 as does excitation in the optical centrifuge. Here we consider the effect of the field polarization on the multiphoton absorption process and the role of CO rotation on the reactions that form C_2 .

The polarization of the optical field does not appear to affect the multiphoton absorption process. Our power-dependent data (Figure 7.5) show that CO excitation involves a similar number of photons for both optical polarization schemes. Strickland and coworkers have shown in photodissociation experiments with polarized light that adiabatic alignment in strong fields results in multiphoton absorption with a directionality that follows the field, as long as the field does not vary too quickly.⁷³ In our experiments using oppositely chirped pulses, molecules aligned in the strong field adiabatically follow the field until the time-dependent polarization frequency varies too quickly. For the optical centrifuge polarization, molecules are spun into high rotational states until the field becomes too weak to trap them or spins too fast for them to keep up. The polarization of the field works together with the molecule's angular momentum to continue to ramp them into higher J states. In the dynamic polarization grating, there is no comparable rotational excitation through alignment in the field. In this case, the field polarization varies between right and left circular.

The extent of rotational excitation in CO was measured below the emission threshold using high-resolution transient IR absorption for CO states with $J > 60$. Transient signals for individual CO rotational states were collected at 5 Torr to avoid interference from C₂ emission. Figure 7.8a shows the C₂ emission thresholds as a function of CO pressure; no emission is observed at pressures below 10 Torr.

For both optical polarizations, a number of CO rotational states with $J = 62 - 73$ and E_{rot} up to $10,400 \text{ cm}^{-1}$ were investigated. The transient signals for CO $J = 70$ are shown in Figure 7.8b for the OCP and the DPG. Figure 7.8c shows the relative CO populations excited with each polarization scheme, based on IR polarization-dependent measurements, where the total relative state-specific population is determined by $S(J, t) = 2S_{\parallel}(t) + S_{\perp}(t)$. Here, $S_{\parallel}(S_{\perp})$ is the transient signal for parallel (perpendicular) IR detection as described in Section 2.2.6. For each J state, the CO signals with the OCP are larger by at least a factor of two than those with the DPG. Figure 7.8d shows the ratio of $S(J)$ values for OCP and DPG. The ratio increases with J and has an average value of 3.2 for this range of states. These measurements show that the number densities of high- J CO molecules are larger with the OCP. Although the OCP traps and spins molecules to high rotational states by the angularly accelerating optical field, the DPG can induce rotational excitation through ladder-climbing Raman transitions based on the oppositely chirped pulses. An analysis performed by Vitanov and Girard showed that linearly polarized, oppositely chirped pulses can lead to extreme rotation; however, rotational excitation through induced Raman transitions was for four-fold less intense than excitation with the

optical centrifuge.¹⁸ We attribute the reduced $C_2(d^3\Pi_g)$ yield to the increased number of highly rotationally excited CO molecules made with the OCP.

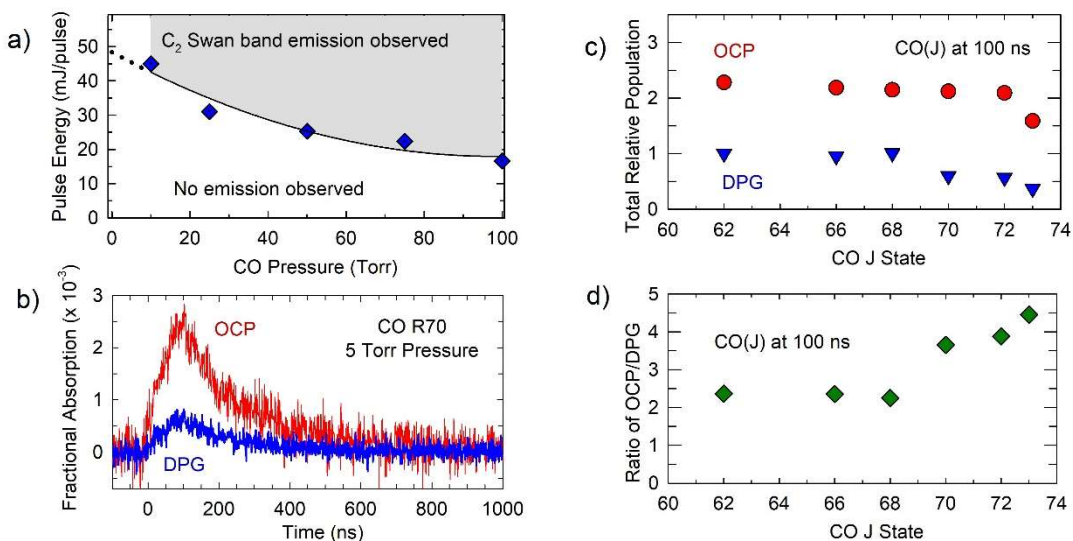


Figure 7.8. a) The pressure dependence of the Swan band emission threshold. b) *R*-branch high-resolution transient IR absorption for the CO $J = 70$ state with OCP and DPG excitation. c) J -dependent transient intensities at 100 ns based on polarization-sensitive IR detection. d) Ratio of $S(J)$ values with OCP and DPG.

Molecules in extreme rotational states have rotational periods (t_{rot}) that can be much shorter than the duration of a collision (t_{col}), thereby reducing the effectiveness of collisional energy transfer and bimolecular reactions. This idea is at the heart of the rotational adiabaticity parameter, which is defined as $a = t_{col}/t_{rot}$. A simple rigid rotor model indicates that CO ($J = 70$) has an adiabaticity parameter of $a = 6$, based on 300 K collision velocities. This situation is the opposite of the sudden approximation, where rotation is considered fixed relative to the collision. The sudden approximation is commonly used in calculations of reaction rates. Being able to prepare molecules with large amounts of rotational energy using an optical

centrifuge provides us the opportunity to explore collisional behavior under rotationally adiabatic conditions.

Previous studies in our laboratory have shown the importance of rotational adiabaticity in the collisional relaxation of optically centrifuged CO₂ ($J = 100$) with Ar and He. With its small mass, helium has very short collision times relative to the CO₂ ($J = 100$) rotational period. Argon on the other hand has collision times with CO₂ that are 2.5 times longer than He/CO₂ collisions. We find that He is significantly more effective than Ar at quenching CO₂ ($J = 100$), despite having similar scattering cross sections.¹⁵ We speculate that similar dynamics could well be involved in the bimolecular reactions of CO when its excitation includes large amounts of rotational energy. These processes will be the subject of future investigations.

7.4 Conclusion

Here, we have used strong optical fields based on shaped chirped laser pulses to excite CO via multiphoton absorption and investigate how CO rotation affects the yield of bimolecular reactions that form C₂. The observation of Swan band emission initiated by the strong field pulse shows that C₂($d^3\Pi_g$) is produced from bimolecular reactions of excited CO. Kinetic modelling using known collisional quenching rates and emission lifetimes suggests that the CO ($a^3\Pi$) state is a likely reactant candidate. We see that larger number densities of rotationally excited CO (with $J > 60$) are made with the optical centrifuge than with the dynamic polarization grating. Reduced intensity of the Swan-band emission indicates that fewer C₂ molecules are formed with the optical centrifuge. Based on these findings, we attribute the reduced C₂ yield

to the presence large amounts rotational energy in the CO reactants. These studies show how strong optical fields from shaped pulses can induce new types of chemistry and we hope that these results will motivate new theoretical studies of such processes.

Chapter 8: Conclusions and Future Work

The research described in this thesis has focused on the development and use of new tools to study molecules in extreme rotational states. This work used an optical centrifuge coupled to a state-resolved high-resolution transient IR absorption spectrometer to investigate optically centrifuged N₂O, CO₂, and CO molecules. These studies asked how large amounts of rotational energy affect energy transfer dynamics, reorientation lifetimes, and bimolecular reactions. These studies get at the heart of the correspondence principle for the quantum and classical behavior of molecular rotation in the high energy limit.

The studies reported in this thesis were made possible by the development of a multi-pass IR detection cell that resulted in a 40-fold increase in observed signal-to-noise levels of transient IR signals. We also developed a tunable optical centrifuge that allowed us to release centrifuged molecules from the optical trap in a controlled manner at desired angular frequencies. These developments made it possible to measure nascent distributions of optically centrifuged molecules and study their dynamics.

The first step to study molecules with extreme rotational energy was to identify the IR transition frequencies for high- J states that had not been observed previously. Prior to this work, observed IR transitions had been reported for N₂O and CO₂ transitions up to $J = 100$ and $J = 146$, respectively. In Chapter 3, we predicted and measured IR transition frequencies for N₂O with $J = 140$ -205. We found that our predictions, based on a 3rd-order expansion of the rigid rotor model, did a very good job at describing the R -branch transitions of N₂O for states with $J \leq 205$. The effect

of rotational energy on the collisional energy transfer and reorientation dynamics was investigated by measuring translational energy gains and orientational anisotropies for a number of N₂O states with $J = 92-195$ and energies $E_{rot} \approx 3,600 - 16,000 \text{ cm}^{-1}$. The N₂O study shows that molecules in states with $J = 160-195$ undergo collisions that exchange energy through near-resonant rotation-to-rotation energy transfer. Molecules in lower rotational states ($J = 92$) gain more translational energy as a result of non-resonant rotation-to-rotation energy transfer.

The spectroscopy of optically centrifuged CO₂ molecules is reported in Chapter 4 where CO₂ IR transitions were measured up to $J \leq 280$ and $E_{rot} \approx 30,000 \text{ cm}^{-1}$. These experiments were informed by the methods used in Chapter 3 for N₂O spectroscopy. New IR transitions were readily observed up to $J = 256$, then a spectral perturbation was observed that hindered the identification of IR transition frequencies for $J > 256$. Calculated transition frequencies based on effective Hamiltonian calculations for CO₂ up to $J = 300$ are reported in the CDSD4000. A comparison of our observed IR transition frequencies for CO₂ states with $186 \leq J \leq 256$ with those reported in the CDSD4000 showed remarkably good agreement, and enabled further measurements of IR transition frequencies for CO₂ states as high as $J = 280$. The perturbed CO₂ states have mixed character, as they are coupled to excited vibrational states with bending motion.

In Chapter 5, the full distribution of optically centrifuged CO was characterized. We found that the full bandwidth of our optical centrifuge is capable of populating CO states as high as $J = 80$ with $E_{rot} \approx 12,400 \text{ cm}^{-1}$. The results of Chapter 5 provide information indicating that our centrifuge is capable of driving CO₂

to at least $J \approx 370$. A major goal of this work was to identify nascent distributions of optically centrifuged molecules. Results from this chapter motivated the development of a tunable optical centrifuge in order to measure the nascent distribution of optically centrifuged CO₂.

In Chapter 6, a tunable optical centrifuge was used to measure the nascent population distributions of optically centrifuged CO and CO₂. The capture and acceleration efficiencies for CO and CO₂ were characterized by measurements of their nascent distributions. We found that optically centrifuged CO₂ has a number density three-fold larger than that of CO. The results in this chapter motivate future studies using a tunable optical centrifuge for CO₂ to detect the elusive states near the perturbation. The centrifuge was tuned such that the bulk of trapped CO₂ molecules are released from the trap in J states near the spectral perturbation. The increase in population near the perturbation would make possible dynamical studies of mixed states.

In Chapter 7, we investigated how rotational energy affects bimolecular reactions. Specifically, we studied CO reactions that form C₂. For this reaction, rotational energy of the CO reactants was shown to slow the progress of bimolecular reactions that form C₂. Using two polarization configurations, it would be possible to investigate the role in which rotational energy plays for other chemical reactions.

The results presented in this thesis reveal important clues about the behavior of molecules in extreme rotational states. We have learned that quantum models for molecular rotation work surprisingly well at describing N₂O and CO₂ high- J rotational states. Observed IR transitions of CO₂ with as much 280 units of angular

momentum and $30,000\text{ cm}^{-1}$ of rotational energy show excellent agreement with predicted values. This finding shows that centrifugal distortion in the high J -states of CO_2 do not overcome the chemical forces that determine molecular structure. New spectral perturbations were observed from state coupling of vibrationally excited states that only occur in the presence of large rotational angular momenta. Near-resonant rotation-to-rotation collisional energy transfer of high- J molecules leads to delayed translational energy release in ensembles of molecular super rotors and orientational anisotropy lifetimes increase as a function of molecular angular momentum. These phenomena show that how energy partitioning dynamics of molecular super rotors are distinct from low energy molecules. These findings also lay the groundwork for exciting new studies that investigate the role of chemical and centrifugal forces in molecules and the ways in which vibrational and rotational energies interact in polyatomic molecules.

Appendix: Dunham Coefficients for CO

The term energy for a single (v, J) state is given by

$$F_{vJ} = \omega_e \left(v + \frac{1}{2} \right) - \omega_e x_e \left(v + \frac{1}{2} \right)^2 + \omega_e y_e \left(v + \frac{1}{2} \right)^3 + \omega_e z_e \left(v + \frac{1}{2} \right)^4 + B_v J(J+1) - D_e J^2(J+1)^2 + H_e J^3(J+1)^3 + \dots, \quad (\text{A.1})$$

where

$$B_v = B_e - \alpha_e \left(v + \frac{1}{2} \right) + \gamma_e \left(v + \frac{1}{2} \right)^2 + \dots. \quad (\text{A.2})$$

In cases where B_v/ω_e is small, the spectral constants in Equation A.1 can be related to the Dunham coefficients as shown in Table A.1, as given by Townes and Schawlow.

Table A.1 Relationships between spectral constants and Dunham coefficients.

$Y_{10} \approx \omega_e$	$Y_{20} \approx \omega_e x_e$	$Y_{30} \approx \omega_e y_e$
$Y_{01} \approx B_e$	$Y_{11} \approx -\alpha_e$	$Y_{21} \approx \gamma_e$
$Y_{02} \approx -D_e$	$Y_{12} \approx -\beta_e$	$Y_{40} \approx \omega_e z_e$
$Y_{03} \approx H_e$		

Guelachvili et al. report Dunham coefficients for CO, which are shown in

Table A.2.³²

Table A.2 Reported Dunham coefficients (in cm^{-1}) for the main isotope of CO based on absorption and plasma emission spectra. Data up to $J = 93$ was used in the global fit.

$Y_{10} =$ 0.2169813079×10^4	$Y_{20} =$ 0.1328790597×10^2	$Y_{30} =$ $0.1041444730 \times 10^{-1}$
$Y_{01} =$ 0.1931280862×10^1	$Y_{11} =$ $-0.1750410455 \times 10^{-1}$	$Y_{21} =$ $0.5422101371 \times 10^{-6}$
$Y_{02} =$ $-0.6120747566 \times 10^{-5}$	$Y_{12} =$ $0.9449843095 \times 10^{-9}$	$Y_{40} =$ $0.6921598529 \times 10^{-4}$
$Y_{03} =$ $0.5555386989 \times 10^{-11}$		

To calculate the energies of rotational states for the upper and lower vibrational states

($v = 0, J = 0 \rightarrow v = 1, J = 1$) we use:

$$F_{v,J} = Y_{10} \left(v + \frac{1}{2} \right) - Y_{20} \left(v + \frac{1}{2} \right)^2 + Y_{30} \left(v + \frac{1}{2} \right)^3 + Y_{40} \left(v + \frac{1}{2} \right)^4 + \\ \left[Y_{01} + Y_{11} \left(v + \frac{1}{2} \right) + Y_{21} \left(v + \frac{1}{2} \right)^2 \right] J(J + 1) + Y_{02} J^2 (J + 1)^2 + Y_{03} J^3 (J + 1)^3 \quad (\text{A.3})$$

The IR transition frequencies are the difference in the energies of the upper and lower states.

Bibliography

1. Ohshima, Y.; Hasegawa, H., Coherent rotational excitation by intense nonresonant laser fields. *International Reviews in Physical Chemistry* **2010**, *29* (4), 619-663.
2. Karras, G.; Ndong, M.; Hertz, E.; Sugny, D.; Billard, F.; Lavorel, B.; Faucher, O., Polarization Shaping for Unidirectional Rotational Motion of Molecules. *Physical Review Letters* **2015**, *114* (10), 5.
3. Korech, O.; Steinitz, U.; Gordon, R. J.; Averbukh, I. S.; Prior, Y., Observing molecular spinning via the rotational Doppler effect. *Nature Photonics* **2013**, *7* (9), 711-714.
4. Kitano, K.; Hasegawa, H.; Ohshima, Y., Ultrafast Angular Momentum Orientation by Linearly Polarized Laser Fields. *Physical Review Letters* **2009**, *103* (22), 4.
5. Bloomquist, C.; Zhdanovich, S.; Milner, A. A.; Milner, V., Directional spinning of molecules with sequences of femtosecond pulses. *Physical Review A* **2012**, *86* (6), 8.
6. Bitter, M.; Milner, V., Rotational excitation of molecules with long sequences of intense femtosecond pulses. *Physical Review A* **2016**, *93* (1), 7.
7. Karczmarek, J.; Wright, J.; Corkum, P.; Ivanov, M., Optical centrifuge for molecules. *Physical Review Letters* **1999**, *82* (17), 3420-3423.
8. Villeneuve, D. M.; Aseyev, S. A.; Dietrich, P.; Spanner, M.; Ivanov, M. Y.; Corkum, P. B., Forced molecular rotation in an optical centrifuge. *Physical Review Letters* **2000**, *85* (3), 542-545.
9. Yuan, L. W.; Toro, C.; Bell, M.; Mullin, A. S., Spectroscopy of molecules in very high rotational states using an optical centrifuge. *Faraday Discussions* **2011**, *150*, 101-111.
10. Yuan, L. W.; Teitelbaum, S. W.; Robinson, A.; Mullin, A. S., Dynamics of molecules in extreme rotational states. *Proceedings of the National Academy of Sciences of the United States of America* **2011**, *108* (17), 6872-6877.
11. Toro, C.; Liu, Q. N.; Echebiri, G. O.; Mullin, A. S., Inhibited rotational quenching in oriented ultra-high rotational states of CO₂. *Molecular Physics* **2013**, *111* (12-13), 1892-1901.
12. Murray, M. J.; Ogden, H. M.; Toro, C.; Liu, Q. N.; Burns, D. A.; Alexander, M. H.; Mullin, A. S., State-Specific Collision Dynamics of Molecular Super Rotors with Oriented Angular Momentum. *Journal of Physical Chemistry A* **2015**, *119* (50), 12471-12479.
13. Murray, M. J.; Ogden, H. M.; Toro, C.; Liu, Q. N.; Mullin, A. S., Impulsive Collision Dynamics of CO Super Rotors from an Optical Centrifuge. *Chemphyschem* **2016**, *17* (22), 3692-3700.
14. Murray, M. J.; Ogden, H. M.; Mullin, A. S., Anisotropic kinetic energy release and gyroscopic behavior of CO₂ super rotors from an optical centrifuge. *Journal of Chemical Physics* **2017**, *147* (15), 10.
15. Murray, M. J.; Ogden, H. M.; Mullin, A. S., Importance of rotational adiabaticity in collisions of CO₂ super rotors with Ar and He. *Journal of Chemical Physics* **2018**, *148* (8), 7.

16. Milner, A. A.; Korobenko, A.; Hepburn, J. W.; Milner, V., Probing molecular potentials with an optical centrifuge. *Journal of Chemical Physics* **2017**, *147* (12), 6.
17. Binauld, Q.; Riviere, P.; Soufiani, A., A note on radiation preheating of some hydrocarbons by combustion products. *Combustion and Flame* **2018**, *194*, 128-134.
18. Vitanov, N. V.; Girard, B., Adiabatic excitation of rotational ladder by chirped laser pulses. *Physical Review A* **2004**, *69* (3), 13.
19. Korobenko, A.; Milner, A. A.; Milner, V., Direct Observation, Study, and Control of Molecular Superrotors. *Physical Review Letters* **2014**, *112* (11), 5.
20. Gordon, I. E.; Rothman, L. S.; Hill, C.; Kochanov, R. V.; Tan, Y.; Bernath, P. F.; Birk, M.; Boudon, V.; Campargue, A.; Chance, K. V.; Drouin, B. J.; Flaud, J. M.; Gamache, R. R.; Hodges, J. T.; Jacquemart, D.; Perevalov, V. I.; Perrin, A.; Shine, K. P.; Smith, M. A. H.; Tennyson, J.; Toon, G. C.; Tran, H.; Tyuterev, V. G.; Barbe, A.; Csaszar, A. G.; Devi, V. M.; Furtenbacher, T.; Harrison, J. J.; Hartmann, J. M.; Jolly, A.; Johnson, T. J.; Karman, T.; Kleiner, I.; Kyuberis, A. A.; Loos, J.; Lyulin, O. M.; Massie, S. T.; Mikhailenko, S. N.; Moazzen-Ahmadi, N.; Muller, H. S. P.; Naumenko, O. V.; Nikitin, A. V.; Polyansky, O. L.; Rey, M.; Rotger, M.; Sharpe, S. W.; Sung, K.; Starikova, E.; Tashkun, S. A.; Vander Auwera, J.; Wagner, G.; Wilzewski, J.; Wcislo, P.; Yu, S.; Zak, E. J., The HITRAN2016 molecular spectroscopic database. *Journal of Quantitative Spectroscopy & Radiative Transfer* **2017**, *203*, 3-69.
21. Steinitz, U.; Khodorkovsky, Y.; Hartmann, J. M.; Averbukh, I. S., Dynamics and Hydrodynamics of Molecular Superrotors. *Chemphyschem* **2016**, *17* (22), 3795-3810.
22. Khodorkovsky, Y.; Steinitz, U.; Hartmann, J. M.; Averbukh, I. S., Collisional dynamics in a gas of molecular super-rotors. *Nature Communications* **2015**, *6*, 6.
23. Paulec, M.; Marciniak, M.; Gross, K.; Azevedo, D. In *Infrared Signature Measurements of a Jet Turbine Using a Hyperspectral Imager for Combustion Diagnostics*, 24th SPIE Conference on Algorithms and Technologies for Multispectral, Hyperspectral, and Ultraspectral Imagery, Orlando, FL, Apr 17-19; Spie-Int Soc Optical Engineering: Orlando, FL, 2018.
24. Swain, M. R.; Tinetti, G.; Vasisht, G.; Deroo, P.; Griffith, C.; Bouwman, J.; Chen, P.; Yung, Y.; Burrows, A.; Brown, L. R.; Matthews, J.; Rowe, J. F.; Kuschnig, R.; Angerhausen, D., Water, Methane, and Carbon Dioxide Present in the Dayside Spectrum of the Exoplanet HD 209458b. *Astrophysical Journal* **2009**, *704* (2), 1616-1621.
25. Tinetti, G.; Deroo, P.; Swain, M. R.; Griffith, C. A.; Vasisht, G.; Brown, L. R.; Burke, C.; McCullough, P., Probing the Terminator Region Atmosphere of the Hot-Jupiter XO-1b with Transmission Spectroscopy. *Astrophysical Journal Letters* **2010**, *712* (2), L139-L142.
26. Wilquet, V.; Mahieux, A.; Vandaele, A. C.; Perevalov, V. I.; Tashkun, S. A.; Fedorova, A.; Koroblev, O.; Montmessin, F.; Dahoo, R.; Bertaux, J. L., Line parameters for the 01111-00001 band of $^{12}\text{C}^{16}\text{O}^{18}\text{O}$ from SOIR

- measurements of the Venus atmosphere. *Journal of Quantitative Spectroscopy & Radiative Transfer* **2008**, *109* (6), 895-905.
27. Bailey, J.; Meadows, V. S.; Chamberlain, S.; Crisp, D., The temperature of the Venus mesosphere from O₂ ($a^1\Delta_g$) airglow observations. *Icarus* **2008**, *197* (1), 247-259.
 28. Bailly, D.; CamyPeyret, C.; Lanquetin, R., Temperature measurement in flames through CO₂ and CO emission: New highly excited levels of CO₂. *Journal of Molecular Spectroscopy* **1997**, *182* (1), 10-17.
 29. Tashkun, S. A.; Perevalov, V. I., CDS-4000: High-resolution, high-temperature carbon dioxide spectroscopic databank. *Journal of Quantitative Spectroscopy & Radiative Transfer* **2011**, *112* (9), 1403-1410.
 30. Rothman, L. S.; Gordon, I. E.; Barber, R. J.; Dothe, H.; Gamache, R. R.; Goldman, A.; Perevalov, V. I.; Tashkun, S. A.; Tennyson, J., HITEMP, the high-temperature molecular spectroscopic database. *Journal of Quantitative Spectroscopy & Radiative Transfer* **2010**, *111* (15), 2139-2150.
 31. Teffo, J. L.; Sulakshina, O. N.; Perevalov, V. I., Effective Hamiltonian for Rovibrational Energies and Line-intensities of Carbon Dioxide. *Journal of Molecular Spectroscopy* **1992**, *156* (1), 48-64.
 32. Guelachvili, G.; Devilleneuve, D.; Farrenq, R.; Urban, W.; Verges, J., Dunham Coefficients for 7 Isotopic-Species of CO. *Journal of Molecular Spectroscopy* **1983**, *98* (1), 64-79.
 33. Armon, T.; Friedland, L., Capture into resonance and phase-space dynamics in an optical centrifuge. *Physical Review A* **2016**, *93* (4), 9.
 34. Armon, T.; Friedland, L., Quantum versus classical dynamics in the optical centrifuge. *Physical Review A* **2017**, *96* (3), 7.
 35. Sitz, G. O.; Farrow, R. L., Preparation and Decay of Alignment in N₂ ($v=1$). *Journal of Chemical Physics* **1994**, *101* (6), 4682-4687.
 36. Stapelfeldt, H.; Seideman, T., Colloquium: Aligning molecules with strong laser pulses. *Reviews of Modern Physics* **2003**, *75* (2), 543-557.
 37. Teilletbilly, D.; Malegat, L.; Gauyacq, J. P.; Abouaf, R.; Benoit, C., Electronic Excitation to the O₂($\pi^3_u \pi^3_g$) States in e⁻O₂ Collisions. *Journal of Physics B-Atomic Molecular and Optical Physics* **1989**, *22* (7), 1095-1102.
 38. Cryan, J. P.; Bucksbaum, P. H.; Coffee, R. N., Field-free alignment in repetitively kicked nitrogen gas. *Physical Review A* **2009**, *80* (6), 5.
 39. Fleischer, S.; Khodorkovsky, Y.; Prior, Y.; Averbukh, I. S., Controlling the sense of molecular rotation. *New Journal of Physics* **2009**, *11*, 15.
 40. Vallance, C., Generation, characterisation, and applications of atomic and molecular alignment and orientation. *Physical Chemistry Chemical Physics* **2011**, *13* (32), 14427-14441.
 41. Hou, H.; Huang, Y.; Gulding, S. J.; Rettner, C. T.; Auerbach, D. J.; Wodtke, A. M., Enhanced reactivity of highly vibrationally excited molecules on metal surfaces. *Science* **1999**, *284* (5420), 1647-1650.
 42. Baltuska, A.; Udem, T.; Uiberacker, M.; Hentschel, M.; Goulielmakis, E.; Gohle, C.; Holzwarth, R.; Yakovlev, V. S.; Scrinzi, A.; Hansch, T. W.; Krausz, F., Attosecond control of electronic processes by intense light fields. *Nature* **2003**, *421* (6923), 611-615.

43. Alekseev, V. A.; Grosser, J.; Hoffmann, O.; Rebentrost, F., Simultaneous optical excitation of Na electronic and CF₄ vibrational modes in Na+CF₄ collisions. *Journal of Chemical Physics* **2008**, *129* (20), 4.
44. Crim, F. F., Chemical reaction dynamics. *Proceedings of the National Academy of Sciences of the United States of America* **2008**, *105* (35), 12647-12648.
45. Palastro, J. P.; Penano, J.; Johnson, L. A.; Hafizi, B.; Wahlstrand, J. K.; Milchberg, H. M., Two-photon vibrational excitation of air by long-wave infrared laser pulses. *Physical Review A* **2016**, *94* (2), 7.
46. Miyamoto, Y.; Hara, H.; Hiraki, T.; Masuda, T.; Sasao, N.; Uetake, S.; Yoshimi, A.; Yoshimura, K.; Yoshimura, M., Vibrational excitation of hydrogen molecules by two-photon absorption and third-harmonic generation. *Journal of Physics B-Atomic Molecular and Optical Physics* **2018**, *51* (1), 7.
47. Rudert, A. D.; Martin, J.; Gao, W. B.; Halpern, J. B.; Zacharias, H., Collisional effects on angular momentum orientation in acetylene $\tilde{X}^1\Sigma_g^+$ ($v_2''=1, j''$). I. Preparation, detection and conservation in single collisions. *Journal of Chemical Physics* **1999**, *111* (21), 9549-9559.
48. Gershnel, E.; Averbukh, I. S., Orienting Asymmetric Molecules by Laser Fields with Twisted Polarization. *Physical Review Letters* **2018**, *120* (8), 6.
49. Li, J.; Bahns, J. T.; Stwalley, W. C., Scheme for state-selective formation of highly rotationally excited diatomic molecules. *Journal of Chemical Physics* **2000**, *112* (14), 6255-6261.
50. Gerlich, D.; Rox, T., Association Reactions with State Selected Ions at meV Collision Energies - CO⁺($v=0, J$) + 2CO (CO)₂⁺ + CO. *Zeitschrift Fur Physik D-Atoms Molecules and Clusters* **1989**, *13* (3), 259-268.
51. Urena, A. G.; Menendez, M.; Sabate, A. S.; Navarro, A. A., The Influence of Rotational Energy on the Cross-Section of Direct Reactions-Comparison of a Simple-Model with Classical Trajectories. *Chemical Physics Letters* **1991**, *176* (3-4), 315-321.
52. Viggiano, A. A.; Morris, R. A., Rotational and vibrational energy effects on ion-molecule reactivity as studied by the VT-SIFDT technique. *Journal of Physical Chemistry* **1996**, *100* (50), 19227-19240.
53. Glenwinkel-Meyer, T.; Gerlich, D., Single and merged beam studies of the reaction H₂⁺ ($v=0,1; j=0,4$) + H₂ → H₃⁺ + H. *Israel Journal of Chemistry* **1997**, *37* (4), 343-352.
54. Nobusada, K.; Moribayashi, K.; Nakamura, H., Quantum dynamics of O(³P) + HCl → OH + Cl Effects of reagent rotational excitation. *Journal of the Chemical Society-Faraday Transactions* **1997**, *93* (5), 721-726.
55. Paetow, L.; Unger, F.; Beichel, W.; Frenking, G.; Weitzel, K. M., Rotational dependence of the proton-transfer reaction HBr⁺+CO₂ → HOCO⁺+Br. I. Energy versus angular momentum effects. *Journal of Chemical Physics* **2010**, *132* (17), 7.
56. Xu, Y. T.; Xiong, B.; Chang, Y. C.; Ng, C. Y., Communication: Rovibrationally selected absolute total cross sections for the reaction H₂O⁺(X²B₁; $v_1^+ v_2^+ v_3^+=000$; N⁺Ka⁺Kc⁺) + D₂: Observation of the rotational enhancement effect. *Journal of Chemical Physics* **2012**, *137* (24), 4.

57. Welsch, R.; Manthe, U., Communication: Ro-vibrational control of chemical reactivity in $\text{H}+\text{CH}_4 \rightarrow \text{H}_2+\text{CH}_3$: Full-dimensional quantum dynamics calculations and a sudden model. *Journal of Chemical Physics* **2014**, *141* (5), 5.
58. Liu, R.; Wang, F. Y.; Jiang, B.; Czako, G.; Yang, M. H.; Liu, K. P.; Guo, H., Rotational mode specificity in the $\text{Cl} + \text{CHD}_3 \rightarrow \text{HCl} + \text{CD}_3$ reaction. *Journal of Chemical Physics* **2014**, *141* (7), 9.
59. Song, H. W.; Guo, H., Effects of reactant rotational excitations on $\text{H}_2 + \text{NH}_2 \rightarrow \text{H} + \text{NH}_3$ reactivity. *Journal of Chemical Physics* **2014**, *141* (24), 7.
60. Uhlemann, T.; Wallauer, J.; Weitzel, K. M., Self-reactions in the $\text{HCl}+(\text{DCI}^+) + \text{HCl}$ system: a state-selective investigation of the role of rotation. *Physical Chemistry Chemical Physics* **2015**, *17* (25), 16454-16461.
61. Herzberg, G., On the High Pressure Bands of Carbon and the Formation of C_2 Molecules. *Physical Review* **1946**, *70* (9-10), 762-764.
62. Faust, W. L.; Goldberg, L. S.; Craig, B. B.; Weiss, R. G., Time-Resolved C_2 Swan Emission from Short Pulse UV Fragmentation of CO- Evidence for 2C_2 Formation Mechanisms. *Chemical Physics Letters* **1981**, *83* (2), 265-269.
63. Alden, M.; Wallin, S.; Wendt, W., Applications of 2-Photon Absorption for Detection of CO in Combustion Gases. *Applied Physics B-Photophysics and Laser Chemistry* **1984**, *33* (4), 205-212.
64. Goldsmith, J. E. M.; Kearsley, D. T. B., C_2 Creation, Emission, and Laser-induced Fluorescence in Flames and Cold Gases. *Applied Physics B-Photophysics and Laser Chemistry* **1990**, *50* (5), 371-379.
65. Wallaart, H. L.; Piar, B.; Perrin, M. Y.; Martin, J. P., C_2 Formation in Vibrationally Excited CO. *Chemical Physics Letters* **1995**, *246* (6), 587-593.
66. Ionikh, Y. Z.; Kostyukevich, I. N.; Chernysheva, N. V., Concentration of C_2 molecules and the kinetics of their formation and destruction in a glow discharge in a He-CO mixture. *Optika I Spektroskopiya* **1996**, *80* (4), 590-594.
67. Tanabashi, A.; Hirao, T.; Amano, T.; Bernath, P. F., The Swan system of C_2 : A global analysis of Fourier transform emission spectra. *Astrophysical Journal Supplement Series* **2007**, *169* (2), 472-484.
68. Grigorian, G. M.; Cenian, A. In *Vibrational and chemical kinetics in plasma of CO containing gases*, Global Conference on Polymer and Composite Materials (PCM), Ningbo, PEOPLES R CHINA, May 27-29; Iop Publishing Ltd: Ningbo, PEOPLES R CHINA, 2014.
69. Rosell, J.; Sjöholm, J.; Richter, M.; Alden, M., Comparison of Three Schemes of Two-Photon Laser-Induced Fluorescence for CO Detection in Flames. *Applied Spectroscopy* **2013**, *67* (3), 314-320.
70. Loge, G. W.; Tiee, J. J.; Wampler, F. B., Multiphoton Induced Fluorescence and Ionization of Carbon Monoxide ($\text{B}^1\Sigma^+$). *Journal of Chemical Physics* **1983**, *79* (1), 196-202.
71. Krupenie, P. H.; Benesch, W., Electronic Transition Moment Integrals for First Ionization of CO and A-X Transition in CO^+ . Some Limitations on use of R-Centroid Approximation. *Journal of Research of the National Bureau of Standards Section a-Physics and Chemistry* **1968**, *A 72* (5), 495.

72. Moore, J. H.; Robinson, D. W., Study of Some Electronic Transition Probabilities in CO and CN. *Journal of Chemical Physics* **1968**, *48* (11), 4870.
73. Dietrich, P.; Strickland, D. T.; Laberge, M.; Corkum, P. B., Molecular Reorientation During Dissociative Multiphoton Ionization. *Physical Review A* **1993**, *47* (3), 2305-2311.